# Doctor Thesis

## Autonomous appearance of dynamic motility and cell-like structure: Physico-chemical modeling

## 生命体の動的運動挙動・細胞様構造の自発的創成：物理化学モデルによる研究

Hiroki Sakuta

作田　浩輝

Graduate School of Life and Medical Sciences,
Doshisha University

同志社大学大学院 生命医科学研究科

November, 2019

# Contents

# List of Figures

# Chapter 1

# General introduction

Living organisms maintain their lives under the highly crowding condition of biomolecules. Biomolecules including DNA, RNA and multifarious proteins compose the cellular cytoplasm and nucleus, and, the cells contain such molecules with the concentration of 30 to 40 wt/wt% [1, 2]. Most of biomolecules are sized number of nm to number of 100 nm, and they are exposed to the thermal fluctuation in cellular environment. In other words, each molecules show the behavior of random motion in cell. Under such environment, living organisms assemble bio-macromolecules like DNA, RNA and proteins, in addition, those molecules compose the cytoplasm, nucleus and the cells, which are the fundamental unit of life.

Living organisms synthesize the proteins which need for their life cycle by using genetic code polymers, DNA and RNA. That is, so called, "Central dogma" of basic concept for molecular biology [3, 4]. DNA having genetic information of the protein is replicated by itself and transferred the genetic information to the mRNA. The genetic information which mRNA have is translated to the proteins at ribosome. Generated proteins contribute to the life activity of cellular differentiation, cell division, morphogenesis and which is extended to the motile of cells and organs.

On the other hand, it is unfavorable to govern huge amounts of components in technology in industrial systems including mechanical and electrical which human being have. Living cells contain number of $10^7$ - $10^9$ various proteins [5, 6]. And, each of them plays a part of life cycle in living organisms. That is huge greater than that of human technology. In terms of eukaryotic multicellular organisms, the cells having huge number of biomolecules compose the organisms. That is, the mechanisms that

living system maintain their living cycle is completely different from the technology human being have.

Living organisms are able to arrange and utilize the suitable matters in the right places, which include the assemblies of bio-macromolecules such as nucleotides and proteins, and the composition of organelles in the cell. However, regarding not only the formation of the structure also the control of the function of living organisms, the important essences of mechanism on the self-organized manner are not clear. In the present study, it is aimed to unveil the essences of the mechanism in the formation of structure and the control of the function by using real-world experimental model. Here, it will be shown the simplified cellular model utilizing the biomolecules extracted from the living cell and the artificial model of motility of living organisms composed by the abiotic origin molecules.

## 1.1 Specific manner of macromolecules under the crowding condition

It have become clear the specific properties of macromolecules and their crowding environment [7–10]. It is known that DNA, RNA, protein and saccharides in living cell are also macromolecule. For example, proteins are composed by polymerizing the amino acids that exist 20 spices in the living organisms. When the one dimensional array of amino acids form the three dimensional structure, the proteins are indicating the certain activities. Here, there is a question, "How can living organisms produce the certain activities by folding the proteins?" This question is applied not only for the activities of proteins, but for the all of function of biomolecules. In this study, it will be discussed the general properties and functions of macromolecules apart from the micro and local properties of macromolecules.

### 1.1.1 Macromolecules in the solution

First, we will discuss the property of single molecular behavior in macromolecule. Here, the macromolecules are regarded their shape as the rope. It is defined the tangent vectors of the point $i$, $j$ on molecule are $\overrightarrow{u_i}$, $\overrightarrow{u_j}$. The average value of inner

product of two vectors become,

$$\langle \overrightarrow{u_i} \cdot \overrightarrow{u_j} \rangle = \exp\left(-\frac{s}{\lambda}\right) \tag{1.1}$$

Where the $s$ is the distance of two vectors, and $\lambda$ is persistent length of the chain of macromolecule.

It can be regarded ideal chain, when the chains have uniform elasticity and they don't have self-exclusion volume. The ideal chain is expressed as the connection of sticks whose length corresponds to the Kuhn length. Kuhn length is established by using the persistent length $\lambda$,

$$b = 2\lambda \tag{1.2}$$

The vector from the starting point to end point of macromolecule is defined as $\boldsymbol{R}$, it is shown as the connection of the number of $N$ vectors of length $b$,

$$\boldsymbol{R} = \sum_{i=1}^{N} b_i \tag{1.3}$$

Here, the statistical average of $\boldsymbol{R}$ become

$$\langle \boldsymbol{R}^2 \rangle = \langle \boldsymbol{R} \cdot \boldsymbol{R} \rangle = \sum_{i=1}^{N} \langle b_i^2 \rangle + 2 \sum_{i=1}^{N} \langle b_i \cdot b_j \rangle \tag{1.4}$$

The chain is the free jointed chain of sticks.

$$\langle \boldsymbol{R}^2 \rangle = Nb^2 \tag{1.5}$$

Thus, it become clear that the end-to-end distance of ideal chain is expressed by the random walk of each segments. The random walk follows the Gaussian distribution.

$$R \sim bN^{\frac{1}{2}} = 2\lambda N^{\frac{1}{2}} \tag{1.6}$$

And, the absolute value of $R$ is the distance of end-to-end distance of the chain, this value is in proportion to the inertial radius $R_g$ which indicates the expanse from the center of gravity.

When we describe about the real molecular chain, the segments with random walk never overlap each other, in other words, the points on the molecules never occupy the same point in the space. Considering this point, the scaling of the real chain is obtained as below by introducing the effect of self-exclusive volume.

$$R_r \sim \lambda N^{\frac{3}{5}} \tag{1.7}$$

The volume expansion of these chain can describe as the spherical expansion,

$$V_r \sim R_r^3 \sim \lambda^3 N^{\frac{9}{5}} \tag{1.8}$$

In this case, the number of segments in the molecular chain is $N$, the density of segments $\rho$ become as follows:

$$\rho \sim \frac{N}{V_r} \sim \frac{1}{N^{\frac{4}{5}}} \tag{1.9}$$

and the density and the number of segments make the closely inverse relationship. Thus, it is expected the real macromolecule have the property the density of segments decreases, and the volume expansion increase with increasing of segments. This means the occupied volume by macromolecules in the solution become larger with the increasing of the molecular weight. In the living organisms, nucleic acids, proteins and saccharides of biomacromolecules dissolve in water with same characteristics of macromolecules. In addition, in the limited fractionation like cell or organelles, the volume fraction of macromolecules will become higher and the effect for other molecules or their conformation should be significant.

### 1.1.2 Mixing entropy of macromolecules

Next, we will discuss the property of the polymer solution from the aspect of single molecule. Here, we will consider the system of dissolution of solute polymer to the solvent water [10, 11]. In general, when the several numbers of molecules are mixed, those molecules become homogeneously mixed spontaneously. In other words, the molecules diffuse to be uniform and disorder of whole system increase. It is the same tendency for the system of dissolution of solute to the solvent, in the solution, the molecules of solute and solvent become homogeneous after dissolution ignoring the specific interaction between molecules. The amount of disorder is characterized by the entropy $S$, and here we expressed the entropy of mixing as $S_{mix}$. The free energy of solution $F_{mix}$ related to the mixing entropy $S_{mix}$.

$$F_{mix} = E_{mix} - TS_{mix} \tag{1.10}$$

where $E_{mix}$ is the energy determined by the interaction between whole molecules (including attractive and repulsive force) and $T$ is temperature of the system.

As shown in Fig. 1.1(a), two types of molecules are in the containers separated by partition respectively. We consider this the reference condition. When the partition is removed, both types of molecules move to the opposite volume and whole system become homogeneous, spontaneously. The increase of disorder results in the increase of the mixing entropy $S_{mix}$.

The positions of each molecule can arrange by many ways. And, the mixing entropy $S_{mix}$ expressed by the configurational entropy which is determined by the number of possibility.

$$S_{mix} = S(N_0,\ N_1) - S(0,\ N_1) - S(N_0,\ 0) \tag{1.11}$$

The entropy of configuration is described using Boltzmann relation,

$$S(N_0,\ N_1) = k_B \ln W(N_0,\ N_1) \tag{1.12}$$

$\ln W(N_0,\ N_1)$ is the number of possibility. $S(0,\ N_1)$ and $S(N_0,\ 0)$ are the entropy before mixing, and S$(N_0,\ N_1)$ is one after mixing. The number of solvent molecules is $N_0$, and solute is $N_1$. Here, it is assumed the entropy of mixing of reference condition as $S\,(0,\ N_1) = 0$, $S\,(N_0,\ 0) = 0$, the mixing entropy become

$$S_{mix} = S(N_0,\ N_1) = -k_B\,(N_0 \ln \phi_0 + N_1 \ln \phi_1) \tag{1.13}$$

$\phi_0$ and $\phi_1$ are the volume fraction of solvent molecules and solute molecules. The volume fraction means the occupied volume of each molecules of whole volume.

As shown in Fig. 1.1(b), we consider the case monomer molecules are polymerized to polymer molecules. For example, it corresponds to the ethylene glycol molecules are polymerized to polyethylene glycol. As mentioned above, the mixing entropy is determined by the number of possibilities of configuration. We assume the polymer (high polymerization state) and monomer (low polymerization state) are mixed by same weight concentration. In the case of polymer, the number of molecules decrease in inverse the polymerization state. That is, a plural number of monomers make connection and translational motion as a group. Polymer solution have a smaller number of molecules than monomer solution under the same weight concentration. So, the mixing entropy of polymer become smaller than monomer. It is important point, as shown in Eq. (1.10), the energy determined by the interaction of molecules, $E_{mix}$, become remarkable because the entropy of mixing decrease in the case of polymer solution. From this point of view, the specific behavior, like phase segregation, can

be emerged in the polymer solution. In the living system, the biopolymer is highly concentrated, and it is expected each molecule have low mixing entropy. Living organisms can form the structure of their bodies and control the function utilizing the such properties of polymer solution. In this study, it is purpose to construct the experimental model of living system by using the polymer properties.

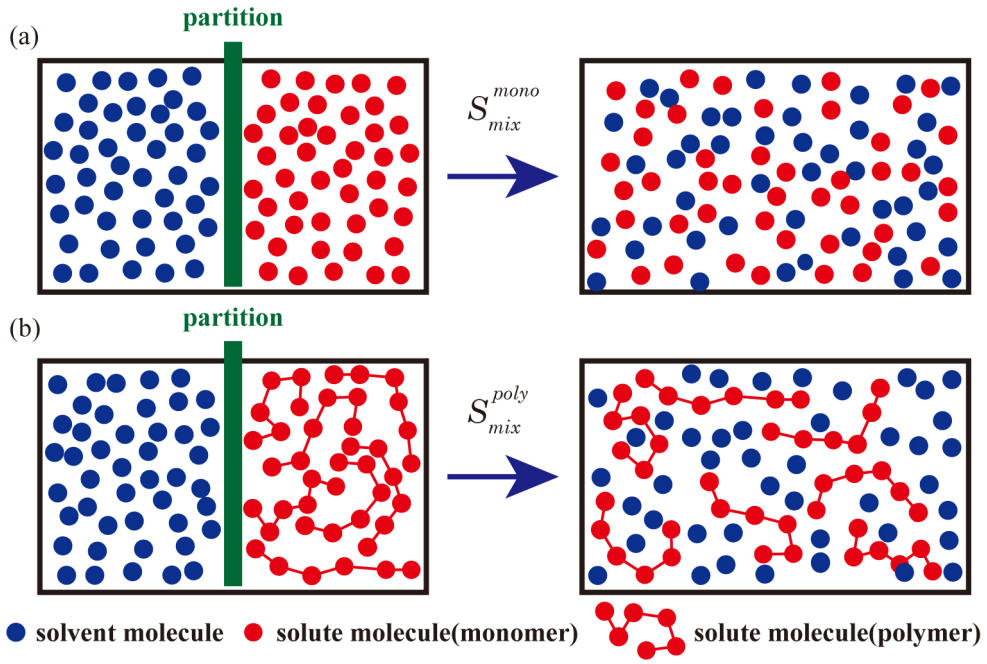


Figure 1.1 Schematic representation of mixing entropy comparing the reference condition and mixed condition (a) Mixing of monomer molecules and solvent molecules. (b) Mixing of polymer molecules and solvent molecules.

### 1.1.3 Aqueous two phase system

The technique utilizing the properties of polymer solution have been developed from 1960's. When the several number of polymer solutions are mixed, the phase segregation for each phase are emerged. Under the condition of phase segregation, the biopolymer, nucleic acids and proteins and so on, localized in the either phase. Aqueous two phase system have been developed as a technique separating nucleic acids, proteins, saccharides, cell [12].

Polyethylene glycol (PEG) and dextran (DEX) is one of the most famous system separating biopolymers in the field of biochemistry [12]. In this system, when the

solution including DNA, RNA or proteins are mixed to the PEG and DEX solution, PEG and DEX separated to each phase and biopolymers tend to localize in the DEX phase. In this study, we utilize these characteristic behaviors of the composing compartment and spontaneous localization to the compartment for model system.

## 1.2 Spontaneous emergence of motility under isothermal condition

In this study, we will focus on the essential function of living system, the emergence and control of motility of living organisms. In recent years, the motile of living organisms generated by the transduction of chemical to kinetic energy under isothermal, non-equilibrium and open system, using nm scale molecules [13].

It is suggested the mechanism of living system is entirely different from the heat engine following the second law of thermodynamics human beings use as the technology. In the case of heat engine, it is need to prepare the insulating container, burn the fuel in that and compose the gradient of temperature and pressure. From the gradient of pressure, it can extract the kinetic energy from chemical energy via heat. However, in living system nm scale molecule and $\mu$m scale organs are difficult to make thermal insulating condition compared with the m scale heat engine. When we consider the thermal diffusion, diffusion equation is as below and the time of thermal diffusion relates to the square power of distance.

$$\frac{\partial U}{\partial t} = D\frac{\partial^2 U}{\partial x^2} \tag{1.14}$$

$$\Delta t \sim \frac{\Delta x^2}{D} \tag{1.15}$$

Here, it is assumed that the thermal diffusion of cellular scale as 1 $\mu$m and the size of insulating container as 1 m. Considering a diffusion coefficient $D$ of 1 $\mathrm{m}^2/\mathrm{s}$, it takes 1 s to diffuse 1 m, and just $10^{-12}$ s to diffuse 1 $\mu$m. That is, molecules or cells is much smaller than the heat engine which human beings practically use. And, such micro system can't create thermal gradient. Therefore, living organisms adopt other mechanism to produce motility which is entirely different from heat engine [14].

In living organisms, the motor protein of actin-myosin, microtubule-kinesin or -dynein is reveled in recent years [4, 15–19]. The motor proteins of myosin and ki-

nesin/dynein are size of several ten nm and slide on the filamentous rail proteins of actin and microtubule which are size of several hundred nm to several $\mu$m. In the heat engine the macroscopic thermal gradient relates to the disproportion of microscopic molecular thermal fluctuation, and at the term of relaxation of disproportion it can extract the kinetic energy. Thus, it is need the process that the thermal fluctuation become disordered state. However, in the living system, nm sized molecules which are affected by the thermal fluctuation produce $\mu$m to m sized macroscopic motion by collecting the motion of each molecules. In other words, it is reverse cascade against the heat engine of classical mechanics.

As another point of view, there is a practical technology of producing kinetic energy from chemical energy under isothermal condition. That is the battery and electric motor. However, it seems also the different mechanism from living system. The living body is mostly composed of water, and it is difficult to extract certain electric current at right place and right function.

### 1.2.1 Self-propelled motion of droplets, particles

Recently, it is reported that the self-propelled motion of the objects in the solution or on the surface of solution including oil droplet, camphor boat, particle and so on [13, 20–29]. These systems show the similar behavior to the living system about the transduction of energy, they can generate the motion under isothermal condition. Thus, these systems are expected to real-world simplified model of living system motility. These self-propelled motion is generated by the instability of interfacial tension induced by the chemical, temperature, light and so on. When the surfactant expand on the interface inhomogeneously, the gradient of interfacial tension emerge and Marangoni flow induced by interfacial instability propel the objects. It is directly transducted from chemical energy to kinetic energy without going through heating. Moreover, it can artificially produce the partial gradient of interfacial tension around the objects or the objects continuously generate motion by producing the gradient of interfacial tension spontaneously. The nm scaled molecules which indicate the surface activity produce the mm to m scaled collective motion. It is expected these system contribute to clarify the essential mechanism, "how can nm scaled biomolecules produce the macroscopic ordered motion?" In this study, it is aimed to create self-

propelled system mimicking the intelligence of living system to unveil the mechanism of real living system.

# Part I

# Self-organized formation of cell-like structure under crowding condition

# Chapter 2

# Self-emergent protocell generated from aqueous solution with macromolecules and phospholipids

## 2.1 Introduction

All living organisms, of course cellular units themselves, have complicated intracellular structures possessing various specific functions. The sophisticated fabrications on living cells are important to maintain lives and it has been generally considered that such structures may be originated under control of dynamic expression of the gene set, but it is also true that another physicochemical mechanisms based on molecular nature that cannot be directly regulated by gene expression may be important to consider because the typical scale of living cells are too large compared to that of each gene product to explain generation of cellular structures simply through accumulation of the gene products.

Recently, for plausible mechanisms to generate microstructures of inside cells, liquid-liquid phase separation (LLPS) widely attract attentions of researchers in life sciences [30]. LLPS occurs via a multitude of nonspecific interactions and/or forces and does not require biochemical binding or attraction that seen between certain specific pairs of molecules [31–36]. The remarkable of LLPS includes the non-uniform localization and concentration of solutes, resulting in the ability to isolate certain chemical systems and so parallelize multiple chemical reactions within a space of the

same cell [37–39]. Naturally, not only providing the space for a certain reaction to take place selectively, LLPS would be also involved in the generation of intracellular structures that have different exchangeability of substances or different variability of morphology or size than organelles covered with lipid membranes [40, 41].

From the characteristic, stable compartments whose solute concentration is different from their surroundings are emerged in solution even without lipid membranes, thus LLPS has been considered to be a candidate of the origin for the membraneless organelles such as nucleoids, P-bodies and some stress granules [42]. For engineering, by utilizing LLPS, making the manipulation of localized or concentrated target substances possible or advanced layered chemical systems realize through parallelization of a plurality of chemical reaction pathways is expected.

Ideally, the phase separation generally occurs among mutually immiscible polymer solutions; e.g., aqueous two-phase systems (ATPSs) is well known as systems exhibiting microphase separation [12]. Popularly, it has been well known that solution consisting of polyethylene glycol (PEG) and dextran (DEX) causes LLPS [43, 44]. Here, we found that phospholipids added into such solution spontaneously assemble at the interface between two phases, PEG-rich (PEG phase) and DEX-rich phases (DEX phase), and demonstrated that lipid vesicles confining only one phase (DEX phase in this case) were formed.

Our previous study has revealed that when double-stranded DNA and cytoskeletal actin filament, the both are biological components essential for living cell, are added to LLPS caused in the two-component system of PEG and DEX, they are selectively accumulated in the DEX phase [45,46]. Under the conditions of microphase segregation, long DNA ($\geq$kbp) was entrapped within cell-sized droplets rich in DEX (as in Figure 2.1(a)). As shown in Fig. 2.1(b), F-actin, linearly polymerized actin, was entrapped specifically within microdroplets rich in DEX, whereas G-actin, a monomeric actin, was distributed evenly inside and outside these droplets. This study has been extended to a system with both F-actin and DNA, and it was found that DNA molecules were localized separately from aligned F-actin proteins to create microdomains inside microdroplets, reflecting the self-emergence of a cellular morphology similar to a stage of cell division (as in Fig. 2.1(c)).

Therefore, this finding will lead to a useful method for encapsulating the localized or concentrated target substances into membrane vesicles.

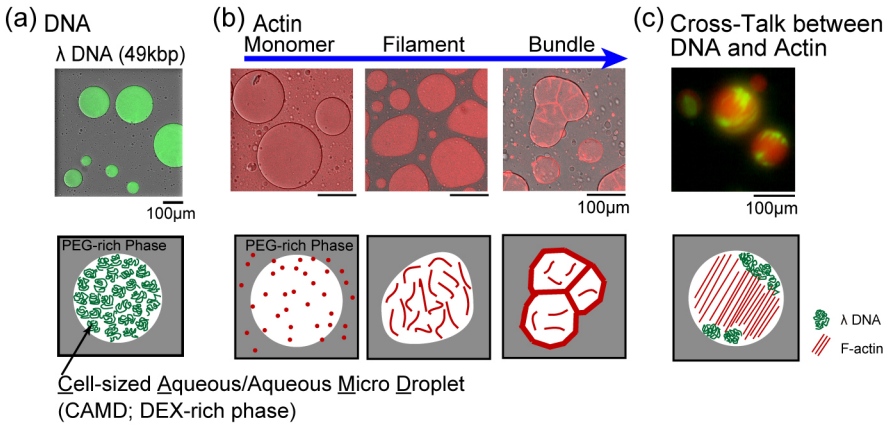


Figure 2.1 Specific localization of DNA and actin in the CAMDs. (a) Localization of DNA, λDNAs (49 kbp, 38.5 mm in nt units) were observed only for DEX-rich CAMDs, and were specifically localized inside the droplets. λDNA was labeled with Gel-Green. (b) Localization of actin, depending on the polymerization state. Monomeric actins, G-actins, were distributed homogeneously inside and outside of CAMDs. F-actins (dispersed F-actins and bundled F-actins) localized inside the droplets, and bundled F-actins were gathered to the interface of the droplets. (c) Cross-talk between F-actin and long DNA (λDNA). DNA molecules appeared to be segregated from the center, compressed by the aligned F-actin.

## 2.2 Materials and methods

The materials and methods of generating cell-sized micro droplet (CAMD) and introducing DNAs is referred from our previous study [45].

### 2.2.1 Materials for microdroplet

We used a polyethylene glycol (PEG)/dextran (DEX) aqueous two-phase system (ATPS). PEG 6,000 was purchased from Wako Pure Chemical Industries (Osaka, Japan), and its average molecular weight (MW) is 7,300 to 9,300 Da. DEX was also purchased from Wako Pure Chemical Industries, and its average MW is 180,000 to 210,000 Da. These two polymers were dissolved in nuclease-free water (Milli-Q, 18.2 MΩcm to prepare 20 wt% stock solutions. To observe the DEX-rich domain, fluorescein isothiocyanate – dextran (FITC-Dextran) was purchased from Sigma-Aldrich

Co. LLC (St. Louis, MO), average MW is 250,000 Da. And, the excitation(Ex) and emission(Em) wavelength are 490 mm and 520 mm.

### 2.2.2 Preparation of DNA

$\lambda$DNA with a MW of 31.5 MDa (48,502 bp) was purchased from Nippon Gene Co., Ltd. (Tokyo, Japan). It was dissolved at a concentration of 0.25 g/L (nucleotide concentration of 770 $\mu$ M). To label $\lambda$DNA, GelGreen as a fluorescent dye (Ex/Em of 500/530 nm) was purchased from Biotium Inc. (Fremont, CA). It was dissolved in nuclease-free water as a 0.5 mM stock solution. The antioxidant 2-mercaptoethanol (2ME) was purchased from Wako Pure Chemical Industries. The buffer solution tris(hydroxymethyl)aminomethane-HCl (1 M Tris-HCl, pH 7.5) was purchased from Nippon Gene, and diluted with nuclease-free water to obtain 200 mM stock solutions.

### 2.2.3 Preparation of phospholipids

In this study, two methodology to prepare the suspension of lipids were adopted. First, it has been already found that lipid vesicles are formed by simple hydration of lecithin powder [47]. As a convenient method for adding lipids to the LLPS system, the suspension portion rich in lipids of a solution in which lecithin powder has been hydrated was mixed into the PEG/DEX-binary solution. Second is the method used classically. The lipid molecules dissolved into the organic solvent and after the organic solvent was volatilized multilamellar lipid film was obtained. It is known as the gentle hydration method obtaining the giant unilamellar vesicles [48–50]. The hydrated suspension of multilamellar lipid film was mixed into the PEG/DEX-binary solution, same as simple hydration of lecithin powder.

### 2.2.4 Microscopy

Images were obtained with a fluorescent microscope. The microscope was a Axio Observer.A1 (Carl Zeiss, Germany) equipped with a 40x objective. And the images were obtained with a CCD digital camera (C11440, Hamamatsu Photonics). The obtained images were analyzed by using ImageJ software (Rasband, W.S., ImageJ, US National Institutes of Health, Bethesda, Maryland, USA, http://imagej.nih.gov/ij/,

1997 – 2019).

## 2.3 Results and discussions

### 2.3.1 Spontaneous formation of lipid-surrounded droplet

The suspension portion of solution where lecithin was hydrated contains numeral lipid vesicles and aggregates (Figure 2.2(a)). Their shape is mostly sphere and size is variety from sub-micrometer to tens of micrometer. Because the fluorescence intensity of those vesicles and aggregates that were stained with rhodamine B are not uniform, they are presumed to have various structures, including vesicles formed from several lipid bilayers, the onion-like that densely stacked many membranes, and droplet that does not have any layered structure.

After mixing of the suspension to the PEG/DEX-binary solution, the fluorescence signal showing the distribution of lipids is mainly observed between PEG and DEX phases (Figure 2.2(a)). Under the condition employed in this study, spherical DEX-rich regions (DEX phases) disperse among PEG phase in the solution that is causing LLPS (Figure 2.2(b-i)). Phospholipids are localized to trace the spherical surface of each DEX phase (Figure 2.2(b-ii)), indicating that the mixing of lipids does not affect the phase separation and the shape of each phase. The profile of the fluorescence intensity obtained from the cross-sectional image of a certain DEX phase shows that such phospholipids are concentrated in a very narrow place, just like the boundary between two phases (Figure 2.2(b-iii)). As a result of these, the micrometer-sized containers made of phospholipid in which a DEX phase is encapsulated are constructed. These are stable with compared to the DEX phases that are formed in LLPS in the usual, i.e. in the absence of lipid. When two DEX phases are contact, shortly fusion occurs to form a single spherical DEX phase with a larger diameter. However, in the case of lipid-surrounded DEX phases, they do not fuse easily and remains in contact for a long hour.

It is also observed that dot-like small clumps are scattered inner the lipid-surrounded DEX phases (Figures 2.2(b-ii)). Probably they are vesicles or aggregates made of lipids that have remained without accumulating at the boundary between two phases, in alternatively they are aggregations of hydrophobic mixtures contained

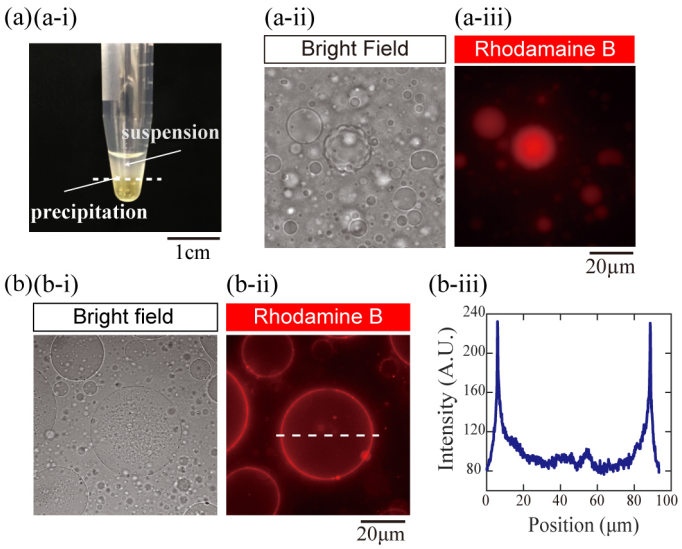


Figure 2.2 Accumulation of phospholipids to the interface of droplet. (a) Simple hydration method for preparing lipid vesicles. (a-i) is the Picture of hydrated solution. Powder lecithin form soy bean was immersed in the water. (a-i), (a-ii) Microscopic images of suspension portion rich in lipids of a solution. (b) Fluorescent microscopic image of mixing lipid suspension for PEG/DEX-binary solution. (b-i), (b-ii) Microscopic images. (b-iii) Spatial profile of the fluorescent intensity corresponds to the broken line.

in lecithin. On the other hand, almost no such fluorescent signal of phospholipids is observed in the PEG phase. This may be consistent with the observation that macromolecules or complexes with large molecular weight, such as long double-stranded DNA and polymerized actin filaments, are localized only in the DEX phase [45]. And, this is also observed with spontaneous localization of cells [51].

The encapsulation of DNAs lipid surrounded structure is observed. Our previous study has revealed that long double-stranded DNAs are accumulated to the DEX phase [45,46]. When λDNA of long DNA are mixed to the PEG/DEX-binary solution together with the lipid suspension, the droplets of DEX phase accumulated the λDNA inward and lipids to the interface of the droplets as shown on Figure 2.3. Here, we examined using the hydrated suspension of multilamellar lipid film was mixed into the PEG/DEX-binary solution. It is observed similar results by using both methods for preparing lipid suspension.

Lecithin obtained from nature contains many components derived mainly from bio-

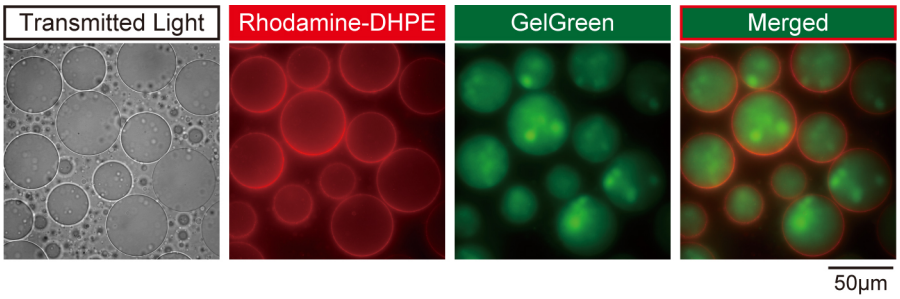


Figure 2.3 Spontaneous encapsulation of DNAs into micro compartment surrounded by phospholipid. The hydrated suspension of multilamellar lipid film was mixed, lipids are labeled with the fluorescent dye bound lipid (rhodamine-DHPE).

logical membranes in addition to phosphatidylcholine (PC). Therefore, in order to investigate the case of using purer synthetic PC or the case of using a phospholipid other than PC, the similar experiments were performed using dioleoyl-phosphatidylcholine (DOPC) or dioleoyl-phosphatidylethanolamine (DOPE) instead of lecithin (Figure 2.4).

Regarding the samples obtained by hydration of each phospholipid, lecithin and DOPC give almost similar results (Figure 2.4(a), top and middle panels). In the case of DOPE, larger aggregates are formed, and conversely, the number of vesicle formation is decreased than the cases of using lecithin and DOPC (Figure 2.4(a), bottom). These are consistent with the results that PE is hard to be hydrated and thus vesicles are not easily formed when PE alone is used, as reported from many previous studies on the preparation of lipid membrane vesicles.

After mixing of the suspension obtained by hydration of either DOPC or DOPE to the PEG/DEX-binary solution, the fluorescence signal showing the distribution of lipids is mainly observed between PEG and DEX phases, as well as the case of using lecithin (Figure 2.4(b), top). Particularly when DOPC is used, DEX phases can be more clearly enclosed with lipid (Figure 2.4(b), middle). The fluorescence indicating the distribution of lipids shows much higher intensity at the boundary of the two phases than the case of lecithin, indicating a larger amount accumulation of DOPC. Moreover, there is almost no dot-like aggregate as observed when lecithin is used. This may be due to that the samples made from DOPC contains much less contaminants compared to the case of lecithin, that is, more net amount of DOPC

is contained in the same amount of sample. Again here, even if two lipid-surrounded DEX phases meet, they do not fuse together easily and remain in contact.

When DOPE is used, the enclosing of the DEX phase with lipids can be viewed non-uniformly and poorly, and the dot-like aggregates are also observed (Figure 2.4(b), bottom). It is presumed that the difference in the preparation efficiency of membrane vesicles by hydration method between DOPE and other phospholipids described above is reflected. In the case of DOPE, lipid bilayer membranes are less likely to be prepared, and insoluble lipid aggregates rather than membrane vesicles are obtained. The former may cause the insufficient enclosing of DEX phases with lipid, and the latter may cause the appearance of dot-like aggregates inner the DEX phases.

It should be noted here that, the state of LLPS and the morphology of each phase, except for the fusion between the same phases, are not affected by the addition of phospholipid regardless of phospholipid used.

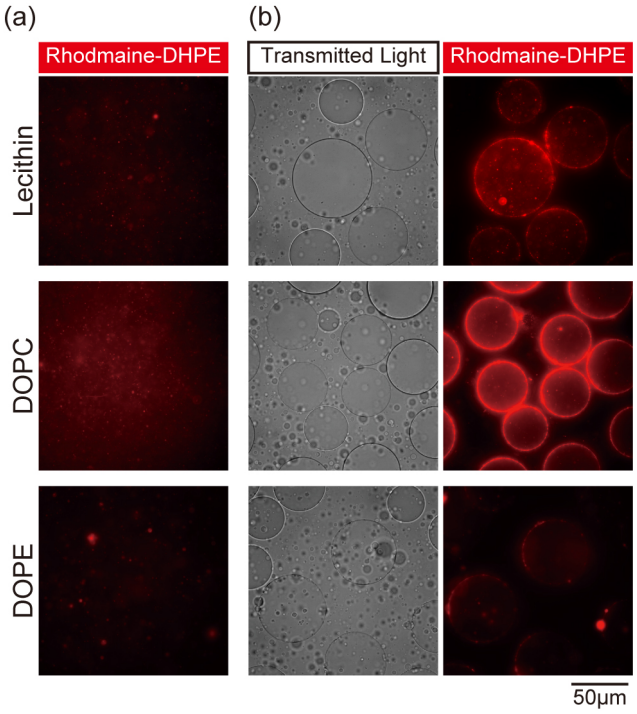


Figure 2.4 Spontaneous accumulation of mixing suspensions from variety of lipids. Lipid vesicles were obtained by the hydration of dry film. (a) Fluorescent microscopic images of lipid suspension. Top image: lecithin, middle: DOPC, bottom: DOPE. Each lipids labeled by the mixing of rhodamine-DHPE. (b) Fluorescent image of lipid suspensions mixed for the PEG/DEX-binary solution.

### 2.3.2 Stability of membranous structure

Next, we examined what structure the lipid surrounding the DEX phase formed, for example, lipid bilayer membrane or layered lipid accumulation. If the phospholipids surrounding the DEX phase form a bilayer membrane, it may be affected by the perfusion of aqueous solutions with different osmolality. So, in a chamber for microscopy, an LLPS solution in which lecithin was added to form a lipid-surrounded DEX phases was attached with an aqueous solution containing a high concentration of salt (5% NaCl), and was observed in real time (Figure 2.5). After the attaching between the two solutions, in the LLPS solution, by diffusion, the salt concentration should be increased and the polymers (in this case mainly PEG) should be diluted.

In the area proximal to the attaching point in the LLPS solution, lipids that had distributed throughout the boundary around a droplet, which is the DEX phase, gathered at one location as if it was shrinking, simultaneously the droplet itself disappeared. As a result, in depending on the degree of the lipid gathering, a lipid-surrounded DEX phase finally turned like a collapsed clump (Figure 2.5(b-i)), a remnant of ruptured vesicle (Figure 2.5(b-ii)), or a shrunken vesicle (Figure 2.5(b-iii)). In the area distal to the attaching point in the LLPS solution, the lipid-surrounded DEX phases tended to keep their spherical shapes (Figure 2.5(c)). The lipids surrounding them continued distribution throughout the boundary. However, the dot-like lipid clumps that were inside them came to the boundary resulting in that the appearance of their inside became clear (Figure 2.5(c-i)), or were moving by the convection generated (Figure 2.5(c-ii)).

Since the salt diffusion will cause a gradient of salt concentration in the LLPS solution, at the region nearer to where the salt solution applied, the changes in osmotic pressure will be rapid and the outside of the lipid-surrounded DEX phases will be more hypertonic. When the outside of a lipid membrane vesicle becomes very hypertonic quickly, probably because a large amount of water molecules move out of the vesicle, the membrane rupture or open a large hole resulting in the leakage of the contents, rather than simply shrinking the lipid membrane vesicle [52]. Therefore, the change to collapsed clump of lipids or remnant of ruptured vesicle may be due to a breakage of the membrane caused by the large difference in osmotic pressure (Figures 2.5(b)).

At the more distant region of the LLPS solution from where the salt solution applied, the changes in osmotic pressure will be slow and the effect will be smaller. The lipid-surrounded DEX phases that could maintain spherical shape would have been able to maintain the integrity and morphology of the membrane due to the slow outflow of water molecules (Figures 2.5(c)). The redistribution from the inside to the surface (Figure 2.5(c-i)) or the flowing movement of the dot-like lipid clumps (Figure 2.5(c-ii)) may be due to the flow generated with the slow outflow of water.

### 2.3.3 Direct observation of formation of membranous structure

In the above, by using the attaching of the two solutions and the diffusion of the solute, the responses of the lipid-surrounded DEX phases during when the osmotic pressure was changed were observed. Here, the same method was used to observe the process of lipid perfusion into the LLPS solution.

When lecithin was hydrated to a 5% PEG solution and then applied to a LLPS consisting of PEG/DEX solution, in the area where the solute appeared to be mixed, membranous structures were seen at the boundary around the DEX droplets (Figure 2.6(a)). In addition, around and inside such droplets, also small lipid vesicles or clumps were floating. When adding a solution that hydrated lipid to 5% PEG, the phase separation will be maintained due to PEG will not be diluted, so lipid-surrounded DEX droplets could be formed. On the other hand, in the region far from the attaching site, neither such membranous structures nor vesicles or clumps were found (Figure 2.6(b)), thus it seems that lipid has not yet reached. Results observed are consistent if lipids are supplied by the diffusion of these lipid vesicles or clumps.

## 2.4 Conclusion

As clearly demonstrated here, aqueous/aqueous microdroplets occurring through microphase separation can have plausible potential to work as a template to confirm the surface for membrane formation in real cells. Importantly, it is still a problem how membranes and/or lipid molecules could find their own destination during formation and disappearance of the membranes (envelopes) of intracellular microcompartments, such as nucleoids, some enveloped virions, etc. as describe below. Membraneless

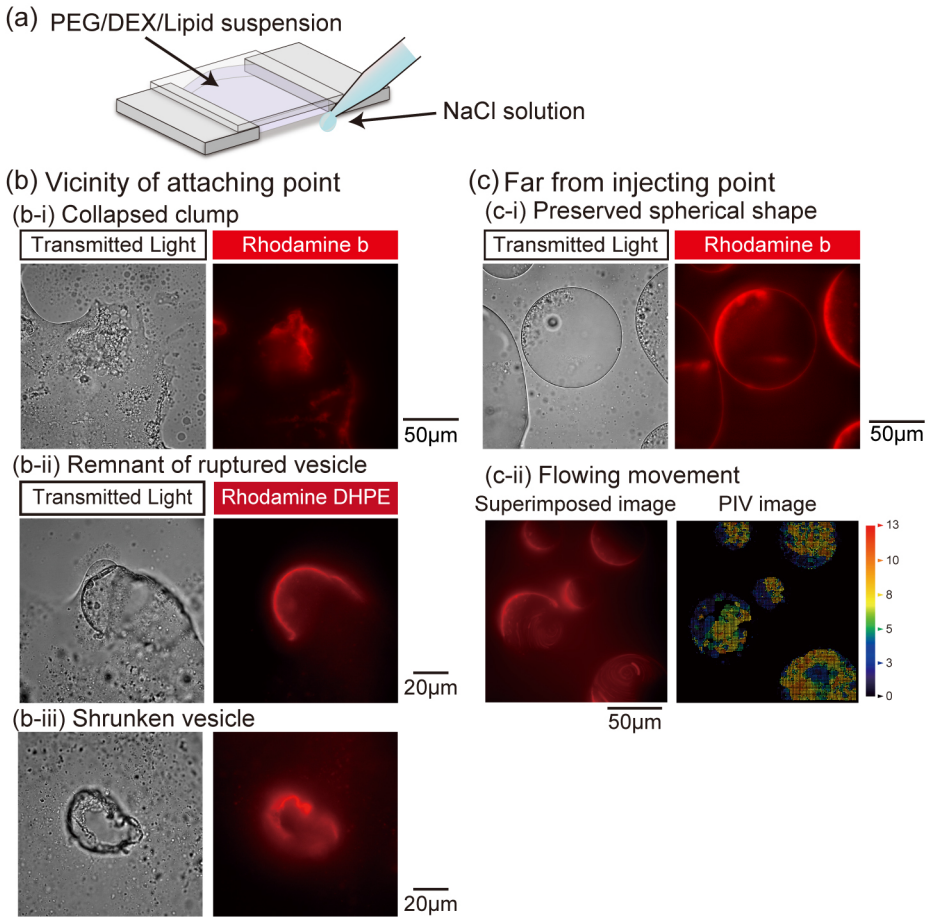


Figure 2.5 Morphological changes of lipid membranous structure by injecting of NaCl solution. (a) Schematic representation of the injecting procedure. Caused by the capillary force, NaCl solution penetrated the PEG/DEX/Lipid suspension. (b) The various morphological changes depending on the degree of the lipid gathering vicinity of attaching point. DEX-rich droplets tend to disappear and become homogeneous with PEG-rich outer solution by mixing NaCl solution, (b-i) collapsed clump, (b-ii) remnant of ruptured vesicle, or (b-iii) shrunken vesicle. (c) Far from attaching point. (c-i) By the effect of NaCl, inside the droplet became clear. (c-ii) The convection in the droplet emerged. Left: superimposed image of convection (duration: 8 s). Right: PIV image of the convection.

compartments generated by microphase separation could affect dynamics of these intracellular structures. Nuclear envelope has to repeat disassemble and reassemble for division of eukaryotic cells. At the end of mitosis, as like wrapping up the chromosomes after separation and other nucleic components, fusion of vesicles derived from

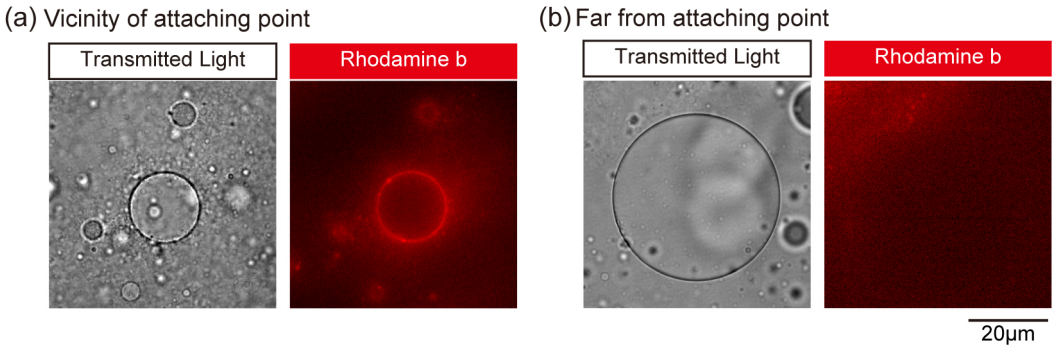


Figure 2.6 Accumulation of lipid vesicles on the interface of DEX-rich droplet by mixing lipid suspension after DEX-rich formation in PEG/DEX-binary solution. (a) Fluorescent image of the vicinity of injecting point. (b) Fluorescent image of the far from injecting point. Lipid membranous structure was hard to form.

the endoplasmic reticulum (ER) or reshaping of ER membrane takes place, resulting in the regeneration of nuclear envelope, i.e., the formation of the daughter cell's nuclear [53]. Autophagy, also it is essential for eukaryotic cells, includes the process in which the cytoplasmic compartment that appears to be generated by phase separation is covered and isolated by lipid membrane [54]. The origin of its lipid membrane is thought to be isolation membranes derived from ER [55]. In any case, the knowledge obtained in this study will be important because it reveals a relationship between the region condensing materials in a solution, such as a droplet composed of biological factors, and lipids.

-

# Chapter 3

# Aqueous/aqueous micro phase separation: Construction of an artificial model of cellular assembly [vi]

## 3.1 Introduction

Living organisms exhibit the self-organization of cells and intracellular organelles in a self-consistent manner. For decades, biochemical studies have unveiled the mechanisms that underlie such regulatory systems at the molecular level. Many macromolecules including nucleic acids and proteins are considered to act in a well-orchestrated manner to express biological functions, by building sophisticated structures under the specific interaction of gene products. On the other hand, it is also considered that even a single-cell system cannot be completely controlled through specific key-lock interactions. In these situations, the self-organization, or self-assembly, of biomolecules is indispensable for the development of various ordered structures, like phospholipid bilayers for cell membranes. Recently, it has been reported that membraneless organelles may arise from the micro phase separation of cytosols, which generates submicron-scale liquid droplets containing proteins and RNAs [30,37]. Since intracellular environments are highly crowded by such macromolecules, the emergence of liquid/liquid phase separation (LLPS) on a microscopic scale is a ubiquitous phe-

nomenon inside living cells [34, 35, 38, 39, 56].

Along these lines, many pioneering researchers have tried to model cellular and intracellular microcompartments by simply using an aqueous two-phase system (ATPS) consisting of solutions with hydrophilic polymers that exhibit LLPS on a microscale [56]. There are both some similarities and differences in the properties of micro phase separation between in vitro ATPS droplets and actual protein/nucleic acid-based droplets [36]. Polyethylene glycol (PEG), a flexible polymer, and dextran (DEX), a semi-flexible polymer, are popularly selected for the preparation of a typical ATPS [43]. Upon the vigorous mixing of a PEG/DEX solution, aqueous/aqueous (water-in-water) microdroplets are transiently formed, and various biomolecules and even inorganic materials can be partitioned into, or excluded from, these droplets, due to the chemical and morphological characteristics of the substances partitioned [31, 57–59]. Generally, this behavior of LLPS droplets is sharp [60], and could be associated with the origin of life and prebiotic functions [61]. Originally, ATPSs with various hydrophilic polymers, in addition to the above PEG/DEX, have been developed to extract molecules and supramolecules from biological materials [31]. Their simplicity makes them suitable for harboring functional proteins and living cells. For example, these microdroplets have been used to promote interaction between entrapped proteins to achieve their alignment [41, 62]. Previously, we have reported DNA entrapment [46], the formation of microparticles by crosslinking proteins [63], and the selective entrapment of filamentous actin (F-actin) and subdomain formation with dsDNAs and F-actin proteins, inside PEG/DEX microdroplets [45].

ATPS is known as a useful system to get selective partition on various biomacromolecules, DNAs, proteins, etc., under certain compositions of polymers. As has been indicated by Albertsson (1971) [12], previous literatures reveal a large number of phase diagrams for the phase separation of binary or more-component polymer solutions. The ATPS with PEG/DEX is popular in biochemical and biophysical research, and we previously used this system to investigate the dynamics (timecourse development) of phase segregation of micro-scale regions [64], as well as the specific localization of DNAs and proteins, such as the cytoskeletal protein actin [45, 46]. In these studies, we observed aqueous/aqueous (water-in-water) microdroplets with an average diameter of $\leq$ 10 - 100 $\mu$m. Importantly, the droplets are stably generated and remain after vigorous mixing using a vortex mixer, etc., near the critical point in

a phase diagram, because there is only a very small difference in density between the phases containing the two polymers in addition to the weak surface tension, which are unique characteristics of a polymer solution.

Compared to bulk ATPS, the above mentioned aqueous/aqueous microdroplet is suitable for microscopic observation; therefore, we can frequently observe intriguing phenomena with biological macromolecules only when these molecules are encapsulated within such microcompartments. For example, interestingly, actin proteins apparently change their preferred location (distributed evenly, encapsulated within the interior, and adhered to the inner surface) in droplets in PEG/DEX ATPS as their higher-ordered structure changes from monomeric (G-actin) through polymeric (F-actin) to bundled actin [45]. DNAs and F-actin entrapped simultaneously exclude each other to form subdomains inside the droplets. Thus, generally, biopolymers with semi-flexible and rigid chains are usually excluded from the PEG-rich exterior environment to the interior of DEX-rich microdroplets. In addition, further transformation of their structures as well as coexistence with other polymers possessing different properties could cause a change in their own positions.

Considering the unique characteristics to entrap certain biomolecules, it would also be expected that in even simple systems, living cells can find preferred locations in microdroplets and their localization can change with a change in the composition of the ATPS. Cells are much larger than the biomacromolecules, and cellular systems are more complicated. However, even though the model artificial system is quite simple, we would expect it to mimic the migration and arrangement of cells in an aqueous environment inside living bodies in a most basic manner, i.e., without any specific molecular interactions among genetic products.

Recently, Han et al. reported the formation and manipulation of cell spheroids [65], clearly indicating that ATPS could be a powerful tool for controlling cell position without causing important damage. In the present study, we used two different kinds of cells, erythrocytes (horse red blood cells; RBCs) and NAMRU mouse mammary gland epithelial cells (NMuMG cells) as models, and investigated how these cells are localized when entrapped inside ATPS microdroplets. Interestingly, we found that RBCs and NMuMG cells alternatively preferred to localize either in the interior or at the periphery of microdroplets, and this preference could be switched by changing the PEG/DEX ratio. We considered that the PEG/DEX interface property could change

with a change in the interface composition, and this could affect how the interface interacts with different types of cells to cause this switching.

## 3.2 Matrials and methods

### 3.2.1 Regents

We used polyethylene glycol (PEG) and dextran (DEX) to form an aqueous/aqueous two-phase system (ATPS): PEG 6,000 (molecular weight (Mw) 7,300 – 9,300 Da) and DEX 200,000 (Mw 180,000 – 210,000 Da) were purchased from FUJIFILM Wako Pure Chemical Industries (Osaka, Japan). PEG and DEX were stocked as solutions of 20 wt% dissolved in isotonic sodium chloride solution (0.9 wt% solution of NaCl) to regulate the osmotic pressure similar to that of cell membranes. The isotonic sodium chloride solution was prepared with nuclease-free water (Milli-Q, 18.2 $M\Omega \cdot cm$). Other reagents used were of analytical grade.

### 3.2.2 Cells

For observations of red blood cells (RBCs), we used the preserved blood of horse purchased from Nippon Bio-test Laboratories,Inc. (Saitama, Japan) and gently added a small aliquot of the blood to the PEG/DEX system without any washing. As model epithelial cells, we used NAMRU mouse mammary gland epithelial cells (NMuMG cells), which were cultivated from cultured cells at regular intervals as previously reported [66]. For mixing in the PEG/DEX system, the epithelial cells were separated in advance from the culture medium by centrifuge.

### 3.2.3 Microscopy

We observed ATPS microdroplets using bright field microscopy or confocal laser scanning microscopy (CLSM). Bright field microscopy images were obtained with an Axio Observer.A1 (Carl Zeiss, Germany) equipped with a 40x objective and a CCD digital camera (C11440, Hamamatsu Photonics). CLSM images were acquired with an FV-1000 laser scanning microscope (Olympus, Japan) and the images were analysed using FV10- ASW software (Olympus). The images acquired with the bright

field microscope were analysed using ImageJ software (Rasband, W.S., ImageJ, US National Institutes of Health, Bethesda, Maryland, USA, http://imagej.nih.gov/ij/, 1997 – 2019). In the CLSM observation, we used fluorescein isothiocyanate (FITC)-dextran (average Mw 250,000, Sigma-Aldrich; Ex. 488 nm) and the lipophilic dye Nile red (Thermo Fisher Scientific; Ex. 543 nm) to fluorescently visualize DEX-rich domains and RBCs, respectively.

## 3.3 Results and discussions

In the present study, we used two kinds of mammal cells: red blood cells (RBCs) and NMuMG cells, which are a type of epithelial cell. As shown in typical microscopic images in Figure 3.1, both RBCs and NMuMG cells were entrapped inside DEX-rich microdroplets when they were mixed in the ATPS with PEG:DEX = 10%:5% and 5%:5%. However, a close look at their distribution revealed that their location switched between the center and the periphery of the droplet with a change in the PEG/DEX ratio. n both cases, DEX-rich microdroplets were located on the bottom of the chamber due to their a little bit larger density as observed in the bulk experiment. Interestingly, these cells showed an opposite preferred distribution inside the droplets (Figure 3.1); at PEG:DEX 10%:5%, RBCs gathered near the interface, while NMuMG cells gathered inside the droplets rather than the interface. In contrast, at PEG:DEX 5%:5%, these preferences were reversed; i.e., RBCs were situated inner part of the droplets, and NMuMG cells were localized at their periphery. RBCs tended not to contact each other when they were trapped inside the droplets at either concentration of the coexisting polymers, whereas NMuMG cells positioned inside the droplets adhered more strongly to each other. Since NMuMG cells are adherent in their intrinsic property, encapsulation within DEX-rich droplets could enhance their attachment propensities [66].

Figure 3.2 shows histograms of the cell population vs. the position of microdroplets. Along the radial distance ($r/L$) normalized to unity by the average radius L of each droplet, entrapped cells were counted and the numbers were converted into a cell frequency. In both types of cells, the median location, which is indicated by arrow, of entrapped cells shifted from around the center (relative radial distance $r/L \sim 0.5$) to the periphery (relative radial distance $r/L = 1.0$). But the preference is opposite; i.e.,

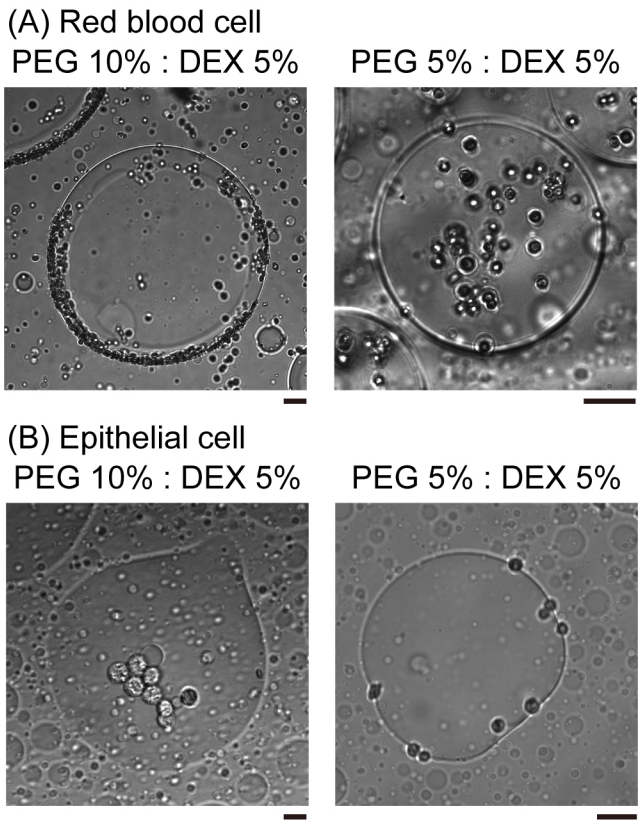


Figure 3.1 Specific distribution depending on the cell type and the concentration of PEG/DEX. (A) Microscopic images of red blood cells (RBCs) in microdroplets for each concentration of PEG:DEX (10%:5%, 5%:5%). The scale bar corresponds to 50$\mu$m. (B) Microscopic images of mouse mammary gland epithelial cells (NMuMG cells) in microdroplets for each concentration of PEG:DEX (10%:5%, 5%:5%). Note that the difference in color of cells could be due to a little variation in distance from the focus. Bar: 20$\mu$m.

RBCs and NMuMG cells (epithelial cells) were observed adsorbed to the interfaces at PEG:DEX = 10%:5% and 5%:5%, respectively. It should be noted that if cells were included inside a droplet without any attraction but with some repulsion to the interface, a peak of the population may appear around $r/L \sim 0.5$ because of the larger area compared to the region near the center.

To further examine how cells switched their distribution inside the droplets, we conducted CLSM observation of the PEG/DEX ATPS containing RBCs labeled fluorescently by Nile red (Figure 3.3). FITC-DEX illuminated the microdroplets and RBCs emitting red fluorescence were fully entrapped, but their distribution was apparently

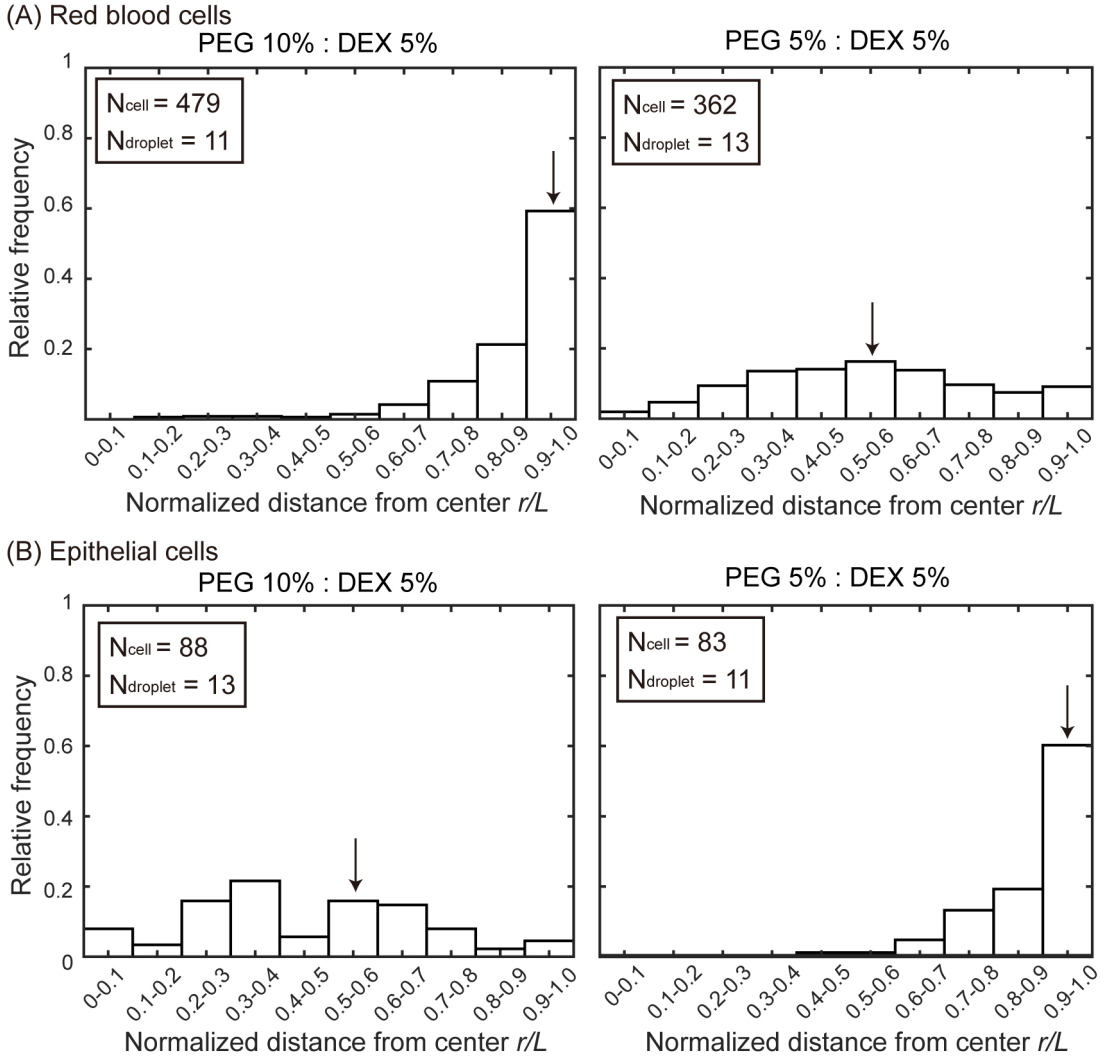


Figure 3.2 Histograms of positions where (A) RBCs and (B) NMuMG cells were distributed inside microdroplets with PEG:DEX = 10%:5% and 5%:5%. Horizontal axes indicate normalized distances ($r/L$) from the center of the droplets to the positions of the entrapped cells. The relative radial distance normalized to unity by the average radius $L$ of each droplet is 0 at the center and 1.0 at the periphery. The average radius is calculated from the area section of each microdroplet observed by microscopy, the distance r at which a cell was observed is divided by $L$ of the droplet entrapping the cell to give the normalized radial distance. Some cells were observed at normalized distances greater than unity because some droplets assumed a somewhat aspherical shape, and then the number of these cells are included in the number at $r/L$ of 0.9 – 1.0. Arrows indicate the medians to express the trends in cell localizations. The total numbers of counted cells ($N_{cell}$) and droplets ($N_{droplet}$) are indicated.

different at PEG:DEX = 10%:5% and 5%:5%, as in Figure 3.1. Under the former condition, RBCs were visualized on the inner interface of the DEX-rich droplet emitting green fluorescence, and in the latter, RBCs were relatively dispersed into the DEX-rich droplets. Fewer cells were observed at the top than the middle of the droplet, indicating that entrapped cells could fall under the present conditions. A number of RBCs were here also found at the interface of the microdroplet at PEG:DEX = 5%:5% (Figure 3.3 (B)), and this trend is consistent with the localization shown in Figure 3.2(A).

We here observed the simple switching of cell localization inside DEX-rich droplets. Both cell types, RBCs and NMuMG cells, preferred the interior, but they exhibited opposite trends when settling in different compartments. The preference in cell localization may be caused by various factors related to difference in cell properties, including their sizes, morphologies, surface structures, adhesive (non-adhesive) behaviors, number density, etc., so it is too complicated to permit us to give a detailed precise explanation for the mechanism. Therefore, the present condition we investigated is considered to be moderately suitable for simple demonstration of switchable behavior of cell localization inside ATPS droplets. For speculation, instead, we try to simply discuss this different preference by imagining cells with different dimensions under a crowded environment with PEG/DEX schematically illustrated in Figure 3.4 as follows.

Generally, DEX molecules have branched structures with some room for harboring other biomacromolecules, and PEG molecules have linear flexible structures with a high excluded volume under concentrated conditions. Since these polymers provide different aqueous environments, not only large biomolecules but also cells prefer the DEX-rich phase, which is less crowded than the PEG-rich phase. In the present study, we used two PEG/DEX ATPSs with different conditions; one is near the critical point in the phase diagram (5%:5%); the other is somewhat far from that point, and accordingly, the binodal line (10%:5%).

The surface tension with such aqueous/aqueous interfaces is not so strong compared to oil/water interfaces [67]. Therefore, it can be finely modulated by changing the PEG/DEX ratio. In the present case, at PEG:DEX = 10%:5%, the interface has a higher tension (surface energy) with a steeper gradient of polymer concentrations, and thus RBCs, which are relatively smaller than NMuMG cells, could keep located on

the surface, leading to reduction of the surface energy (Figure 3.4(A)). On the other hand, at PEG:DEX = 5%:5%, the surface free energy, or surface tension, is so low due to a small gradient of polymer concentrations that small RBCs with weaker effects on stabilization of the interface alternatively tend to leave and enter the interior of DEX-rich droplets, which can accommodate these cells (Figure 3.4(B)).

To interpret the opposite preference of NMuMG cells along the same scenario as the case of RBCs, their larger size can be taken into account in relation to depletion effects by PEG. NMuMG cells appear to move to the interior of DEX-rich droplets, avoiding the interface where PEG exists more densely at PEG:DEX = 10%:5%. In other words, PEG could effectively induce depletion effect on NMuMG cells due to their larger sizes (surface areas), so these cells can be located not near a PEG-rich surrounding but in a DEX-rich inner space, where they might be associated with each other by moderate depletion force with DEX polymers [67]. At PEG:DEX = 5%:5%, where most RBCs are located inside the droplets, NMuMG cells can stand adhering to the interface, leading to the efficient stabilization due to their greater dimension. Note that the surface free energy of the interface through the phase segregation of polymer solutions is generally much smaller than those for interfaces with small molecules, because of the small contribution of the mixing entropy for polymer systems [45].

It has been shown that interface properties are in general strongly correlated to the positioning and qualities of cells with various origins [65, 67] with some changes in genetic activities [68]. To achieve assembly of highly organized compartments including cells in microfluidics, interfacial environments where cells and biopolymers are accumulated should be well-regulated [69]. We here simply chose physiological saline for suspending cells, but it is not suitable for cell proliferation, but, along this line, when some conditions that facilitate micro phase separation and cell growth are available, our results would be expected to aid development of such techniques for constituting assembled cell systems.

## 3.4 Conclusion

In conclusion, it was found that living cells exhibit specific localization in an aqueous solution with water/water microdroplets generated through phase separation in the presence of hydrophilic binary polymers. It was revealed that two type of cells are

situated either in the interior or at the periphery of the droplets. By changing the relative ratio of the polymer content, switching of the cell localization was observed. The mechanism of such observations was interpreted in terms of polymer depletion effect on the micro phase separation. It is highly expected that the simple mixing procedure with micro water/water droplets provides novel methodology to construct 3D cellular assembly composed with difference cell species.

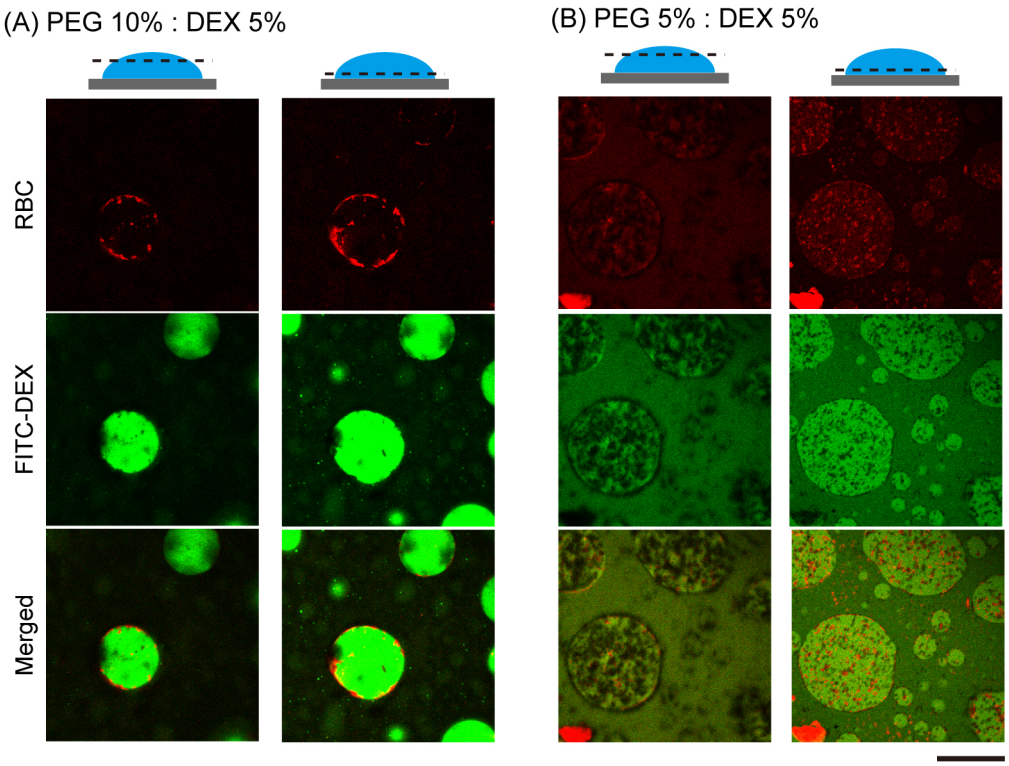


Figure 3.3 Confocal laser scanning microscopy (CLSM) images of RBCs in microdroplets. Top: RBCs labeled with Nile red. Middle: FITC-DEX. Bottom: Merged. The focal planes of the left and right columns for each condition are around the top and below the middle, respectively, as schematically illustrated for PEG:DEX = (A) 10%: 5% and (B) 5%: 5%. Bar: 100 $\mu$m.

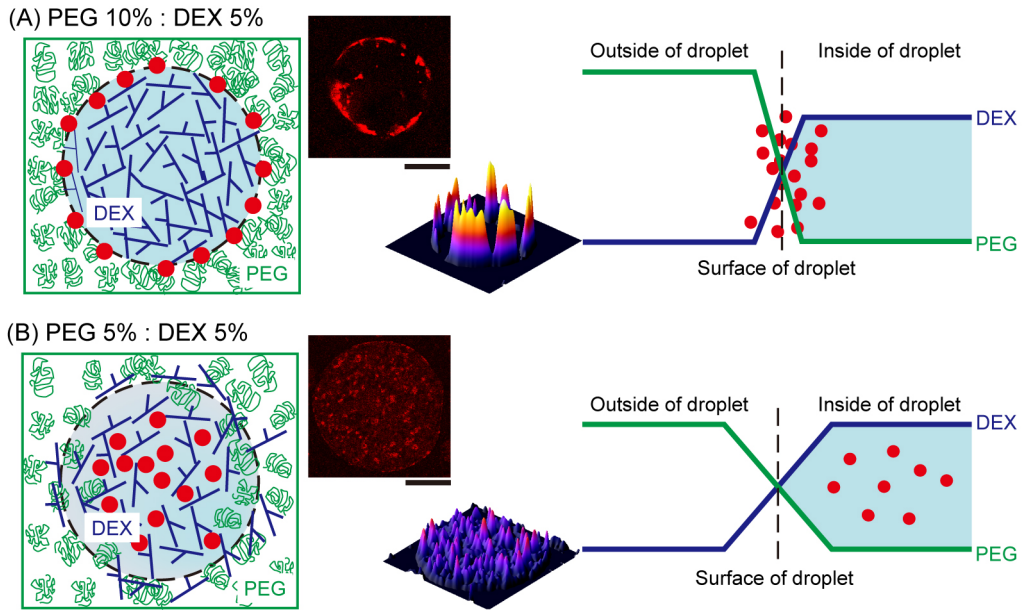


Figure 3.4 Schematic representation of the proposed mechanism of RBC distribution inside microdroplets generated by PEG and DEX. The leftmost illustrations show localization of RBCs (red closed circles) in droplets of DEX (blue branching line) surrounded with PEG (green random coil). The rightmost graphs depict the profiles of concentrations of DEX and PEG at the interfaces of droplets. (A) At PEG:DEX = 10%:5%, the high surface energy due to the steep gradient of polymer concentrations may cause the accumulation of RBCs at the interface to lower the tension. (B) In contrast, at PEG:DEX = 5%:5%, the surface tension can be moderately reduced to permit mutual invasion to some extent, and thus RBCs cannot be pushed to the interface so strongly. The pseudo three-dimensional images in the middle show the fluorescence intensities of Nile red from RBCs entrapped inside the DEX-rich microdroplets shown in the upper-left side, also in each upper-right panel of Figure 3.3. Bar: 100$\mu$m

# Part II

# Spontaneous emergence of dynamic motility under isothermal non-equilibrium condition

# Chapter 4

# Self-emerging collective motion of microtubules and kinesins in the cell-sized droplet

## 4.1 Introduction

Living organisms maintain their lives through adapting the external and internal change of environment. The dynamic behavior including transformation of the body, transportation of the certain materials, etc. is essential for the living cycle [4]. Biomolecular assemblies are dynamically arranged in a self-organized manner during the cell life cycle to contribute to various biological functions, including cell motility, morphogenesis, and division [70, 71]. The filamentous biomacromolecules including microtubules, actin and so on play significant rolls in the cell, the cytoskeleton, the rail of motor protein, etc. [72, 73]. Recently, to reveal the dynamic function of motor protein and rail filamentous protein, motility assays which protein filaments are driven by molecular motors bound to a substrate in the presence of ATP have been developed [19, 74, 75]. In addition, the dynamic behaviors of filamentous proteins including shrinkage or nematic order are focused from the experimental and theoretical aspect [19, 76–78].

On the other hand, living cell keep a highly crowded cellular cytoplasm with 30 – 40 wt/wt% of cellular materials, such as, nucleic acids and a rich variety of proteins [1, 2]. Under highly concentrated condition, living system can maintain the

dynamic behavior including cell motility, morphogenesis, and division, as well as the spatial arrangement and migration of organelles. And, it is becoming clear that these systems lack specific regulatory factors, which suggests that subcellular structures are generated in a self-organized manner under the crowded conditions of the cytoplasm.

In the present study, we focused on the specific dynamic manner of microtubule and kinesin in the living cell, that is, under the highly concentrated and micro sized partitioned environment. In our previous study, it was revealed the characteristic behavior of DNA and actin in a binary hydrophilic polymer system, polyethylene glycol (PEG) and dextran (DEX). When the solutions of two polymers are mixed at the composition of near the critical point of phase diagram, 10 – 100 $\mu$m cell-sized water/water microdroplets emerged. And, long DNA and filamentous actin tend to localize inside these droplets composed with DEX-rich phase [45, 46]. Whereas the behavior of microtubules and kinesin within the micro confinement have been reported, they are mostly water in oil droplet or liposome of phospholipids [79–81]. Herein, we will report the characteristic behavior of microtubule and kinesin in the cell-sized water/water microdroplet generated through the macromolecular crowding effect.

## 4.2 Materials and methods

### 4.2.1 Preparation for microdroplet

To generate water/water micro droplet, polyethylene glycol (PEG)/dextran (DEX) aqueous two-phase system (ATPS) was used. PEG 6,000 was purchased from Wako Pure Chemical Industries (Osaka, Japan), and its average molecular weight (MW) is 7,300 to 9,300 Da. DEX was also purchased from Wako Pure Chemical Industries, and its average MW is 180,000 to 210,000 Da. These two polymers were dissolved in nuclease-free water (Milli-Q, 18.2 M$\Omega \cdot$ cm) to prepare 20 wt% stock solutions. When the composition of PEG and DEX is 5% and 5%, the droplet of DEX-rich phase surrounded by PEG-rich phase are sized of 10 to 100 $\mu$m.

### 4.2.2 Microtubules and kinesin

Microtubules were polymerized from tubulin. Tubulin was purified from porcine brain tissue. Here, guanosine-50-[(a,b)-methyleno]triphosphate (GMPCPP) was used to polymerize the tubulin for microtubules. For observation of fluorescent microscope including confocal laser scan microscopy, tubulin labeled with ATTO647N (ATTO-TEC) was used at label ratio of 6In this study, it was used the tetramer kinesin of the human Eg5 was used. And, to observe more active motile of microtubules, chimeric $KIF5B_{head}$-$EG5_{tail}$ was used. By replacing the motor head of Eg5 for KIF5B, it indicates the 10-fold higher velocity of microtubules than the wild type Eg5 with less affinity [78]. To observe the kinesin by fluorescent microscopy, GFP-fused kinesin was used.

### 4.2.3 Microscopy

We obtained images with confocal laser scan microscope (CLSM), Nikon A1 microscope system through the 40x objective lens. The acquired images were analyzed by using a NIS Elements Viewer (Nikon), ImageJ (Rasband, W.S., ImageJ, US National Institutes of Health, http://imagej.nih.gov/ij/, 1997 – 2019) and MATLAB (MathWorks).

## 4.3 Results and discussions

### 4.3.1 Spontaneous localization of microtubules inside microdroplet

Figure 4.1 shows the confocal laser scanning microscopic images of microtubule. By polymerized tubulins with guanosine-50-[(a,b)-methyleno]triphosphate (GMPCPP), the microtubules in the bulk solution is as Fig. 4.1(a). When the microtubules mixed for the PEG/DEX binary solution, 10 to 100 $\mu$m sized microdroplets are emerged (Fig. 4.1(b-i)) and it is found the spontaneous localization of microtubules inside the droplet was occurred (Fig. 4.1(b-ii)). In the previous study, it has been revealed DEX-rich microdroplet tend to entrap the long DNA or filamentous actin (F-actin) in a selective manner [45, 46]. This is caused by the difference of molecular conformation, DEX

have branched structure and PEG have flexible chain [82]. Under the occurrence of phase segregation between PEG and DEX, DEX-rich phase have more nanosized void space than PEG-rich phase. It is expected the microtubules which have filamentous structure (Fig. 4.1(a)) can penetrate the nanosized void space with DEX depleted from the PEG-rich phase of flexible chain.

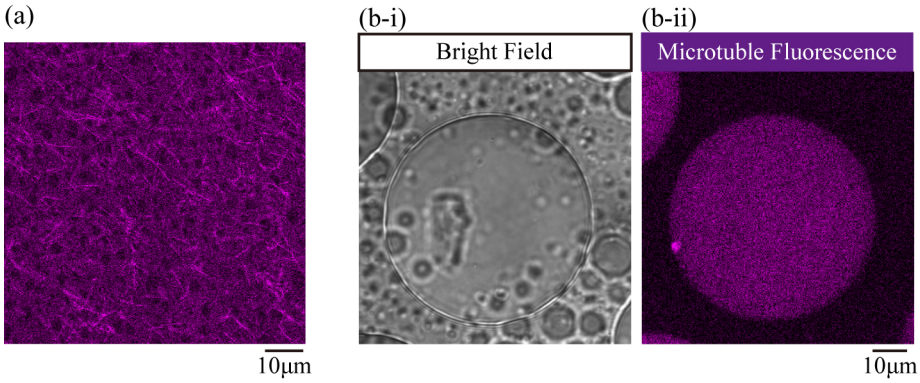


Figure 4.1 Spontaneous localization of microtubules inside the DEX-rich microdroplet. (a) Fluorescent image of microtubules in bulk solution. (b) Microscopic images microtubules in the PEG/DEX binary solution. The composition of PEG:DEX = 5%:5%. (b-i) Microscopic image of transmitted light. (b-ii) Fluorescent microscopic image of microtubules labeled with ATTO 647.

### 4.3.2 Emergence of vortices within the water/water microdroplet

Figure 4.2 indicates the localization of microtubules and kinesins inside the droplet and spontaneous emergence of vortices within the droplet. As shown in Figure 4.2(a), when the microtubule and kinesin mixed to the PEG/DEX binary solution, both molecules are entrapped into the DEX-rich microdroplet in the presence of ATP and $MgCl_2$. To observe the interaction and motility between microtubule and kinesin, ATP and MgCl2 were mixed at the concentration of 10 mM, respectively. The concentration of microtubule and kinesin were 1.8 $\mu$M and 42 nM, which were determined by the previous work [78]. The distribution of microtubules inside the droplet were different, aggregations of microtubules are distributed inside and at periphery of the droplet, whereas mixing microtubules alone, the homogeneous distribution can be observed inside the droplet. Comparing the fluorescent microscopic image of micro-

tubule (cyan) and kinesin (green), there is a strong correlation between the position of each molecule. In other words, it is expected the aggregations of microtubules are emerged together with kinesins and they tend to be entrapped inside the microdroplet.

By the long-term observation, it was found the emergence of vortices inside the droplet. As shown in Figure 4.2(b) shows the superimposed image of the fluorescent microscopic images. The duration of observation was 210 s. Each image of microtubules and kinesin indicates the emergence of convectional flow within the droplet. And, it is suggested the morphology of flow depends on the diameter of droplet. In the case of ca. 100 $\mu$m sized droplet, it was found the two roll vortices are generated inside the droplet. In contrast, in the several times larger sized droplet (200 – 500 $\mu$m), less collective flow was emerged. In addition, several 10 $\mu$m ized small droplets were difficult to entrap the microtubules and kinesins. It is known the DEX-rich phase tends to become larger density than PEG-rich phase under phase segregation [12], DEX-rich droplet tend to touch on the glass substrate, which caused the motile of droplets becoming difficult whereas the vortices were emerged.

Figure 4.3 shows the analysis of the convections inside the droplet. Here, it was focused on the two droplets which are different size and mode of convection. Ca. 500 $\mu$m sized droplet indicated the less collective flow and was named as "droplet 1". On the other hand, ca. 100 $\mu$m droplet indicated two roll vortices inside droplet named as "droplet 2" (Fig. 4.3(a)). At first, the flow around the interface of droplets was shown by spatiotemporal diagram. As shown in Figure 4.3(b-i), the spatiotemporal diagrams were obtained along the continuous line at periphery and the angle was set as shown. Figure 4.3(b-ii) shows the spatiotemporal diagram of each droplet. It was found the similar result was happen between two droplets. The directional flow was emerged to the right side of droplet and shrinkage of microtubules was formed. Moreover, the collective flow of two vortices within the droplet was generated in the case of small droplet, "droplet 1" (Fig. 4.3(c-i)). However, in the case of larger droplet, "droplet 2", it is difficult to align each molecule inside the droplet, and less collective flow was emerged (Fig. 4.3(c-ii)). The vector filed of convection as shown in Figure 4.3(c-i) and (c-ii), were obtained by the PIV method utilizing the plug-in for MATLAB (PIVlab) [83]. In addition, from the present study, the flowing pattern deeply depends on the size of the confinement. That is, the size of cell or cellular organelles is possible to provide some effects for their motile including cytoplasmic

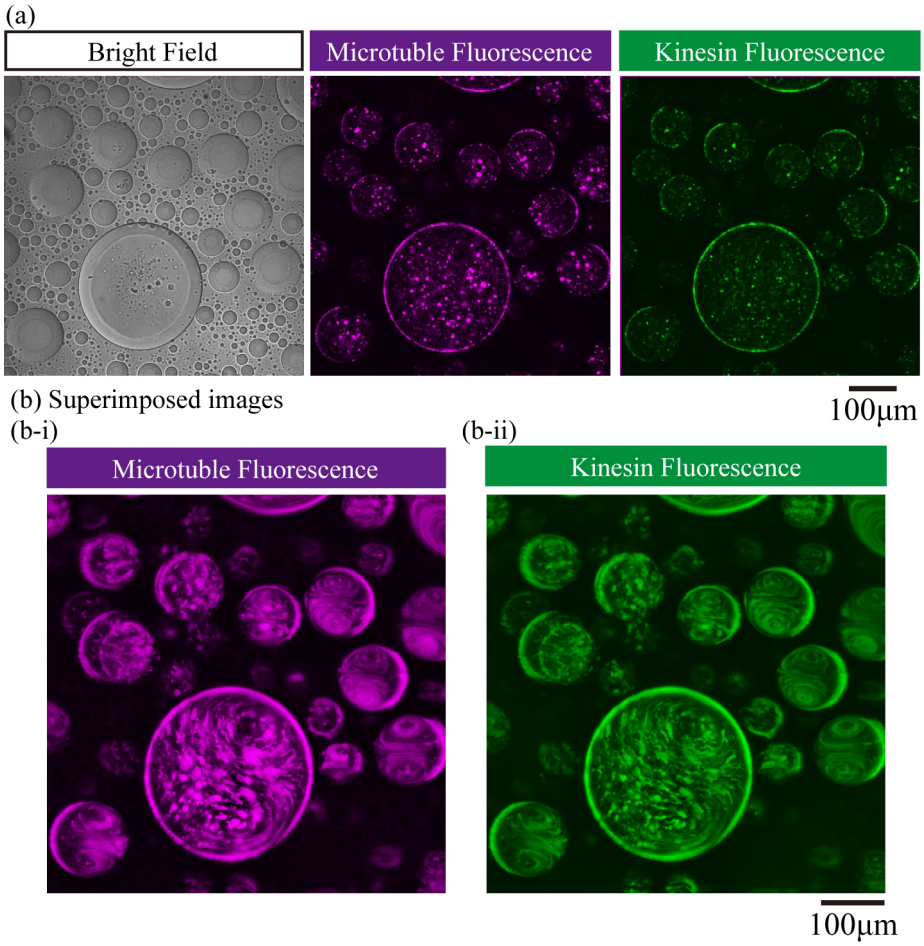


Figure 4.2 Emergence of collective vortices inside the DEX-rich microdroplet. (a) Initial images of fluorescent microscopy. (b) Superimposed images of microtubules (b-i) and kinesin (b-ii). The duration was 840 s. The size dependency of the flowing is occurring.

streaming.

### 4.3.3 Characteristic behavior depending on the volume fraction

To clarify the interaction between microtubule and kinesin within the droplet, the morphological change depending on the volume fraction was confirmed by change the composition of microtubule and kinesin. It was found the four types of motility mode was able to be happen depending on the volume fraction of microtubule and kinesin. Figure 4.4(a) shows the phase diagram depending on the concentrations of micro-

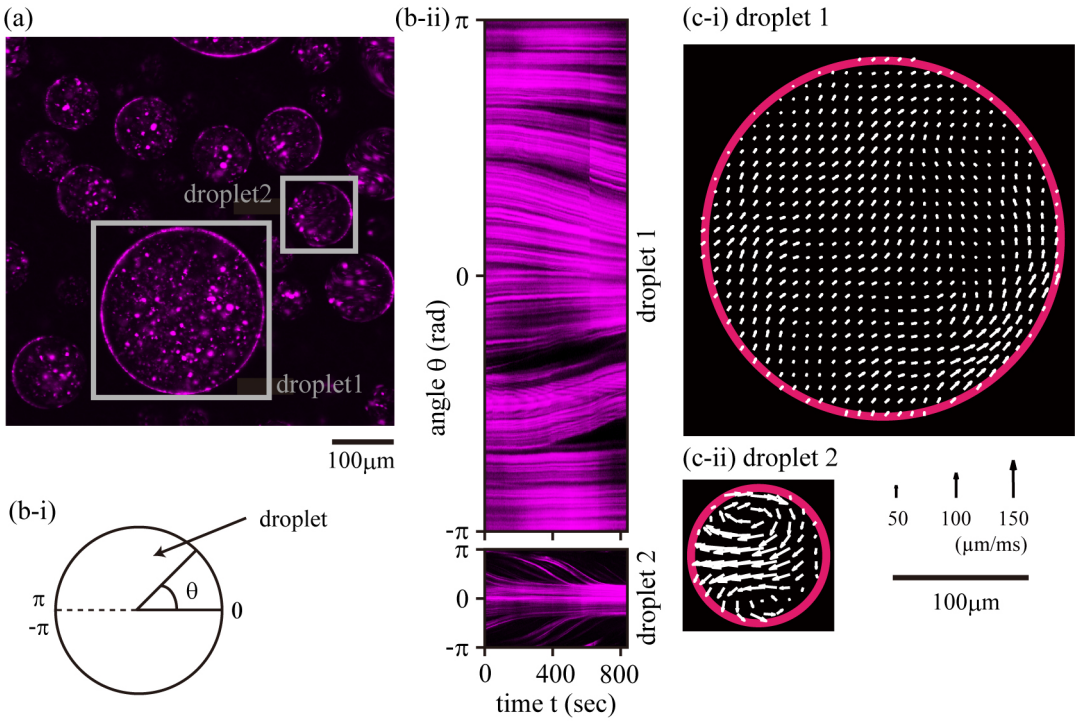


Figure 4.3 Visualization of the convection inside the droplet, which was made by the fluorescent images of microtubule. (a) Snapshot of the fluorescent microscopic image of microtubule. The large droplet is named as "droplet 1" and small as "droplet 2". (b-i) Schematic illustration of the droplet. The angle of spatio-temporal diagram is set as shown. (b-ii) Spatio-temporal diagram of the flow at the vicinity of the interface of each droplet. Upper is "droplet 1". Lower is "droplet 2". (c-i), (c-ii) Flow profiles accompanied by the convection of inside the droplets. The velocity field was analyzed by the PIV, and the velocity of flow corresponds to the size of arrow mark shown above the scale bar.

tubule and kinesin. When we assign the composition of the vicinity of microtubule : kinesin=1.8 $\mu$M:42 nM, most droplets indicate the vortices as shown in Fig. 4.2 (blue circle). The aster shrinkage was happened within the droplets, when it was assigned the higher concentration of microtubule as in Figure 4.4(b) (orange rectangle). On the other hand, the fraction of kinesin becoming higher, random tremor motion can be observed. In the case of both concentrations of microtubules and kinesin become higher or less concentration of kinesin, microtubules and kinesin indicates little activity within the droplet. From these results, it is suggested the volume fraction of microtubules and kinesin is important to formation of the microtubule-kinesin com-

plexes and control of their motilities. As above mentioned, in this study, tetramer kinesin $KIF5B_{head}$-$EG5_{tail}$ was employed and can operate as a cross-linker of microtubules. In addition, under existence of ATP and $MgCl_2$, the cross-linker can provide the sliding motility of microtubule-kinesin complexes. Thus, the volume fraction of microtubule and kinesin is significantly effective within the droplet. It is expected the more detailed effect of appearance these motilities within the droplet become clearer by the theoretical consideration in the future study.

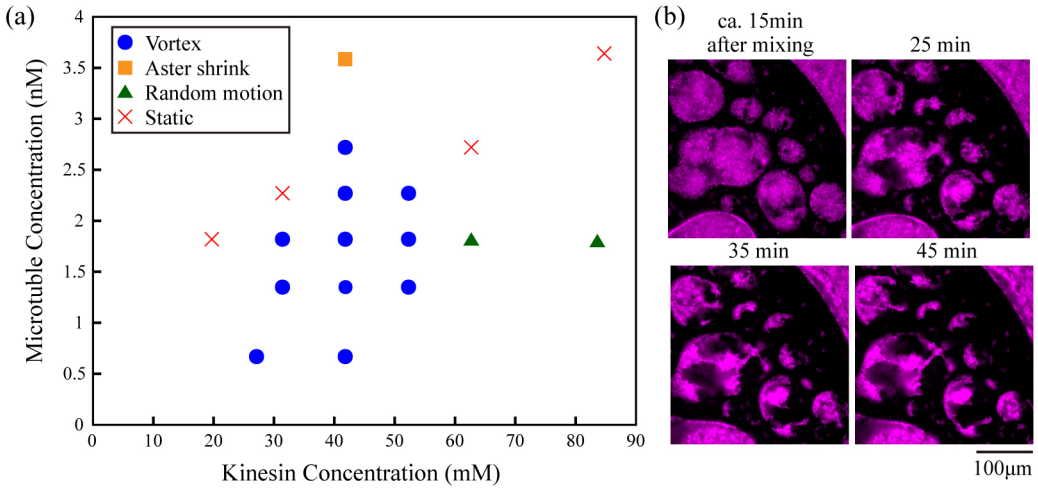


Figure 4.4 Change of motility mode depending on the volume fraction of microtubules and kinesins in the droplet. (a) Phase diagram depending on the concentration of microtubules and kinesin. Four types of behavior were observed. (b) Time dependent change of aster shrinkage of microtubules. Snapshots of the microtubule fluorescent microscopic images were taken every 10 minutes from 15 minute after mixing solution.

## 4.4 Conclusion

In conclusion, it was found that the motor protein, kinesin, or filamentous protein, microtubule, exhibit the specific localization in the cell-sized water/water midrodroples generated thorough the phase separation of binary polymer solution, PEG/DEX. It was revealed the collective vortices within the droplet could be emerged through the sliding motile of microtubule and kinesin. In addition, we employed the tetramer kinesin chimeric $KIF5B_{head}$-$EG5_{tail}$ which have modified from

kinesin of human Eg5. Tetramer kinesin operate as the cross-linker of microtubules. By the observation of fluorescent microscope, the vortices of microtubules and kinesin depend on the size of confinement, the size of droplet. Moreover, the volume fraction of microtubule and kinesin also affect the motile within the droplet including formation of microtubule network and dynamics. It is expected the simple binary polymer system provides the novel aspects to unveil the essential mechanism of the collective motility in side living cells, including spindle dynamics, cytoplasmic streaming and so on.

# Chapter 5

# Negative/positive chemotaxis of a droplet: Dynamic response to a stimulant gas [i, ii]

## 5.1 Introduction

Living organisms on Earth exhibit self-propelled motion or chemotactic behavior in response to external stimuli, where motion is driven by chemical energy under isothermal conditions. In other words, organisms can transduce information into active motion through a process in which external stimuli are recognized as being favorable or unfavorable. This phenomenon is even seen in single living cells that do not have a neural net. In contrast to these observations in living organisms, the ability of human technology to create an artificial chemical system that exhibits dynamic chemotactic behavior is still in its infancy. The spontaneous motion of self-propelled droplets has recently attracted considerable attention in relation to energy transduction by living organisms, i.e., chemo-mechanical energy transduction [26, 84–90]. Various kinds of droplet motion driven by a gradient in interfacial tension have been reported, as well as the propelled motion caused by diffusiophoresis [91,92]. In a related system, an oil-water system composed of an organic phase with potassium iodide and iodine and an aqueous phase containing stearyltrimethylammonium chloride (STAC) exhibits self-agitation at the oil-water interface, accompanied by spatio-temporal nonequilibrium fluctuation of the interfacial tension [20, 21, 93–96]. In addition, the motion of an oil

droplet in an oil/water system has been shown to be chemosensitive [97]. In measurements of the electrical potential at the oil-water interface in a similar system, the nature of the potential fluctuation and oscillation strongly depended on the chemical properties and the concentration [98]. It was proposed that an oil-water system shows reactive spreading on a glass surface with recovery of the surface condition [99, 100]. The spontaneous motion of a self-propelled oil droplet moving on a glass substrate under an aqueous phase has been shown to be limited to the region of the acid-treated glass surface [101, 102]. Here, we report an artificial model system consisting of an oil droplet floating on an aqueous layer that exhibits chemotactic behavior in response to a gas stimulus.

## 5.2 Materials and methods

Figure 5.1(a) shows the experimental system in which a droplet of oleic acid is situated on an aqueous layer with a depth of 1 cm. In this system, ammonia vapor was applied by moving a cotton swab wetted with 28% $NH_3$ liquid (Wako Pure Chemical Industries) close to the oil droplet. Figure 5.1(b) shows an example of the repulsive motion of a 25 $\mu$L oleic acid droplet in response to ammonia vapor, indicating negative chemotaxis.

## 5.3 Results and discussions

To analyze the motion of the droplet in a quantitative manner, we created a spatio-temporal diagram of the droplet image, as shown in Fig. 5.1 (c). The vertical axis shows the distance from point $x = 0$, which corresponds to the center of the original position. Careful inspection of the response of the droplet to ammonia vapor reveals that the footprint of the droplet initially expands while it remains at the initial position for ca. 0.8 sec. This increase in area implies that there is a decrease in interfacial tension at the oil-air and/or oil-water interface. The droplet then accelerates, and finally stops at ca. 4 sec after application of the vapor. Such repulsive motion as exemplified in Fig. 5.1 was confirmed to be highly reproducible. We also noted that the lag-time before the appearance of the escaping motion, e.g., ca. 1 sec in Fig. 5.1(c), tended to increase with an increase in the distance between the floating oil

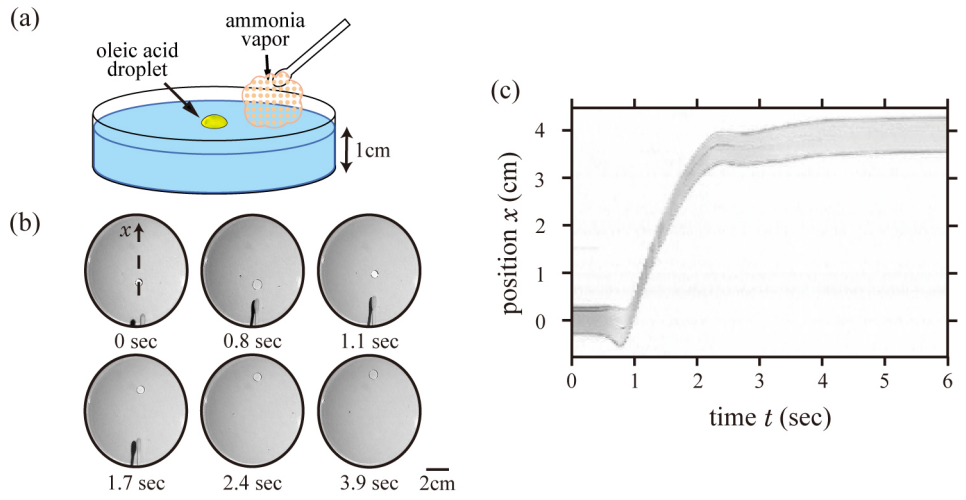


Figure 5.1 Experimental observation of the negative chemotactic behavior of an oleic acid droplet floating on an aqueous solution (a) Experimental setup: ammonia vapor is applied by using a cotton swab wetted with $NH_3$ liquid. (b) Snapshots of an oleic acid droplet moving away from ammonia vapor. (c) Spatio-temporal diagram of droplet motion, where $x = 0$ corresponds to the center of the droplet at the initial position.

droplet and the cotton swab wetted with $NH_3$ liquid.

We performed a time derivation of the time-dependent change in the position of the center of the droplet, and obtained the time course of the droplet velocity $dx/dt$ as shown in Fig. 5.2 (a). Similarly, Fig. 5.2(b) shows the time-dependent change in acceleration $d^2x/dt^2$. We can analyze these time-dependent profiles by using the simple equation of motion in Eq. (5.1):

$$m\frac{d^2x}{dt^2} + \xi\frac{dx}{dt} + f(t) = 0 \tag{5.1}$$

where $m$ [kg] is the mass of the droplet, $\xi$ [Pa·s·m] is the viscosity coefficient, and $f(t)$ [N] is the driving force. We can reasonably assume that the velocity profile at the point at which acceleration switches from positive to negative is given under the condition $f(t) \approx 0$. Thus, from curve-fitting with a single exponent over the portion of the curve with a decrease in velocity ($t > 1.2$ sec), we evaluated the effective viscosity $\xi$ by using a value of $m = 22 \times 10^{-6}$ kg for 25 $\mu$L oleic acid (density: 0.89 g/cm$^3$). With this value of $\xi$, we can evaluate the time-dependent change in the driving force, as shown in Fig. 5.2(c). In the figure, the apparent force $f(t)$ is almost null expect

for the period between 0.5 and 1.0 sec, which supports the validity of our analysis based on the rather simple kinetic equation in Eq. (5.1). Note that the actual friction has two different origins; usual fluidic friction at a mesoscopic scale and molecular friction due to absorbance and desorption at the interface [102]. In a future study, it may be of interest to evaluate the origin of the apparent friction based on careful measurements.

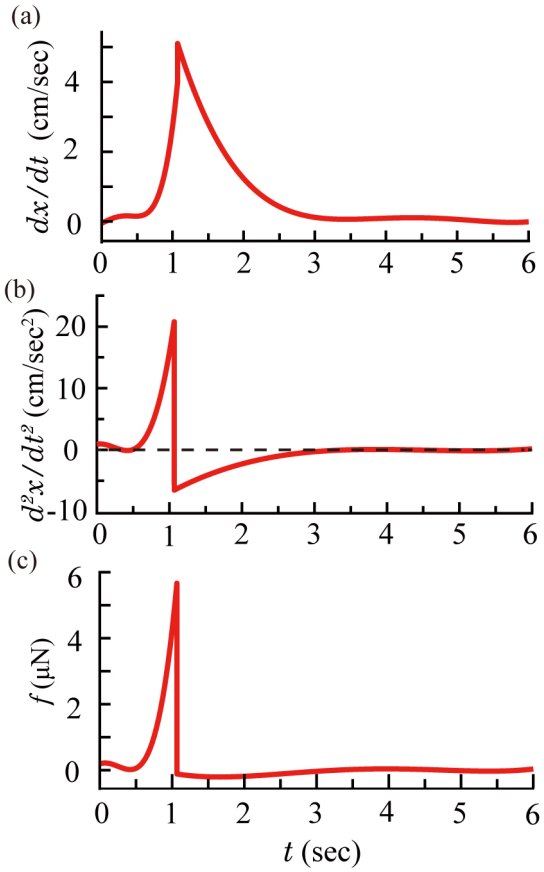


Figure 5.2 Time-dependent characteristics of repulsive motion of the droplet shown in Fig. 5.1. (a) and (b) Profiles of the velocity and acceleration of the droplet evaluated through the time derivative and second-derivative, respectively, of the spatio-temporal diagram in Fig. 5.1(c). (c) Profiles of the propelling force evaluated from an analysis of the time-dependent changes in velocity and acceleration, by adapting a phenomenological kinetic equation: $m\frac{d^2x}{dt^2} + \xi\frac{dx}{dt} + f(t) = 0$.

Next, to clarify the mechanism of the stimulus-induced vectorial motion of the droplet through observation of the aqueous layer, we monitored the motion of

polyethylene beads floating on the surface to visualize surface flow (see Fig. 5.3(a), where the average diameter of the polyethylene particles is 180 $\mu$m (CL-2507, Sumitomo Seika Chemicals Co., Ltd.)). Figure 5.3(b) shows representative profiles of surface flow for the three stages of motion: induction stage (0.8 sec), running stage (2.0 sec) and stopping stage (5.4 sec). The velocity field of the flow was obtained with the Particle Image Velocimetry (PIV) plugin for MATLAB. In the induction stage, the surface layer flows toward the stimulant gas. In this stage, the droplet tends to expand on the surface layer, as shown in Fig. 5.1. In the running stage, the direction of flow is almost opposite that in the induction stage, suggesting that the repulsive motion of the droplet coincides with the direction of flow. In the stopping stage, the directional surface flow tends to decay gradually. Figures 5.3(c) and (d) show flow profiles in the bulk aqueous solution, where the aqueous layer was prepared by the addition of small amount of 0.5 $\mu$M of hydrophilic red dye (Ponceau 4R; trisodium (8Z)-7-oxo-8-[(4-sulfonatonaphthalen-1-yl)hydrazinylidene]naphthalene-1,3-disulfonate, available from Kyoritsu Foods Inc.) to distilled water to clearly visualize the system. To visualize the internal flow of the aqueous phase, the red dye was not thoroughly mixed in the water. In contrast to the profiles regarding surface flow, there is very little motion of the liquid inside the aqueous layer. Based on these observations, the driving force of the running droplet is most likely the force acting at the interface, i.e., the gradient of the surface tension should act as the driving force for the vectorial motion of the droplet.

Figure 5.4 shows a schematic representation of the mechanism by which the droplet moves away from the gas stimulus. With the application of ammonia vapor, the oleic acid located at the oil/air interface undergoes an acid-base reaction. The ionized molecules of oleic acid decrease the oil/air interfacial tension, and then cause flattening of the droplet as exemplified in the initial stage of vapor application at around 1 sec. Successively, the negatively charged oleate molecules, through the binding of $NH_3$ to the carbonyl group, tend to spread onto the water/air interface, and this phenomenon would be more prominent on the side closer to the vapor source. Thus, the water/air interfacial tension decreases on this side. As a result, there is a large difference in interfacial tension between the sides of the droplet, and this propels the droplet to move away from the vapor source. The significant fluidic flow on the surface of the aqueous layer (Fig. 5.3(b)) and the stationary bulk phase (Fig. 5.3(d)) support the

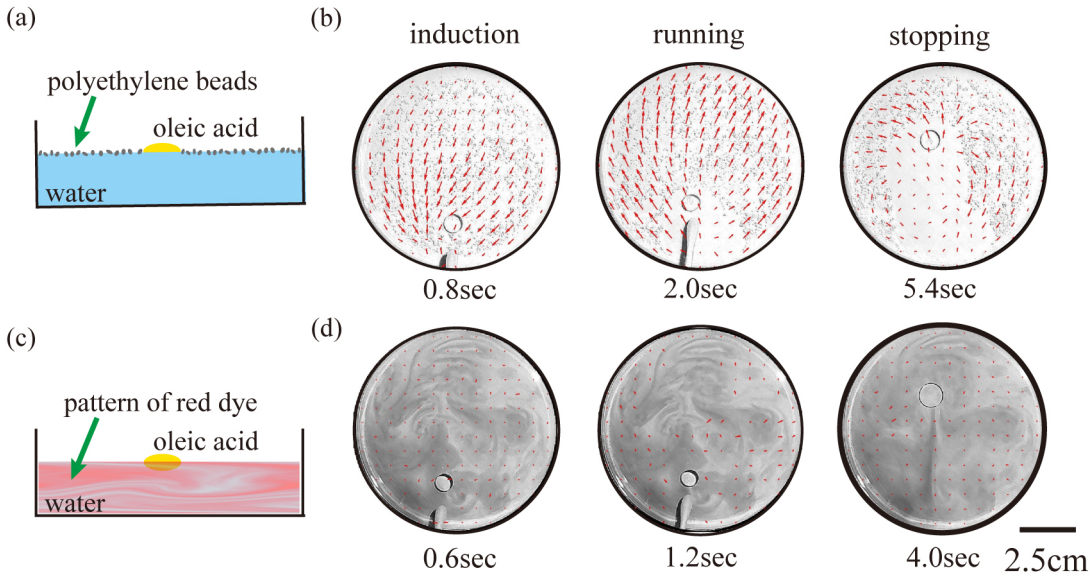


Figure 5.3 Flow profiles accompanied by the generation of chemotactic behavior. (a) Schematic representation of the system for observing interfacial flow. (b) Surface flow obtained by an analysis of the velocity field with the PIV plugin for MATLAB visualized by polyethylene beads. (c) Schematic representation of the system for observing internal flow. Internal flow was visualized with the use of a hydrophilic red dye. (d) Velocity field analyzed with PIV by measuring the deformation of the diffusion pattern of the dye.

validity of this mechanism.

Figure 5.5 shows the attractive motion or positive chemotaxis of a 25 $\mu$L aniline droplet floating on an aniline-saturated aqueous phase. With the application of hydrochloric acid vapor, the droplet tends to approach the vapor source. In this experiment, we consider that aniline molecules tend to form a monolayer at the water/air interface in the absence of the vapor. The contact angle of the aniline droplet is relatively small compared to that in the experiment with oleic acid as shown in Fig. 5.1. In this case, the interfacial tension close to the gas stimuli is considered to increase because the positively charged aniline complexed with hydrochloric acid tends to dissolve into the bulk aqueous layer, i.e., a gradient of interfacial tension is generated between the sides of the droplet. Thus, we can explain the positive chemotaxis of the aniline droplet caused by exposure to the acidic gas.

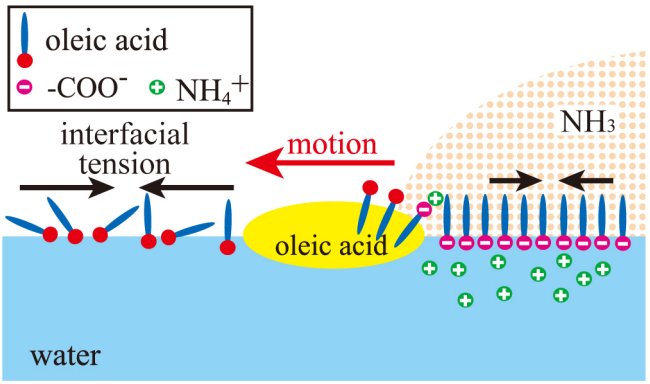


Figure 5.4 Proposed mechanism of the negative chemotactic behavior of an oleic acid droplet. The gradient of interfacial tension drives the droplet away from the stimulating gas, resulting in negative chemotactic behavior.

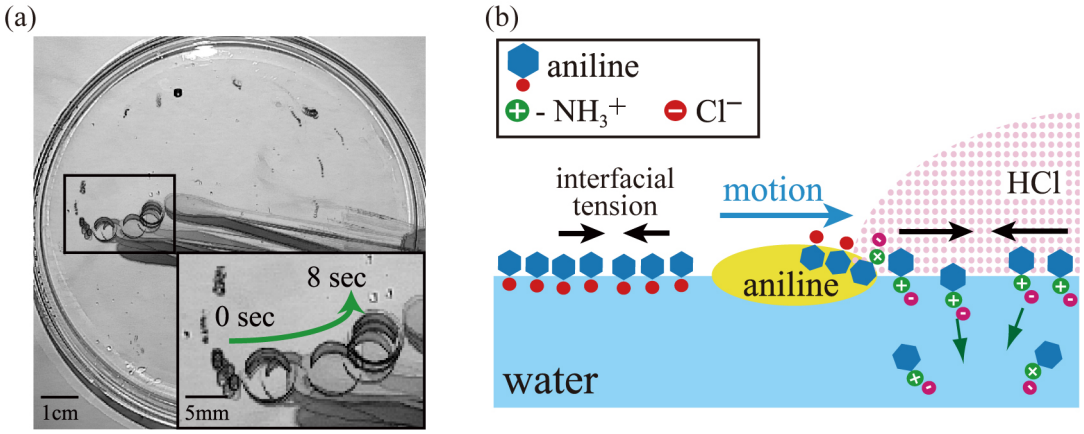


Figure 5.5 Positive chemotactic behavior of an aniline droplet vs. HCl vapor. (a) Superimposed image of the aniline droplet moving toward the HCl vapor, supplied by a cotton swab wetted with hydrochloric acid solution (37%). (b) Proposed mechanism of the positive chemotactic behavior of the aniline droplet.

## 5.4 Conclusion

We have described the negative and positive chemotaxis of an oil droplet floating on an aqueous phase. Negative chemotaxis is observed for a droplet with a weakly acidic molecule, i.e., oleic acid, stimulated by the relatively strong alkaline vapor of $NH_3$. In contrast, positive chemotaxis is generated for the combination of a weakly alkaline oil and the strong acidic vapor of HCl. Based on these findings, we strongly suspect that

negative/positive chemotaxis could be controlled by considering the acidity/basicity of the droplet and the stimulating gas, together with the hydrophobicity of the chemical components of the droplet. It would be interesting to examine this hypothesis in future studies.

# Chapter 6

# Self-synchronous swinging motion of a pair of autonomous droplets [iii, vii]

## 6.1 Introduction

Living organisms maintain their lives through the dissipation of chemical energy under isothermal conditions. Through a long evolutionary process, organisms have developed a 'technique' to generate macroscopic motion by diminishing the effects of large fluctuations, Brownian motion, inherent to individual molecular components with a length-scale of nm, i.e., motor proteins. On the other hand, humans are adapting the approach by using rigid bodies to obtain macroscopic mechanical motion, by suppressing fluctuation to achieve energy transduction. The realization of self-regulated macroscopic motion using chemical energy with a non-rigid body under mild conditions is a long-standing target of research and still remains an interesting subject. Recently, numerous studies have been undertaken to generate self-propelled motion on a macroscopic scale driven by thermodynamic non-equilibricity [103–106], including chemical reactions [101,107–110], transfer of a chemical substance [23,24,28,111–127], a temperature gradient [128–131], photo irradiation [107,132–135], external vibration [136], stationary electrical potential [137] and so on. These studies have revealed that various kinds of regular motion can be generated under the introduction of symmetry-breaking to the experimental system, in terms of either the shape of the objects or on the environmental boundary conditions [105]. In an experimental system with active droplets, fluctuation of the interface, or interfacial instability, due to the

Marangoni effect has been proposed to cause specific macroscopic motions. It has been reported that irregular agitation induced by a chemical Marangoni effect can be transduced into characteristic repetitive up-down or rotational motion, simply by choosing appropriate boundary conditions [22, 23, 114]. For example, Sumino et al. found that an oil droplet exhibits rhythmic back-and-forth (reciprocating) motion under geometrical constraint with a narrow rectangle shape, whereas it undergoes random motion in an isotropic environment [23].

In the present study, we performed an experiment on the interference between a pair of active droplets undergoing back-and-forth the motion on a waterway with a narrow rectangle shape. The droplets exhibit a swinging type of synchronization when a glass capillary is placed at the midpoint of the waterway.

## 6.2 Results and discussions

Figure 6.1(a) shows the experimental system, where a pair of droplets of nitrobenzene (density: 1.2 g/cm$^3$) with the same volume (100 $\mu$L) are situated on an aqueous phase by use of a pipette. In our experiments, all of the chemicals were analytical grade and were purchased from Wako Pure Chemical Industries, Ltd. All of the experiments were carried out at room temperature ($24 \pm 2$ °C). It has been found that heavy oil droplet, such as nitrobenzene and aniline, can float on aqueous solution by avoiding the sinking-down onto the bottom because of the supporting effect of the interfacial tension and tend to exhibit active self-propelled motion driven by Marangoni instability [20, 22, 23, 114]. Before the investigation on the interference of the self-propelled motion of the couple of droplets, we have explored the effect of chemical compositions of the aqueous phase on the self-propelled motion; for example, we have explored the effect of chemical compositions of the aqueous phase on the self-propelled motion, by adding various chemical species, such as sodium chloride, sucrose, quinine chloride and acetic acid, at different concentrations. As the result, we found that the self-propelled motion of a nitrobenzene droplet becomes most vivid when sub-molar concentration of acetic acid is added to the aqueous solution. Thus, Thus, in the present study, we adapted acetic acid solution to observe the spontaneous motion of oil droplets and confirmed that regular back-and-forth reciprocating motion is generated in a reproducible manner. To observe the interference between the

droplets undergoing back-and-forth motion, we placed a glass capillary ($\phi = 1.8$ mm for the part dipped into the waterway) at the middle of the waterway, as depicted in the Fig. 6.1(a). In the absence of a glass capillary on the waterway, the droplets tend to merge each other to form a single droplet through the collision. With a capillary, the twin droplets exhibit the back-and-forth motion remaining each other on the left and right chambers without fusion. Figure 6.1(b) shows images of the droplets taken at 1-s intervals, revealing that the droplets exhibit swinging-type synchronization.

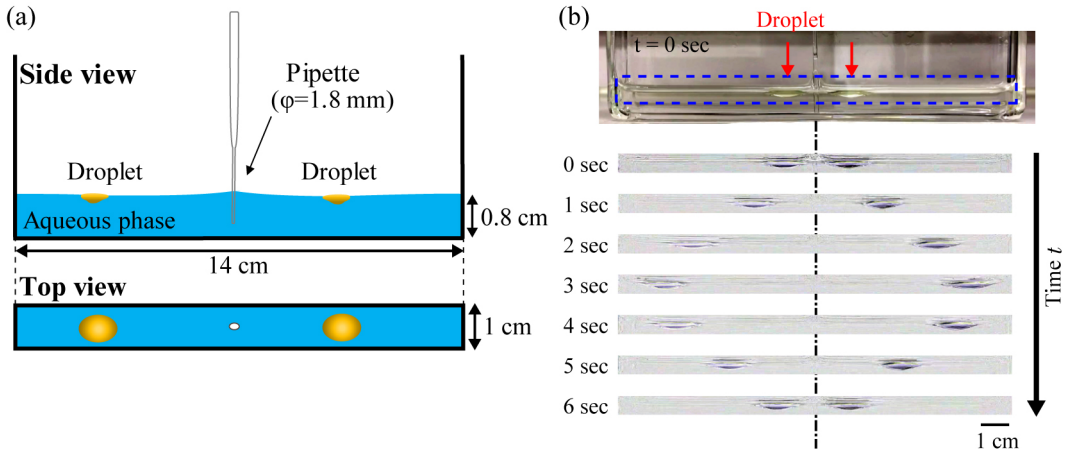


Figure 6.1 A pair of oil droplets exhibiting self-propelled motion on an aqueous phase in a narrow rectangular vessel. (a) Experimental setup: Two droplets of nitrobenzene (each 100 $\mu$L) were situated on an aqueous phase of 0.3 mol/L acetic acid. A pipette was inserted at the midpoint of the waterway. The droplets began to exhibit translational motion immediately after contact with the aqueous solution. (b) Upper image: Side view of the experimental setup. Lower image: Snapshots of the swinging droplets at 1-s intervals.

### 6.2.1 Synchronous oscillatory motion of two droplets

Figure 6.2 shows spatio-temporal diagrams for droplet motion. As shown in Fig. 6.2(a1), the droplets undergo 1:1 swinging-type synchronization, where a narrow pipette ($\phi = 1.8$ mm) was put at the middle of the waterway in the experiments as depicted in Fig. 6.1. When the intervening narrow pipette was replaced by the thick glass rod ($\phi = 5.0$ mm), the droplets exhibit unsynchronized motion. It is noted that replacement of the interference barrier of the narrow pipette by the glass rod

with wider diameter causes the coupling strength between the self-moving droplets to be weaker. The difference in the interference mode of coupled motion can be depicted as a phase diagram, as shown in the lower panels in Fig. 6.2. For 1:1 synchronized motion, the trajectory shows a regular loop along a straight line with a slope of unity (Fig. 6.2(a2)). Figure 6.2(c1) shows the spatio-temporal diagram when the intervening pipette was positioned on the right side of the waterway, revealing the appearance of 2:1 synchronization of back-and-forth motion. Recently, we have reported that the up-down self-propelled motion for a floating oil droplet by prohibiting translational motion by use of thin glass rod [138]. It was found that a pair of neighboring droplets undergo in-phase synchronization. Such an experimental trend was argued in terms of the Marangoni effect under gravitational instability for a heavy oil droplet. The mode of the synchronization of the swinging-type motion in the present study is regarded to correspond to the in-phase synchronization on the up-down motion of two droplets.

### 6.2.2 Numerical simulation

To clarify the mechanism that underlies the synchronized motion of the two droplets, we performed a numerical study based on a simple theoretical model. We adopted a model for self-propelled directional motion on a quasi-one-dimensional waterway, as in a previous study [23]:

$$m\frac{d^2x}{dt^2} = \eta\left(1-\alpha\left(\frac{dx}{dt}\right)^2\right)\frac{dx}{dt} + [\text{mutual interaction}] + [\text{boundary effect}] \qquad (6.1)$$

where $m$ denotes the mass of the droplet, $\eta$ the viscosity of water and $\alpha$ the ratio between the driving force and viscous damping. In our modeling, we omitted the noise term used in the previous study [23] to abstract the essential quality of the self-propelled motion through simplification of the differential equation. Equation (6.1) implies that the self-propelled motion is a phenomenon generated under thermodynamically open conditions, i.e., competition between the driving force and viscous damping.

Next, we consider the motion of the droplets on the left and right sides of the waterway by using dimensionless positional variables, $x_1$ and $x_2$, corresponding to

the left and right droplets, respectively:

$$\begin{aligned} m\frac{d^2x_1}{dt^2} &= \mu_1\left(1-\alpha\left(\frac{dx_1}{dt}\right)^2\right)\frac{dx_1}{dt}+\frac{\gamma}{(x_2-x_1)^2}-\frac{\partial U}{\partial x_1} \\ m\frac{d^2x_2}{dt^2} &= \mu_2\left(1-\alpha\left(\frac{dx_2}{dt}\right)^2\right)\frac{dx_2}{dt}+\frac{\gamma}{(x_2-x_1)^2}-\frac{\partial U}{\partial x_2} \end{aligned} \tag{6.2}$$

where $\mu_1$ and $\mu_2$ are parameters that determine the period of back-and-forth motion, and they are set to ca. 0.35. The value of $\alpha$ is set to 0.26. The variables of $x_1$ and $x_2$ are defined as negative and positive, respectively. Thus, the differential equations on $x_1$ and $x_2$ in Eq. (6.2) are symmetric with respect to each other. The second term on the right side of Eq. (6.2) represents the interaction between the two droplets. Here, we simply assumed that the interaction between two droplets is inversely proportional to the square of the distance between them [22]; thus the interaction is effective only when the distance between them is short and tends to induce in-phase motion. The last term of Eq. (6.2) represents the boundary effect, or potential energy of the vessel wall and barrier of the inserted capillary or rod. We chose these values to reproduce the stable translational motion of the droplets.

$$U=\begin{cases} k(x-a)^2, & 0\le|x|\le a \\ 0, & a<|x|\le b \\ k(x-b)^2, & b<|x| \end{cases} \tag{6.3}$$

The potential energy $U$ is schematically depicted in Fig. 6.3(a2) – (c2), where we consider the repulsive effect due to the meniscus near the glass wall and inserted pipette/rod. We adopted the parameters for the boundary effect, $k = 80$, $a = 0.25$, $b = 6.75$, to roughly reproduce the geometry of the meniscus around the hydrophilic glass wall. Figure 6.3(a1), (b1) show the results of the numerical simulation when the waterway is divided at the midpoint. To check for the ap6.3(b1) shows the unsynchronized state, where the interaction parameter is smaller: $\gamma = 0.1$. Figure 6.3(c1) shows the appearance of 2:1 synchronization, where the waterway is divided 2:1, suggesting a reproduction of the experimental trend in Fig. 6.3(c2). Except for the placement of the barrier, the parameters for 2:1 synchronization are the same as those for 1:1 synchronization. In our simple model equations, the important spatial variables were not included such as size and morphology of the droplets, and width and depth of the waterways. It is noted that, through such very simple mathematical

modeling, the essential features on the behavior of a pair of the self-propelled droplets have been well reproduced.

## 6.3 Conclusion

In summary, we have clarified that the synchronized swinging motion of a pair of droplets is generated in a spontaneous manner. When we vary the relative length of the waterway as a control parameter, the mode of synchronization changes from 1:1 to 2:1. It may be interesting to extend the experiments to produce other types of synchronized motion, such as mode coupling with more than two droplets and the interaction of different-sized droplets. These studies are expected to contribute to the development of a system that exhibits self-organized motion working driven by chemical non-equilibricity under isothermal condition.

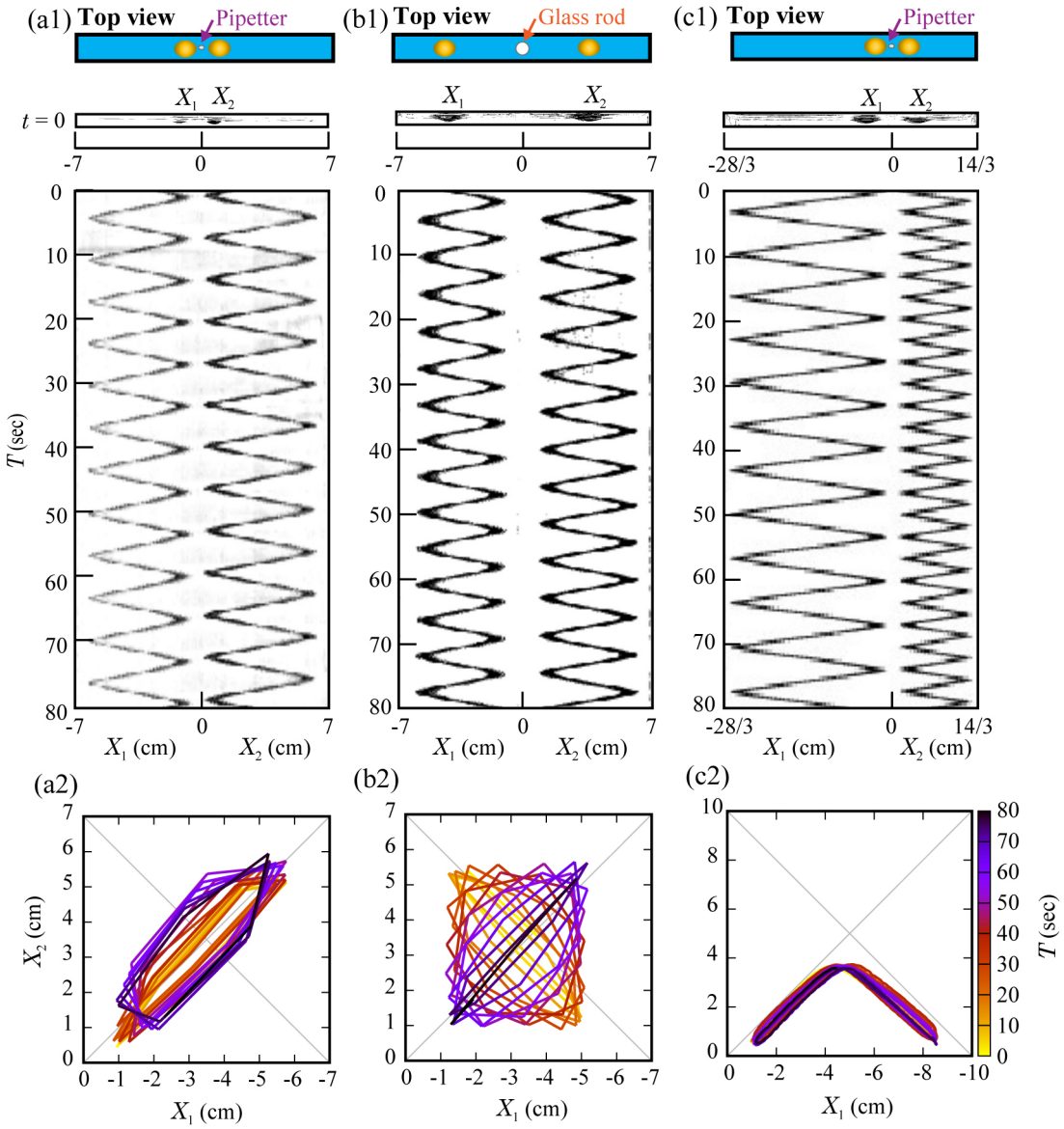


Figure 6.2 Analysis of the oscillatory motion of the two droplets. Upper part: Spatio-temporal diagram based on data regarding movement of the droplets. (a1) Swinging motion with 1:1 synchronization where a pipette with the diameter of 1.8 mm is inserted at the midpoint of the waterway. (b1) Out of synchronization under the same conditions as in (a1) except for the intervening object; a glass rod was positioned at the midpoint. (c1) 2:1 Synchronization when the narrow glass pipette was shifted toward the right. (a2) - (c2) Correlation diagrams between the motions of the left and right droplets, $X_1$ and $X_2$, respectively. For all of the experiments, the volume of the droplets was 100 $\mu$L and the aqueous phase was 0.3 mol/L acetic acid solution, using the waterway shown in Fig.6.2(a).

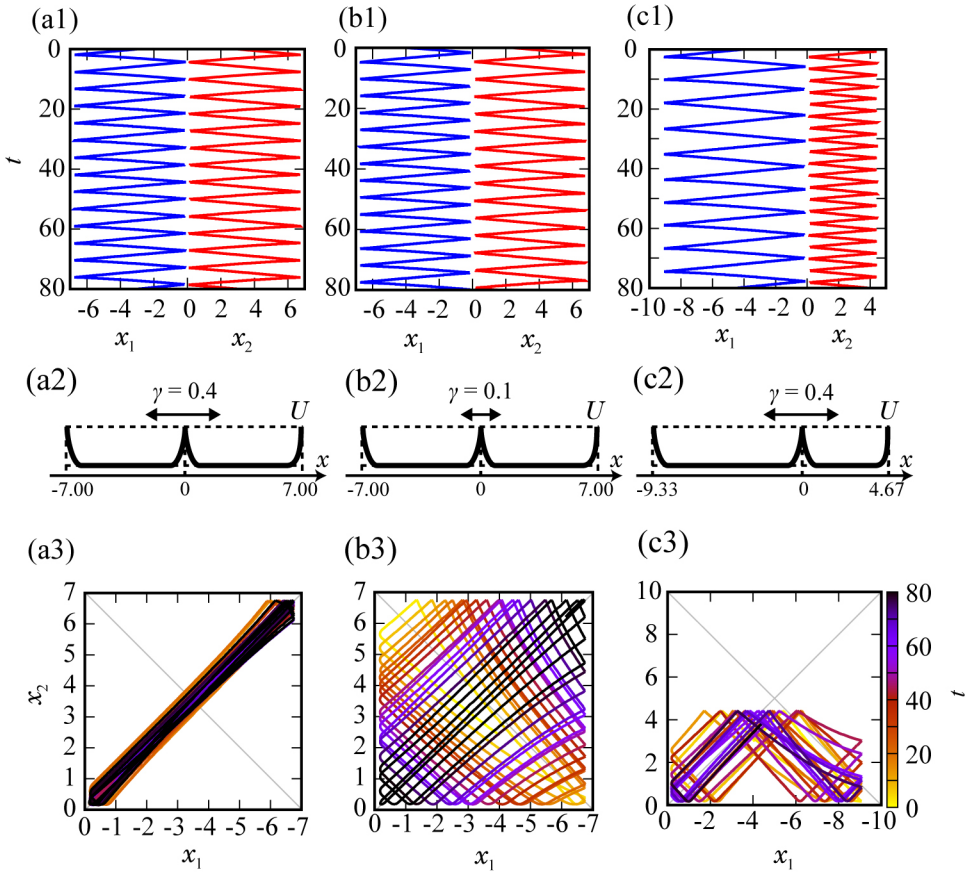


Figure 6.3 Numerical simulation of the motion of a pair of droplets calculated with Eq. (6.2); the values of the parameters are given in the text. (a1) 1:1 Synchronization when the strength of the interaction parameter is $\gamma = 0.4$ at the middle of the waterway. (b1) Out of synchronization when the strength of interaction is smaller; $\gamma = 0.1$. (c1) 2:1 Synchronization when the intervening barrier is shifted to give a 2:1 ratio for the respective lengths of the waterway under conditions similar to those in (a2). The result of numerical simulation for t=[0,100], where the time step is 0.01. (a2) - (c2) The profiles of the potential function $U$, where $x_1, x_2 = 0$ corresponds to the position of the glass pipette or rod, and the edges on the left and right correspond to the position of the walls of the vessel. Around the vicinity of the boundary, we considered the effect of the meniscus as explained in the text. (a3) - (c3) Correlation diagram of between the left and right droplets denoted as $x_1$ and $x_2$, respectively.

# Chapter 7

# Emergence of pendular and rotary motions of a centimeter-sized metallic sheet under stationary photoirradiation [iv]

## 7.1 Introduction

Living organisms on Earth maintain their lives under thermodynamically open conditions through the use of energy from the sun. There has recently been considerable interest in clarifying the mechanisms that underlie the emergence of regular motion in dissipative systems. Through recent studies on the self-propelled motion of both living organisms and artificial living material, it has become clear that irregular self-propelled motion can be converted to regular motion through the introduction of geometrical asymmetry [20, 25, 77, 139–141]. For example, it was reported that the direction of translational motion is determined by the introduction of anterior-posterior asymmetry to either a chemical property or the physical structure of an object, and rotational motion is observed for an object with a rotationally asymmetric shape [142–146]. Furthermore, the emergence of regular motion in self-propelled particles through spontaneous symmetry-breaking has attracted increasing interest, with regard to both physics and biology [103, 147–150].

In the present study, we focused on the motion induced by the instability of a

solid/liquid interface, i.e., a spatio-temporal change in the interfacial free energy or interfacial tension. It is well known that a spatial gradient of interfacial tension due to a thermal or chemical inhomogeneity at the interface can generate macroscopic agitation. This agitation can cause liquid flow known as Marangoni flow [151–153]. Interestingly, it has been reported that the macroscopic motion of a droplet or bubble can be induced accompanied by Marangoni instability or interfacial instability, under stationary dissipative conditions, including the experimental systems with photo-irradiation [100, 115, 133, 134, 154–161]. Here, we study the generation of regular motion on a metallic sheet induced by Marangoni convection under local heating with a spatially-fixed CW laser. We found that, with a change in the magnitude of irradiating laser power, a hammer-shaped object undergoes periodic pendular motion. In addition, a metal sheet entrapped with an oil droplet undergoes regular rotational motion, where the direction of rotation is determined by the geometric symmetry of the sheet.

## 7.2 Experimental methods

An aluminum (Al) sheet with a thickness of 11 $\mu$m was obtained from Toyo Al Echo Products Co., Ltd. (Japan; Foil Roll Black for Broiling Potatoes). Oleic acid was purchased from Nacalai Tesque (Kyoto, Japan). A CW laser (532 nm) was obtained from OXIDE Co. (Tokyo, Japan; LS03TT-M01). Experiments were performed at a room temperature of 18 °C. The motion of the Al sheet was captured by a digital video camera (Panasonic Co., Osaka, Japan; HC-600M) and a thermal-camera (FLIR Systems Japan, Tokyo, Japan; FLIR T420). The recoded motion of the Al sheet was analyzed using ImageJ and Kinovea image-analysis software. To ensure that photons were absorbed effectively, we used the black-painted side of the Al sheet for the experiments. For the experiments on the generation of selective rotary motion (see Figures 7.5 and 7.6), we coated the surface of the Al sheet with black paint containing carbon black and poly(methyl methacrylate-co-butyl methacrylate) (Tamiya Ink Co., Japan; TS-14).

## 7.3 Results and discussions

### 7.3.1 Pendular motion under the stationary photoirradiation

Figure 7.1 shows pendular motion under irradiation by a laser at a spatially-fixed position. The Al sheet was hammer-shaped, as shown in Figure 7.1(A). In the experiment, the end of the "handle" of the hammer-shaped sheet was bent at a right angle to form a small triangle, as depicted in Figure 7.1(A), which was positioned to be parallel to the wall of the experimental container. Figure 7.1(B) shows snapshots and spatio-temporal diagrams of the pendular motion of the object under stationary laser irradiation at a laser power of 0.45W. The lower panel of Figure 7.1(B) shows a spatio-temporal diagram of the rhythmic pendular motion, where the middle panel shows a time-expansion of the diagram for rhythmic motion. The spatio-temporal diagram indicates that the object maintains its pendular motion under stationary laser irradiation and the period of this motion is on the order of 3 s.

Figure 7.2 shows the dependence of the pendular motion on laser power; Figure 7.2(A) exemplifies the time-dependent change in the angle $\Delta\theta = \theta - \theta_0$ of laser-induced motion of the hammer-shaped object. Figure 7.2(B) shows a definition of the angle $\theta$. The amplitude of the curve on the vertical axis of Figure 7.2(A) is the change in $\theta$ from its initial value $\theta_0$ ($\theta_0 \approx 11$ radian). In these experiments, we set the initial condition so that the handle of the hammer-shaped object was in contact with the wall of the container. Figure 7.2(C) shows how the mode of movement of the object varies with the laser power; i) stationary state without any moment (0 – 0.37 W), and ii) rhythmic motion (0.37 W – 0.5 W). Above a power of 0.5 W, the object again entered a stationary state without rhythmic motion. The transition from stationary to rhythmic states at a power of around 0.35 W was abrupt or discrete, as shown in Figure 7.2(C).

Figure 7.3(A) shows the temperature distribution around the object as observed by an IR thermometer after 0.7, 6.2, 6.7 and 7.9 s, and th e corresponding spatio-temporal diagram during rhythmic motion. The diagram clearly shows periodic heating of the hammer-shaped object coupled with periodic motion, i.e., movement of the object away from the laser spot is enhanced when the temperature of the object increased.

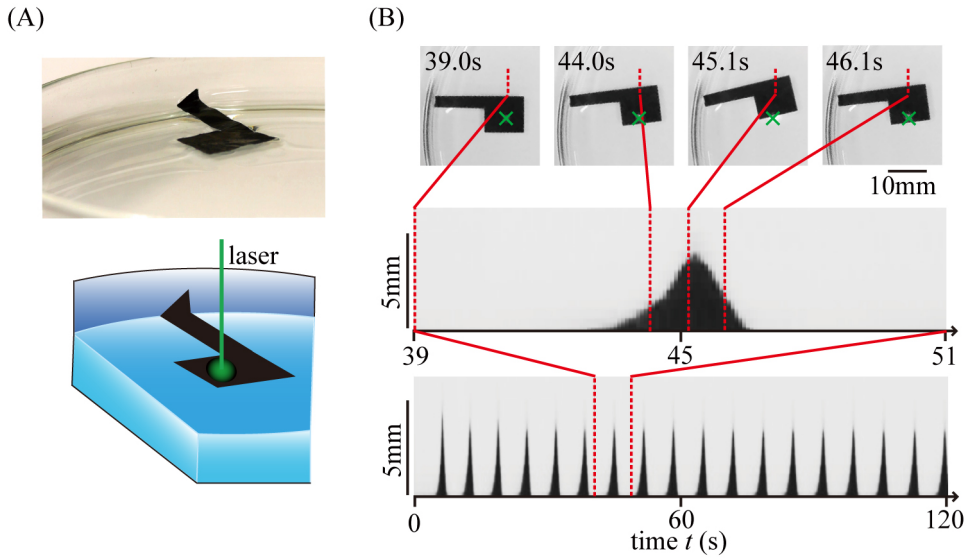


Figure 7.1 Pendular motion of a hammer-shaped aluminum sheet. (A) Photograph and schematic representation of the experimental system, where a hammer-shaped black aluminum (Al) sheet is floating on an aqueous phase. (B) Bottom: Spatio-temporal diagram of pendular motion, where $t = 0$ corresponds to the initiation of laser irradiation. Middle: Expansion of time-axis on the spatio-temporal diagram. Top: Images of the motion of the hammer-shaped object, where the green cross indicates the position of the laser spot.

Based on the above experimental results, we propose a mechanism for the pendular motion induced by laser irradiation, as shown in Figure 7.3(B). It is well known that a temperature gradient around a water/air interface leads to a gradient of interfacial tension in that area. This means that the tension at a lower temperature, $\gamma_L$, is greater than that at a higher temperature, $\gamma_H$. Due to this spatial gradient of the interfacial tension, the "head" of the hammer moves away from the region of higher temperature, as shown in Figure 7.3(A). Another important factor in the periodic motion is the presence of a meniscus between the handle of the hammer and the glass vessel. When the hammer-shaped object moves away from the laser spot, the meniscus tends to make the object return to its initial position, like a spring. The competition between the driving force generated by laser irradiation and the restoring force exerted by the meniscus generates the observed pendular motion of the sample. Thus, the mechanism of pendular motion can be summarized as follows: First, the head of the hammer-shaped object moves due to laser irradiation while maintaining

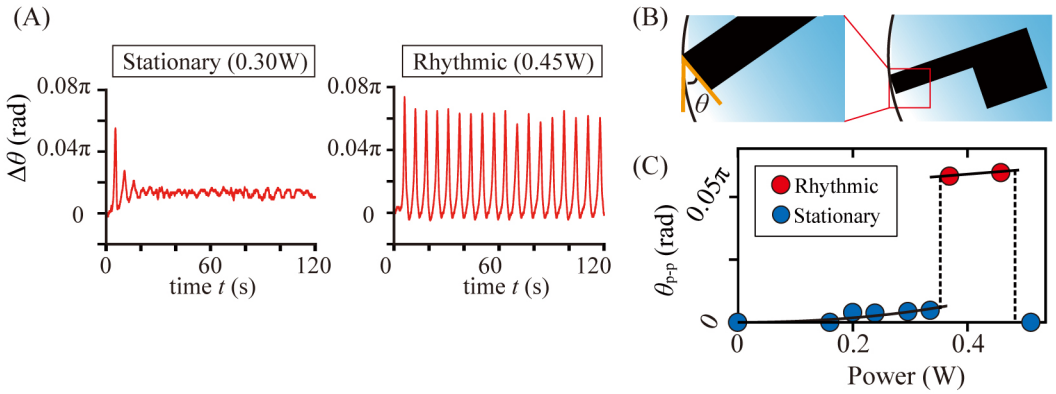


Figure 7.2 (A) Time-dependent change in the contact angle ($\Delta\theta$), just after the start of laser irradiation, for the motion of a hammer-shaped Al sheet. (B) Schematic illustration to show the change in angle $\theta$. (C) Bifurcation diagram of the dynamic behavior of the hammer-shaped object, depending on the laser power. $\theta_{\text{p-p}}$ corresponds to the peak-to-peak amplitude of $\Delta\theta$ in Fig. 7.2(A). With an increase in laser power, the mode changes from 'stationary' to 'rhythmic'. With a further increase in power, the object is repelled away from the laser focus and attaches to the periphery of the glass vessel in a stationary manner.

contact between the sample and the container wall. Next, the sample moves away from the focus of the laser due to the motion of the sample driven by laser irradiation. This means that the driving force of laser irradiation works by increasing the temperature of the sample. The restoring force exerted by the meniscus then returns the sample back to its initial position before laser irradiation. The competition between these forces leads to the pendular motion of the sample.

### 7.3.2 Numerical simulation of pendular motion

Based on the above results and discussion of pendular motion caused by laser irradiation, we propose a simple numerical model for this oscillatory motion. To express the essence of the mechanism of pendular motion, we use only two variables: $\theta$, the angle of the long-axis of the hammer with respect to the wall of the outer vessel as shown in Figure 7.2(B); and $\tau$, the temperature normalized to room temperature.

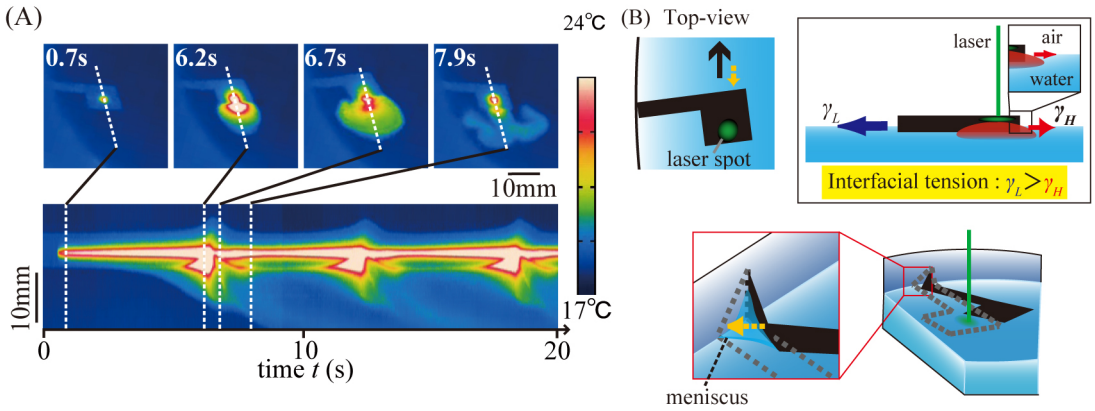


Figure 7.3 (A) Spatio-temporal diagram of the temperature profile for the rhythmic motion of the hammer-shaped object, together with snapshots of the spatial temperature profile. (B) Schematic representation of the difference in interfacial tension between the sides of the hammer-shaped plate under local heating by a laser. The black arrow shows the net force and the light-orange arrow is the restoring force due to the meniscus.

Using these two variables, we propose the following coupled differential equations.

$$\begin{cases} \frac{d^2\theta}{dt^2} = -\alpha\frac{d\theta}{dt} - b\theta + c\xi(\theta)\tau \\ \frac{d\tau}{dt} = d\xi(\theta) - e\tau \end{cases} \tag{7.1}$$

where $a, b, c, d$ and $e$ are positive constants that depend on the arrangement of the experimental system. The first term on the right side of the upper equation in Eq. (7.1) shows the effect of viscous damping, and the second term is the recovering force to maintain the meniscus between the hammer handle and the wall of the vessel due to interfacial tension, as shown schematically in Figure 7.3(B). The last term on the first line of Eq. (7.1) is the driving force caused by the difference in interfacial tension, as shown in Figure 7.3(B). The second differential equation in Eq. (7.1) describes the speed of the change in temperature around the hammer head caused by laser irradiation, where $\xi(\theta)$ is

$$\xi(\theta) = \begin{cases} 1 & 0 \leq \theta < k \\ e^{-\eta(\theta-k)^2} & \theta \geq k \end{cases} \tag{7.2}$$

$\xi(\theta)$ expresses the efficiency of heating due to laser irradiation as a function of $\theta$, $k$ in Eq. (7.2) is a parameter.

Figures 7.4(A) and (B) exemplify the results of numerical calculations based on Eqs. (7.1) and (7.1), where we adopted $a = 0.241,\ b = 0.398,\ c = 0.315,\ e = 1.1,\ k = 0.25$ and $\eta = 7500$. Where parameter a was determined from the decay of the angular velocity after sudden switch-off of the laser and parameter $b$ was set so as to fit the periodicity of the rhythmic motion. Parameter e was estimated from the rate of decrease of temperature toward room temperature after switch-off the laser under the condition that the hammer was spatially fixed. Parameter $\eta$ was chosen so as to roughly fit the temperature profile near the edge of hammer as observed by the thermal camera. After setting these parameters, parameter $c$ was chosen so as to reproduce the whole experimental trends in a similar manner. When the laser power is weak, i.e., when d in Eq. (7.1) is small ($d = 0.3$), the calculated results indicated a damping motion of the object, which leads to a stationary state. On the other hand, the object exhibits limit-cycle behavior when d is sufficiently large ($d = 0.45$). Figure 7.4(C) shows the amplitude of the oscillatory motion depending on d in Eq. (7.1). Thus, the calculated results reproduce the essential features of the observed photo-induced pendular motion.

### 7.3.3 Rotary motion under situational photoirradiation

Next, we show the experimental results for the motion of a hexagonal Al sheet floating on a droplet of oleic acid, as shown in Figure 7.5(A). A droplet of oleic acid (260 $\mu$L) was floated on an aqueous layer with a depth of ca. 5 mm in a container. Each side of the hexagonal Al sheet was 5 mm. Figure 7.5(B) shows the rotational motion of the Al sheet within the region of the oil droplet, under stationary laser irradiation with a power of 0.87 W. As shown in the lower part of Figure 7.5(B), the Al sheet causes fluctuation within the oil droplet up to an induction period of ca. 5 seconds. Thereafter, the Al sheet exhibited continuous rotational motion around the laser spot. Figure 7.5(C) shows the results of the simultaneous observation of rotational motion with both a digital video camera and a thermal-camera. The images show that there is a temperature difference between the front and rear of the hexagonal sheet as shown in the thermal images, with the corresponding position on the sheet

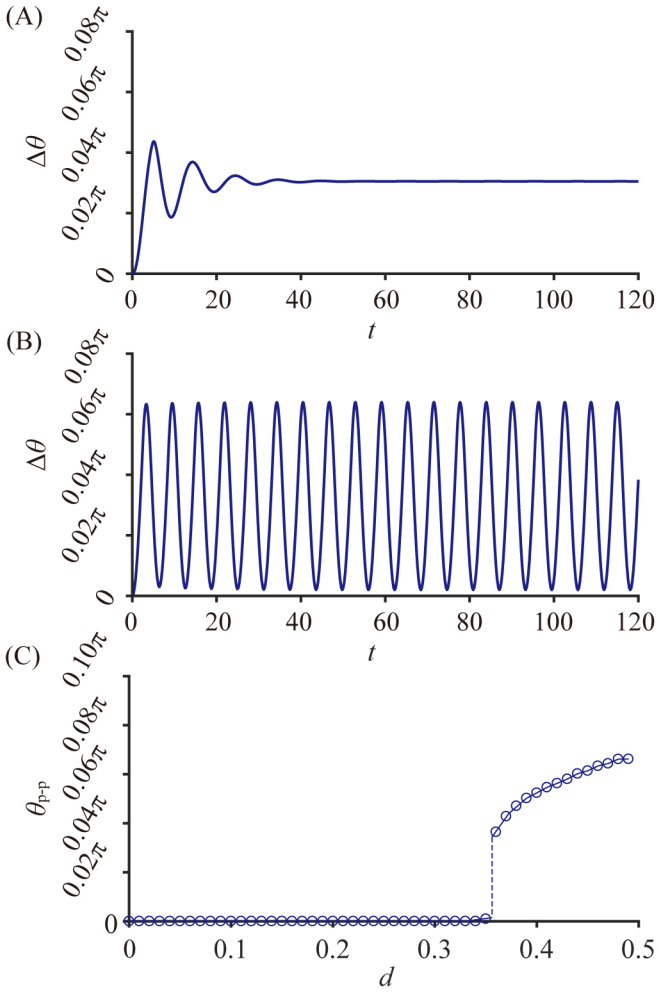


Figure 7.4 Results of the numerical simulation of pendular motion, by adapting the numerical equations (1) and (2). (A) Damping motion to a stationary state when the laser power is weak, $d = 0.3$. (B) Rhythmic motion with a greater laser power, $d = 0.45$. (C) Dependence of the amplitude of rhythmic motion on the heating parameter, d. As for the details on the parametrizations, see the text. $\Delta\theta$ and $\theta_{\text{p-p}}$ corresponds to those shown in Fig. 7.4 (A) and (B), respectively.

marked with a green X. During rotational motion, the front part moves toward the laser spot and exhibits a gradual temperature increase. As a result, the degree of heating at the rear becomes significant, which causes a higher temperature at the rear than at the front. As in the experiments on pendular motion, the air/water interfacial

tension at higher temperature becomes lower than that at lower temperature. Thus, during rotational motion, the hexagonal object continues to accept the driving force due to the difference in interfacial tension between the front and rear. Figure 7.5(D) shows the state of the hexagonal sheet depending on the laser power. Here again, similar to the pendular motion described above, the rotatory motion exhibits on/off switching depending on the laser power; i.e., the motion shows a subcritical-type transition. Based on the experimental results, we found that the direction of rotation of the object in the droplet is sensitive to the initial conditions; i.e., the direction of rotation is almost stochastic. To develop a method for controlling the mode of rotation in a reliable manner, we performed experiments using an Al sheet with chiral asymmetry, as shown in Figure 7.6, where the Al sheet has a propeller-like morphology with chiral asymmetry. Using this chiral object, we succeeded in constructing an experimental system that undergoes directional rotation. The upper panels show the generation of clockwise rotation and the bottom panels show anti-clockwise rotation.

## 7.4 Conlusion

It has become clear that, for a cm-sized metallic sheet floating on an aqueous solution, both stable pendular motion and rotary motion are generated under continuous photo-irradiation. The driving force is the spatial gradient of surface tension caused by photo-absorption on the metallic sheet. Interestingly, with a change in the color pattern on the sheet, rotational motion can become deterministic between clockwise and anticlockwise modes. It is expected that various regular motions besides simple pendular and rotational motion could be realized through the suitable choice of morphology and the color pattern.

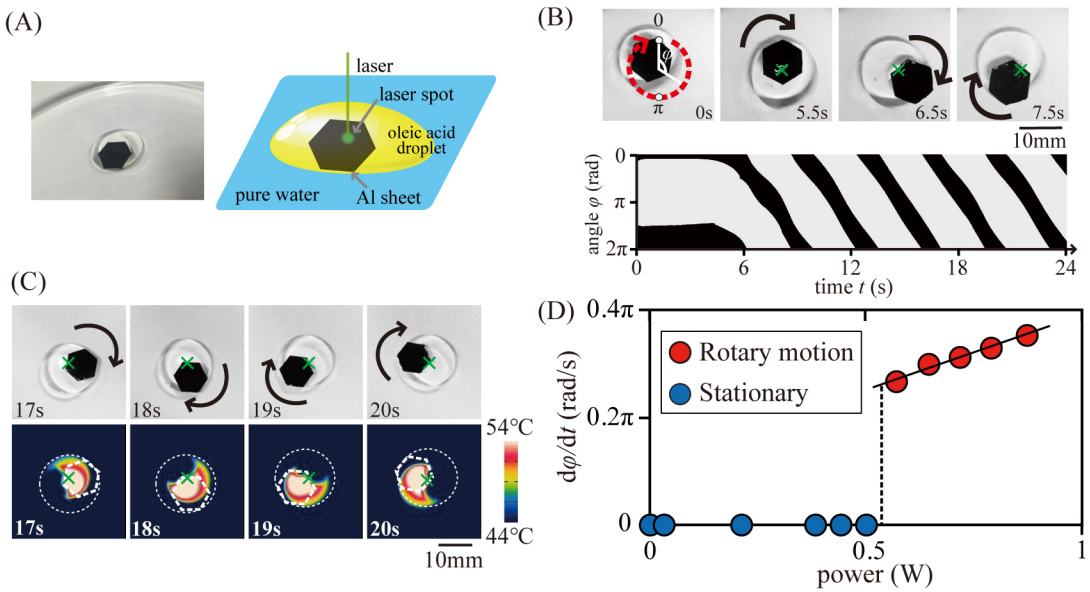


Figure 7.5 Rotary motion of a hexagonal Al sheet. (A) Photograph of the floating Al sheet entrapped inside an oil droplet (oleic acid, 260 $\mu$L) together with a schematic representation. (B) Example of rotary motion caused by CW laser irradiation and the corresponding spatio-temporal diagram. $\varphi$ is defined as shown in the snapshot for 0 sec. The direction of rotation is determined by the initial condition, i.e., the direction of rotation is bistable. (C) Snapshots of rotary motion and the corresponding temperature profiles. (D) Phase diagram of rotary motion dependent on the laser power.

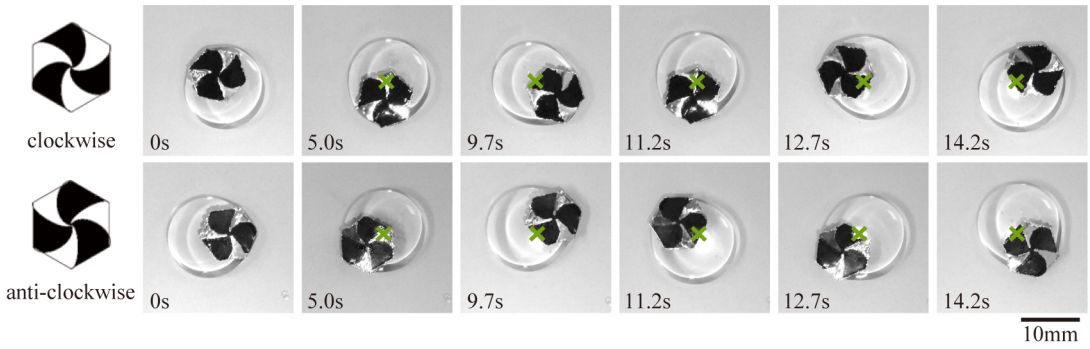


Figure 7.6 Clockwise and anti-clockwise rotary motions with chiral propeller-shaped objects. The rotational direction is deterministic depending on the chirality of the Al object.

# Chapter 8

# Optical fluid pump: generation of directional flow via microphase segregation/homogenization [v]

## 8.1 Introduction

In general, oil/water systems exist as either a homogeneous solution or a macroscopically segregated solution [70, 162, 163], which can be interpreted in terms of a first-order phase transition. The phase coexistence on a microscopic scale is intrinsically unstable in the absence of a surfactant under equilibricity. This implies the possible occurrence of dynamic phenomena, including the emergence and annihilation of microscopic segregation under thermodynamically open conditions. Recently, it has been shown that a focused laser can generate microscopic phase-separation in a homogeneous solution composed of oil and water under a condition that is near the critical point for a phase transition [164–174]. When the homogenous solution is enriched with oil near the bimodal line in the phase diagram, water-rich microdroplets successively emerge from the laser focus under constant laser irradiation [64,175–177]. The generated water-rich microdroplets tend to escape from the focus because of the lower dielectricity compared to that of the oil-rich medium. As they travel into the periphery, the microdroplets disappear by merging into the homogeneous bulk in the absence of a laser-induced dielectric potential. Here, it is expected that the emergence of several microdroplets at the laser focus will cause an increase in local pressure due

to a transient increase in the total oil/water interfacial area, which is incommensurate with molecular packing. In this article, we propose a new methodology for producing an optically driven micro-pump by applying such kind of dynamical phenomenon with the emergence/annihilation of microdroplets caused by a focused laser. There has been growing interest [178–181] in the subject of micro-pumps below the millimeter scale in the medical and micro-engineering fields, such as in the use of micro-pumps in biosensors, small fuel cells, and drug-delivery equipment. However, micro-pumps smaller than a micrometer scale do not seem to be available for practical application. Trials that involve the downsizing of existing pump have encounterd serious difficulties because of the relatively greater effects of viscosity and friction in a microscopic system. On the other hand, it is well known that laser trapping is a useful tool for transporting objects smaller than the scale of several tens of micrometers [134, 165, 179, 182, 183]. Several studies have shown that centimeter-sized objects at an interface can be transported by laser through a thermocapillary effect [135,184–187]. Thus, methods for transporting objects on a scale between several millimeters and several tens of micrometers are needed [163]. Recently, Wang, *et al.* reported that directional flow on the scale of several cm is generated by the use of a laser beam, through the photoacoustic effect [188]. The driving force is attributed to the generation of cavity caused by laser irradiation. Although this methodology seems to be interesting, we have to consider the possible effect of chemical damage induced by the breakage shock of the cavity [189].

## 8.2 Experimental system

In this study, we examined a mixture of water and trimethylamine (TEA), in which we previously observed the formation of a flower-like dynamic pattern with radial symmetry as a result of the generation and annihilation of microdroplets under continuous irradiation by a focused laser [168,169]. As shown in Fig. 8.1(a), an infrared laser (1064 nm Nd:YAG laser, Millennia IR, Spectra-Physics; output power 0.5 W) was passed through an oil-immersion objective lens (×100, numerical apparatus; 1.3) with an inverted microscope (Nikon ECLIPSE TE300). The photo intensity on the solution after passing through the objective lens was ca. 50 mW [171]. The images were recorded at a field of view of $45 \times 60$ $\mu$m$^2$ every 1/30 s using a high-sensitivity

monochromic digital video camera (Nikon WAT-120N). The temperature was set to 291 K to ensure that the solution was near criticalitys. For preparation of the sample solution, triethylamine (TEA) and pure water were mixed in a volume ratio of 1:1. After vigorous mixing, the solution was allowed to stand for more than one hour before the experiment. In Fig. 8.1(b), we have shown the visual images on the water and triethylamine solution, revealing the clear macroscopic phase separation when the solution has been standing still more than several hours. By shaking the solution or mechanical agitation, the solution becomes turbid for the period of several tens of seconds, indicating the occurrence of microphase segregation. For the experiment of laser irradiation in the chamber, we transferred a part of TEA-rich phase (upper layer) from the well-separated solution (the panel of before mixing, Fig. 8.1(b)) to thin glass chamber in a fully occupied state with tight shielding from outer environment (lateral view in Fig. 8.1(a)). In the present study, we have examined the effect of spatial asymmetry on dynamic flow pattern. By adapting a very simple method to introduce spatial asymmetry, we placed a glass plate near the laser focus, as indicated in Fig. 8.1(a) and top picture of Fig. 8.2.

## 8.3 Results and discussions

### 8.3.1 Emergence of directional flow under laser irradiation

Figure 8.2 shows the results of laser irradiation for a homogeneous solution that was allowed to equilibrate for more than one hour, and the spatio-temporal diagram after the start of laser irradiation. The snapshots on the bottom of Fig. 8.2 depict/illustrate the area around the laser focus at 0.2 s and 10 s together with the corresponding flow profiles. Under laser irradiation, microdroplets successively emerge at the focus, and the generated droplets escape into the surrounding solution. Then, the droplets tend to merge into the solution and disappear. The driving force of the escaping motion around the laser focus is attributable to the gradient of dielectric potential together with scattering force, i.e., lower dielectricity, or refractivity, of emerging droplets with richer water content caused the repulsive effect from the laser focus as described in previous studies [169, 170]. The outgoing flow generally becomes asymmetric and transforms to directional flow after a few seconds (the bottom pictures in Fig. 8.2).

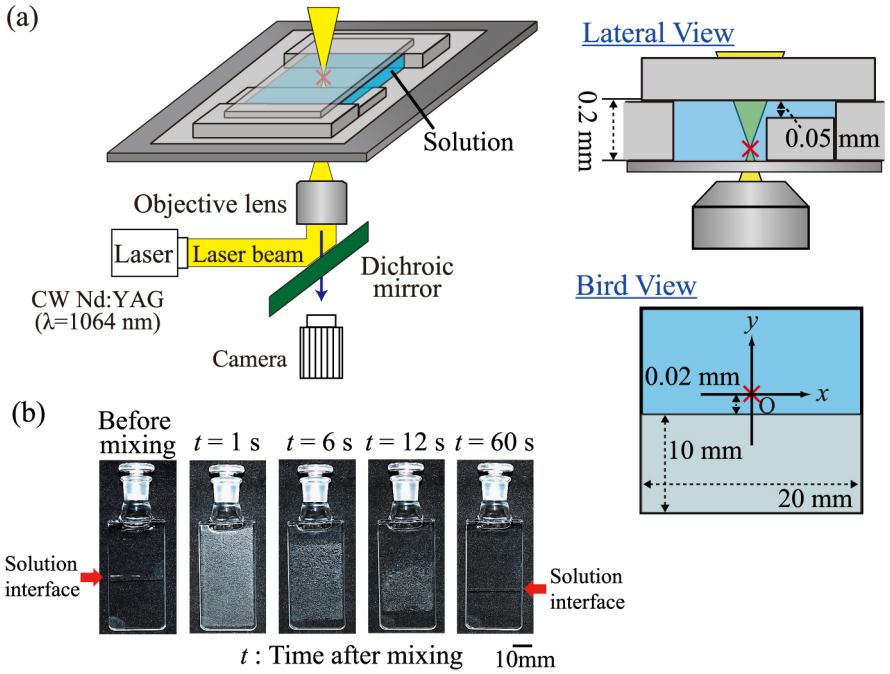


Figure 8.1 (a) Schematic illustration of the experimental setup. A Nd:YAG laser (1064 nm) was applied at a fixed power of 0.5 W. The laser light was passed through an oil-immersed objective lens with an inverted microscope, where the focus is denoted by a red "x". The chamber was fully filled with TEA-rich solution and shielded from the outer environment. To introduce spatial-asymmetry in the experimental system, a glass sheet with a width of 0.15 mm was situated on the right-hand side of the chamber. (b) Effect of mechanical agitation on the macroscopic phase-separated solution of water and TEA with a volume ratio of 1:1 at room temperature (291 K). Just after agitation, the solution becomes turbid and then tends to be transparent, accompanied by growth of the phase separation

The flow profiles are depicted in 2D, which were obtained through a Fourier image analysis. The time development of directional flow is found. The fluid velocity was evaluated based on an analysis of the saptio-temporal dynamics by ImageJ/Matlab. For the initial radial symmetric flow ($t$ = 0 s - 2 s), the velocity in the positive direction along the $y$ axis was 52 $\pm$ 7 $\mu$m/s for the region around 5 $\mu$m - 10 $\mu$m from the focus and that in the negative direction was 47 $\pm$ 14 $\mu$m/s. For $t$ = 2 s - 5 s, the velocity in the positive direction along the $y$ axis increased to ca. 100 $\mu$m/s, whereas that between the boundary and laser focus, i.e., the negative direction, were not so different (positive directional flow 105 $\pm$ 57 $\mu$m/s and negative directional flow 48 $\pm$

15 $\mu$m/s). Interestingly, the flow velocity in the positive direction increased to ca. 180 $\mu$m/s, for $t$ = 7 s - 8 s. Thus, we successfully constructed a micro-pump that increased the directed velocity of water droplets by more than three-fold compared to the initial radial symmetric flow. In the present study, directional flow is induced by the combination of the photo-induced dielectric potential caused by the focused laser [190] and the geometrical asymmetry of the environment/boundary condition around the laser focus. Based on the results of past experimental studies concerning the effect of laser irradiation on to the mixed solution near critical condition of phase separation, [64, 169, 171] it is expected that the dielectric potential caused by the focus laser is the main contributor to generate the micro phase separation. For the homogeneous mixture between water and TEA under geometrically symmetric condition, it has been confirmed that essentially the same dynamical pattern of the droplets is observed with either $H_2O$ and $D_2O$, or with a laser wavelength of either 800 nm and 1064 nm [176]. Here, it is noted that the absorption of $D_2O$ is less than 1/10 compared to $H_2O$ at 1064 nm, i.e., the heating effect is significantly different between $D_2O$ and $H_2O$, if one considers the microphase segregation as the main factor. It was also found that laser focusing on a micro droplet in a solution with lower critical solution temperature, LCST, causes disappearance or homogenization, i.e., the opposite effect against laser heating [64]. In relation to the possible temperature effect, it was reported that focused IR laser caused apparent increase of the temperature on the laser spot, where the irradiation was performed for a homogeneous solution under negligible convective flow [191]. Based on these considerations, we conclude that the relatively fast fluid flow caused by the continuous emergence of droplets is attributable mainly to dielectric effect by the focused laser.

### 8.3.2 Synchronous oscillatory motion of two droplets

Figure 8.2 shows spatio-temporal diagrams for droplet motion. As shown in Fig. 8.2(a1), the droplets undergo 1:1 swinging-type synchronization, where a narrow pipette ($\phi$ = 1.8 mm) was put at the middle of the waterway in the experiments as depicted in Fig. 8.1. When the intervening narrow pipette was replaced by the thick glass rod ($\phi$ = 5.0 mm), the droplets exhibit unsynchronized motion. It is noted that replacement of the interference barrier of the narrow pipette by the glass rod

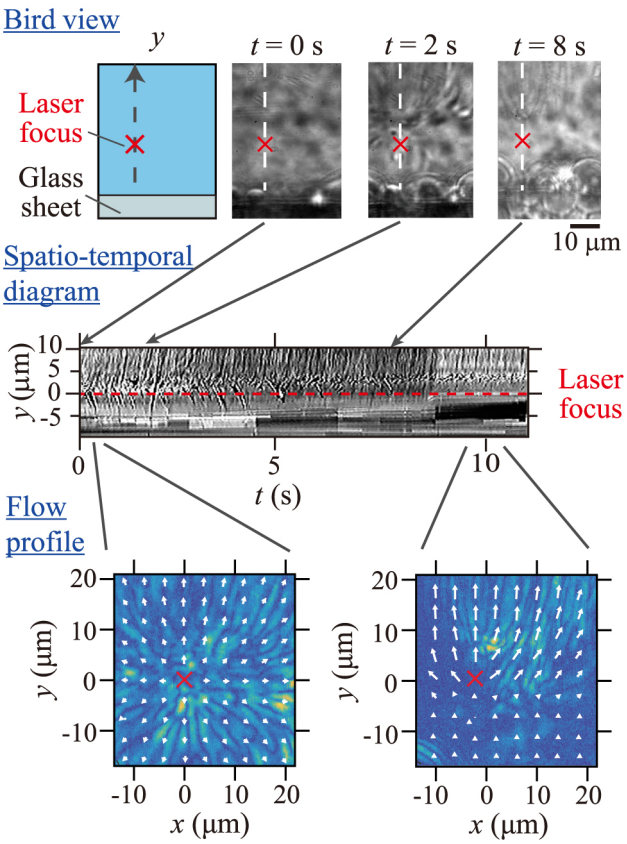


Figure 8.2 Spatio-temporal diagram for the water-TEA mixed solution (volume ratio, 1:1) from the start of laser irradiation, showing that microdroplets of water emerge continuously under situational laser irradiation. The images at the top show snapshots at $t = 0$ s, 2 s and 8 s. The emerging droplets tend to escape from the focus driven by the local increase in pressure near the region of droplet generation. The snapshots at the bottom exemplify flow patterns at different time-stages at 0.2 s and 10 s, which were obtained by 2D FFT analysis. The flow velocity arrow was determined from the slopes of spatio-temporal diagrams with different geometrical directions.

with wider diameter causes the coupling strength between the self-moving droplets to be weaker. The difference in the interference mode of coupled motion can be depicted as a phase diagram, as shown in the lower panels in Fig. 8.2. For 1:1 synchronized motion, the trajectory shows a regular loop along a straight line with a slope of unity (Fig. 8.2(a2)). Figure 8.2(c1) shows the spatio-temporal diagram when the intervening pipette was positioned on the right side of the waterway, revealing the appearance of 2:1 synchronization of back-and-forth motion. Recently, we have reported that the

up-down self-propelled motion for a floating oil droplet by prohibiting translational motion by use of thin glass rod [138]. It was found that a pair of neighboring droplets undergo in-phase synchronization. Such an experimental trend was argued in terms of the Marangoni effect under gravitational instability for a heavy oil droplet. The mode of the synchronization of the swinging-type motion in the present study is regarded to correspond to the in-phase synchronization on the up-down motion of two droplets.

### 8.3.3 Numerical simulation

To verify the experimental findings and pinpoint the essence of the underlying mechanisms, we examined the simple model shown in eq. (8.1):

$$\frac{\partial \vec{u}}{\partial t} + (\vec{u} \cdot \nabla)\vec{u} = -\nabla p + \frac{1}{R_e}\nabla^2 \vec{u} \tag{8.1}$$

where $\vec{u}$ is the velocity of the fluid, $p$ is the pressure, and $R_e$ is the Reynolds number. Here, we ignored the inertia term because of the low Reynolds number as mentioned below. To clarify the essential mechanism of directional flow in a simple manner, we reduce the dimentionality of the experimental system to two-dimensions by adapting the approximation that change in the effective Reynolds number for regions with different heights as in the lateral view in Fig. 8.1(a). Figure 8.3 exemplifies the numerical simulation with eq. (8.1) under two-dimensional approximation. We adopted Reynolds numbers, $R_e$, of $8 \times 10^{-3}$ for the bulk solution in the fluid field and $5 \times 10^{-4}$ for the local area, where the glass sheet was situated on the bottom of the glass chamber, as shown in the top view in Fig. 8.1(a). These values correspond to the experimental data determined from the observed viscosity of a water-triethylamine system [192]. We adapted a simple assumption that is the pressure at the laser focus linearly increase with reduced time from $\tau = 0$ to $\tau = 8$. The point with red "x" in Fig. 8.3(a) was chosen as the laser focus on the simulation array of 100 $\times$ 100 in reduced length. The time step in caliculations is set to $10^{-4}$ to ensure numerical stability, and the differential equation is solved by the cubic interpolated polynomial (CIP) method [193]. In Figs. 8.3(b) and (c) are shown two snapshots of the flow dynamics at $\tau = 0.2$ and $\tau = 8$, respectively, close to the proximal area around the laser spot. These numerical results reproduce the essential aspect of the observed

flow profiles in Fig. 8.2 regardless the very simple approximation. Initially, isotropic flow escaping from the laser spot is observed, which gradually evolves into strongly anisotropic directed flow away from the boundary, as indicated by the vector-field. Based on the experiments and calculated results, we can conclude that the spatial asymmetry of viscosity is essential for creating strongly directed flow.

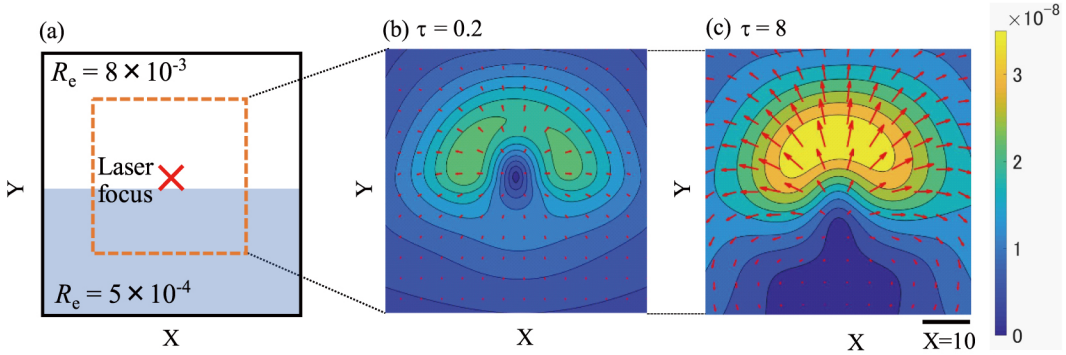


Figure 8.3 Numerical simulations on the flow pattern for a simplified 2D model. (a) The simulation was performed with a 2D square, $X = [-50, 50]$, $Y = [-50, 50]$, where the focus point is at $X = 0$, $Y = 5$, which are dimensionless values in calculations. To take into account the effect of geometrical asymmetry on depth, we adopted different Reynolds numbers, $R_e$, as indicated in the figure; $R_e = 8 \times 10^{-3}$ and $R_e = 5 \times 10^{-4}$ for the upper and lower parts in the calculation region, respectively. (b) Snapshot of the flow pattern at $\tau = 0.2$, and (c) Snapshot at $\tau = 8$. Region (a) in orange corresponds to a square area around the laser spot with a width of 60.

## 8.4 Conclusion

The present study has demonstrated the successful generation of directed flow by a continuous laser irradiation is achieved by introducing geometrical asymmetry in the experimental chamber. This self-establishing directional flow is regarded as a new type of light-driven micro-pump/motor, being difficult from the past studies [194–197]. The findings may also lead to the development of micro-sized pumps and motors that could not be engineered before on such a small scale. Further studies on the development of new optical pumps would be awaited to examine various liquidus system near criticality, that are composed with different kinds of chemical species, together with

the investigation toward more effective spatially asymmetric arrangements [198, 199].

# Chapter 9

# General conclusion

In summary of this study, it is aimed to unveil the essences of the mechanism about the formation of structure and the control of the function by using real-world experimental model. In other words, simplified cellular models utilizing the biomolecules extracted from the living cell and the artificial models of motility of living organisms composed by the abiotic origin molecules have been indicated to clarify the essential mechanism of the autonomous appearance of cell-like structure or dynamic motility of living organisms.

## 9.1 Spontaneous formation of cell-like structure under crowding condition of macromolecules

It is known the inside living cell is highly crowded condition of biomolecules. It is considered that the living system utilize such highly concentrated environment and form their structure. Biomacromolecules such as DNA, RNA and multifarious proteins compose the cellular cytoplasm and nucleus. It is suggested the specific physico-chemical properties of macromolecules or crowding environment by themselves play the important role for the assembly of structures and control of functions. Here, it has been shown the artificial cellular model considering those properties of macromolecules. A simple binary polymer system with polyethylene glycol (PEG) and dextran (DEX) was used. Under the certain concentrations two polymers in the solution, cell-sized water/water microdroplets with diameters ranging from 10 to 100 $\mu$m, emerged. And such solution can entrap the biomolecules nucleic acids and pro-

teins and so on, in the either phase. In this study, these droplets considered the model of cellular confinement and confirmed the characteristic behavior of biomolecules or cells.

In Chapter 2, it has been shown the spontaneous emergence of cell-like structure by mixing phospholipids which compose the cellular membrane and DNA, biomacromolecule, for the PEG/DEX binary solution system. Our previous study has revealed that when double-stranded DNA and cytoskeletal actin filament, the both are biological components essential for living cell, are added to LLPS caused in the two-component system of PEG and DEX, they are selectively accumulated in the DEX phase. Here, it has been revealed the phospholipids are accumulated to the interface of droplets rich in DEX by mixing binary solution of PEG/DEX, spontaneously. That is, microdroplets occurring through microphase separation can have plausible potential to work as a template to confirm the surface for membrane formation including entrapment of biomacromolecules in real cells.

In Chapter 3, it is indicated the availability of artificial construction of a three-dimensional cell assembly utilizing microdroplets emerging with the binary polymer solution of PEG/DEX. It has been found erythrocytes (horse red blood cells; RBCs) and NAMRU mouse mammary gland epithelial cells (NMuMG cells) were completely and spontaneously entrapped inside DEX-rich microdroplets. And cells were located in the interior and at the periphery of the droplets depending on the species of cell and the composition of polymer concentration. The simple mixing procedure with micro water/water droplets may provide novel methodology to construct 3D cellular assembly composed with difference cell species.

It has been described the spontaneous emergence of cell-like structure or cellular assembly by using cell-sized droplets under the certain concentrations two polymers. It is suggested these formations of structure are accomplished with the effect of entropy. Mixing entropy, translational entropy of each molecules play the important role to create the cells and organs structure. Through the model system, it has become clear the significant process and mechanism of self-organization of cell-like structure.

## 9.2 Self-emergence of dynamic motility with the collective motion of molecules

In this study, it has been focused the essential function of living system, the emergence and control of motility of living organisms. In living organisms, the motor protein of actin-myosin, microtubule-kinesin or -dynein is revealed in recent years. In addition, it is reported that the self-propelled motion of the objects in the solution or on the surface of solution including oil droplet, camphor boat, particle and so on. Here, it has been shown the artificial model indicating dynamic motility caused through non-equlibrium molecular system. They are including not only the model using biomolecules extracted from the living organisms, also composed by the abiotic origin molecules.

In Chapter 4, the reconstructed model with kinesin-microtubule has been indicated. Kinesin of motor protein and microtubule of rail filamentous protein are entrapped into the DEX-rich droplets, by mixing for PEG/DEX binary solution. In the droplet, kinesin and microtubule indicated the collective convectional flow. The morphology of flow depends on the size of confinement. It is considered this is caused by the alignment of each microtubule in the confinement. And these convectional flow are able to contribute to the motile of droplets including kinesin-microtubule. Also it is expected as the model to clarify the mechanism of the protoplasmic flow.

In Chapter 5, it has been shown the chemotactic behavior of an oil droplet floating on aqueous phase. That is, the repulsive/attractive motion of an oil droplet caused by the application of a stimulant gas. Centimeter-sized droplet of oleic acid is repelled by ammonia vapor. In contrast, a droplet of aniline on an aqueous phase moves toward hydrochloric acid as a stimulant. The mechanisms of these characteristic behaviors of oil droplets are discussed in terms of the spatial gradient of the interfacial tension caused by the acid-base reaction between the droplet molecules and stimulant gas molecules. This is expected not only the model of chemotaxis of living system, also one of manipulation using chemical reaction as human technology.

In Chapter 6, synchronized motion between self-running droplets floating on aqueous solution. The two droplets exhibit a swinging synchronization when a thin glass

capillary is placed at the midpoint of the waterway with a narrow rectangle shape. Furthermore, 2:1 synchronized oscillation of the periodicities of this back-and-forth motion is generated when the capillary is shifted away from the center of the waterway. These studies are expected to contribute to the development of a system that exhibits self-organized motion working driven by chemical non-equilibrium under isothermal condition.

In Chapter 7, it was expanded to the collective motion of metallic sheet under stationary photoirradiation by a laser. Local heating by laser irradiation can cause the spatial gradient of interfacial tension, and metallic sheet which absorbed photon can generate the motility. Here, by fixing the shape of metallic sheet and boundary condition, the rhythmic pendular motion and stable rotary motion can be obtained. It has become clear that various regular motions besides simple pendular and rotational motion could be realized through the suitable choice of morphology.

In Chapter 8, the availability of directional flow has been indicated by geometrical symmetry breaking. When geometrical asymmetry is introduced around the laser focus in the chamber, continuous directional flow is generated, accompanied by the emergence of water-rich microdroplets at the laser focus by irradiating for the homogeneous solution. When geometrical asymmetry is introduced around the laser focus in the chamber, continuous directional flow is generated, accompanied by the emergence of water-rich microdroplets at the laser focus.

It has been described the spatial asymmetry caused by the boundary condition or interior or exterior factor create the collective motion through these studies. And under dynamic motile, the interaction between each droplets or objects generate synchronous motion. It is expected to clarify the essential mechanism of collective motion of living organisms by using artificial model. Also, it will can be developed the novel technique for the driving and manipulating objects.

# References


[1] S. B. Zimmerman and A. P. Minton, *Annual review of Biophysics and Biomolecular Structure* **22**, 27 (1993).

[2] R. J. Ellis, *Current Opinion in Structural Biology* **11**, 114 (2001).

[3] F. Crick, *Nature* **227**, 561 (1970).

[4] B. Alberts, A. D. Johnson, J. Lewis, D. Morgan, M. Raff, K. Roberts, and P. Walter, *Molecular Biology of the Cell: Sixth International Student Edition*, Garland Science, Taylor and Francis Group, 2014.

[5] R. Milo, *BioEssays* **35**, 1050 (2013).

[6] N. A. Kulak, G. Pichler, I. Paron, N. Nagaraj, and M. Mann, *Nature Methods* **11**, 319 (2014).

[7] F. Oosawa, *Journal of Polymer Science* **23**, 421 (1957).

[8] F. Oosawa, *Biopolymers* **6**, 1633 (1968).

[9] G. S. Manning, *Quarterly Reviews of Biophysics* **11**, 179 (1978).

[10] P. G. de Gennes, 和訳: 久保 亮五, 高野 宏, 中西 秀,『**高分子の物理学: スケーリングを中心にして**』, 吉岡書店, 1984.

[11] A. A. Hyman, C. A. Weber, and F. Jülicher, *Annual review of cell and developmental biology* **30**, 39 (2014).

[12] P.-Å. Albertsson, *Partition of Cell Particles and Macromolecules*, Wiley: New York, New York, 2nd edition, 1971.

[13] 作田 浩輝, 馬籠 信之, 吉川 研一,**「ナノの世界からマクロな世界を動かす: 見えない分子から巨視的な動きへ」『分子マシンの科学分子の動きとその機能を見る』**, 26 巻 *CSJ* **カレントレビュー**, 化学同人, 日本, 2017.

[14] R. P. Feynman, *The Feynman Lectures on Physics*, Reading, Mass. : Addison-Wesley Pub. Co., c1963-1965., 1963.

[15] R. D. Vale, T. Funatsu, D. W. Pierce, L. Romberg, Y. Harada, and T. Yanagida, *Nature* **380**, 451 (1996).

[16] R. D. Vale, *Cell* **112**, 467 (2003).

[17] A. F. Huxley, R. M. Simmons, K. Kinosita, R. Yasuda, H. Noji, and K. Adachi, *Philosophical Transactions B* **355**, 473 (2000).

[18] K. Takiguchi, A. Yamada, M. Negishi, Y. Tanaka-Takiguchi, and K. Yoshikawa, *Langmuir* **24**, 11323 (2008).

[19] Y. Sumino, K. H. Nagai, Y. Shitaka, D. Tanaka, K. Yoshikawa, H. Chate, and K. Oiwa, *Nature* **483**, 448 (2012).

[20] K. Yoshikawa and N. Magome, *Bulletin of the Chemical Society of Japan* **66**, 3352 (1993).

[21] N. Magome and K. Yoshikawa, *Journal of Physical Chemistry* **100**, 19102 (1996).

[22] K. Nagai, Y. Sumino, H. Kitahata, and K. Yoshikawa, *Physical Review E* **71**, 065301/1 (2005).

[23] Y. Sumino, N. Magome, T. Hamada, and K. Yoshikawa, *Physical Review Letters* **94**, 068301/1 (2005).

[24] T. Toyota, N. Maru, M. M. Hanczyc, T. Ikegami, and T. Sugawara, *Journal of the American Chemical Society* **131**, 5012 (2009).

[25] S. Ramaswamy, *Annual Review of Condensed Matter Physics* **1**, 323 (2010).

[26] T. Ban, T. Yamagami, H. Nakata, and Y. Okano, *Langmuir* **29**, 2554 (2013).

[27] D. Yamamoto, A. Mukai, N. Okita, K. Yoshikawa, and A. Shioi, *Journal of Chemical Physics* **139**, 034705 (2013).

[28] N. J. Cira, A. Benusiglio, and M. Prakash, *Nature* **519**, 446 (2015).

[29] S. Nakata, R. Tenno, A. Deguchi, H. Yamamoto, Y. Hiraga, and S. Izumi, *Colloids and Surfaces A* **466**, 40 (2015).

[30] E. M. Courchaine, A. Lu, and K. M. Neugebauer, *EMBO journal* , e201593517 (2016).

[31] O. Akbulut, C. R. Mace, R. V. Martinez, A. A. Kumar, Z. Nie, M. R. Patton, and G. M. Whitesides, *Nano Letters* **12**, 4060 (2012).

[32] A. A. Kumar, C. Lim, Y. Moreno, C. R. Mace, A. Syed, D. Van Tyne, D. F. Wirth, M. T. Duraisingh, and G. M. Whitesides, *American Journal of Hematology* **90**, 31 (2015).

[33] C. R. Mace, O. Akbulut, A. A. Kumar, N. D. Shapiro, R. Derda, M. R. Patton, and G. M. Whitesides, *Journal of the American Chemical Society* **134**, 9094 (2012).

[34] V. N. Uversky, *Current Opinion in Structural Biology* **44**, 18 (2017).

[35] H. Walter and D. E. Brooks, *FEBS Letters* **361**, 135 (1995).

[36] B. Y. Zaslavsky, L. A. Ferreira, A. L. Darling, and V. N. Uversky, *International Journal of Biological Macromolecules* **117**, 1224 (2018).

[37] C. P. Brangwynne, *The Journal of Cell Biology* **203**, 875 (2013).

[38] G. Rivas and A. P. Minton, *Trends in Biochemical Sciences* **41**, 970 (2016).

[39] J. Spitzer and B. Poolman, *FEBS Letters* **587**, 2094 (2013).

[40] C. D. Crowe and C. D. Keating, *Interface Focus* **8** (2018).

[41] B. Monterroso, S. Zorrilla, M. Sobrinos-Sanguino, C. D. Keating, and G. Rivas, *Scientific Reports* **6**, 35140 (2016).

[42] S. F. Banani, H. O. Lee, A. A. Hyman, and M. K. Rosen, *Nature Reviews Molecular Cell Biology* **18**, 285 (2017).

[43] J. Esquena, *Current Opinion in Colloid & Interface Science* **25**, 109 (2016).

[44] S. Singh and H. Tavana, *Frontiers in Chemistry* **6** (2018).

[45] N. Nakatani, H. Sakuta, M. Hayashi, S. Tanaka, K. Takiguchi, K. Tsumoto, and K. Yoshikawa, *ChemBioChem* **19**, 1370 (2018).

[46] K. Tsumoto, M. Arai, N. Nakatani, S. Watanabe, and K. Yoshikawa, *Life* **5**, 459 (2015).

[47] Y. Yoshikawa, T. Kanbe, and K. Yoshikawa, *Chemical Physics Letters* **366**, 305 (2002).

[48] M. Hishida, H. Seto, N. L. Yamada, and K. Yoshikawa, *Chemical Physics Letters* **455**, 297 (2008).

[49] H. Hotani, F. Nomura, and Y. Suzuki, *Current Opinion in Colloid & Interface Science* **4**, 358 (1999).

[50] F. Nomura, M. Nagata, T. Inaba, H. Hiramatsu, H. Hotani, and K. Takiguchi, *Proceedings of the National Academy of Sciences of the United States of America* **98**, 2340 (2001).

[51] H. Sakuta, T. Fujimoto, Y. Yamana, Y. Hoda, K. Tsumoto, and K. Yoshikawa, *Frontiers in Chemistry* **7**, 44/1 (2019).

[52] M. Ohno, T. Hamada, K. Takiguchi, and M. Homma, *Langmuir* **25**, 11680

(2009).

[53] M. W. Hetzer, *Cold Spring Harbor Perspectives in Biology* **2** (2010).

[54] M. Hayashi-Nishino, N. Fujita, T. Noda, A. Yamaguchi, T. Yoshimori, and A. Yamamoto, *Nature Cell Biology* **11**, 1433 (2009).

[55] M. Hamasaki, N. Furuta, A. Matsuda, A. Nezu, A. Yamamoto, N. Fujita, H. Oomori, T. Noda, T. Haraguchi, Y. Hiraoka, A. Amano, and T. Yoshimori, *Nature* **495**, 389 (2013).

[56] W. M. Aumiller and C. D. Keating, *Advances in colloid and interface science* **239**, 75 (2017).

[57] M. M. Hanczyc, S. M. Fujikawa, and J. W. Szostak, *Science* **302**, 618 (2003).

[58] T. Z. Jia, C. Hentrich, and J. W. Szostak, *Origins of Life and Evolution of Biospheres* **44**, 1 (2014).

[59] M. Vis, J. Opdam, I. S. J. Van't Oor, G. Soligno, R. Van Roij, R. H. Tromp, and B. H. Erné, *ACS Macro Letters* **4**, 965 (2015).

[60] T. J. Nott, T. D. Craggs, and A. J. Baldwin, *Natature Chemistry* **8**, 569 (2016).

[61] R. R. Poudyal, F. Pir Cakmak, C. D. Keating, and P. C. Bevilacqua, *Biochemistry* **57**, 2509 (2018).

[62] Y. Song, T. C. T. Michaels, Q. Ma, Z. Liu, H. Yuan, S. Takayama, T. P. J. Knowles, and H. C. Shum, *Nature Communicates* **9**, 2110 (2018).

[63] K. Tsumoto and K. Yoshikawa, *MRS Advances* **2**, 2407 (2017).

[64] H. Toyama, K. Yoshikawa, and H. Kitahata, *Physical Review E* **78**, 060801 (2008).

[65] C. Han, S. Takayama, and J. Park, *Scientific Reports* **5**, 11891 (2015).

[66] A. Yoshida, S. Tsuji, H. Taniguchi, T. Kenmotsu, K. Sadakane, and K. Yoshikawa, *Polymers* **9** (2017).

[67] E. Atefi, R. Joshi, J. Mann, J. A., and H. Tavana, *ACS Appl Mater Interfaces* **7**, 21305 (2015).

[68] L. Yu, J. Li, J. Hong, Y. Takashima, N. Fujimoto, M. Nakajima, A. Yamamoto, X. Dong, Y. Dang, Y. Hou, W. Yang, I. Minami, K. Okita, M. Tanaka, C. Luo, F. Tang, Y. Chen, C. Tang, H. Kotera, and L. Liu, *Stem Cell Reports* **11**, 142 (2018).

[69] A. Yamada, R. Renault, A. Chikina, B. Venzac, I. Pereiro, S. Coscoy, M. Verhulsel, M. C. Parrini, C. Villard, J. L. Viovy, and S. Descroix, *Laboratory on a*

*Chip* **16**, 4691 (2016).

[70] F. Huber, J. Schnau$\beta$, S. Rönicke, P. Rauch, K. Müller, C. Fübctterer, and J. Käs, *Advances in Physics* **62**, 1 (2013).

[71] E. Karsenti, *Nature Reviews Molecular Cell Biology* **9**, 255 (2008).

[72] H. De Forges, A. Bouissou, and F. Perez, *The International Journal of Biochemistry & Cell Biology* **44**, 266 (2012).

[73] T. D. Pollard and J. A. Cooper, *Science* **326**, 1208 (2009).

[74] T. Butt, T. Mufti, A. Humayun, P. B. Rosenthal, S. Khan, S. Khan, and J. E. Molloy, *Journal of Biological Chemistry* **285**, 4964 (2010).

[75] V. Schaller, C. Weber, C. Semmrich, E. Frey, and A. R. Bausch, *Nature* **467**, 73 (2010).

[76] A. C. Callan-Jones and F. Jülicher, *New Journal of Physics* **13**, 093027 (2011).

[77] J. F. Joanny and J. Prost, *HFSP Journal* **3**, 94 (2009).

[78] T. Torisawa, D. Taniguchi, S. Ishihara, and K. Oiwa, *Biophysical Journal* **111**, 373 (2016).

[79] A. Opathalage, M. M. Norton, M. P. N. Juniper, B. Langeslay, S. A. Aghvami, S. Fraden, and Z. Dogic, *Proceedings of the National Academy of Sciences of the United States of America* **116**, 4788 (2019).

[80] T. Sanchez, D. T. Chen, S. J. Decamp, M. Heymann, and Z. Dogic, *Nature* **491**, 431 (2012).

[81] Y. Sato, Y. Hiratsuka, I. Kawamata, S. Murata, and S. M. Nomura, *Science Robotics* **2** (2017).

[82] N. Biswas, M. Ichikawa, A. Datta, Y. T. Sato, M. Yanagisawa, and K. Yoshikawa, *Chemical Physics Letters* **539-540**, 157 (2012).

[83] W. Thielicke and E. J. Stamhuis, *Journal of Open Research Software* **2** (2014).

[84] T. Ban and H. Nakata, *The Journal of Physical Chemistry B* **119**, 7100 (2015).

[85] H. Linke, B. J. Alem1án, L. D. Melling, M. J. Taormina, M. J. Francis, C. C. Dow-Hygelund, V. Narayanan, R. P. Taylor, and A. Stout, *Physical Review Letters* **96**, 154502 (2006).

[86] L. Martiradonna, *Nature Materials* **14**, 463 (2015).

[87] M. Schmitt and H. Stark, *Physics of Fluids* **28**, 012106 (2016).

[88] F. C. Wang, F. Yang, and Y. P. Zhao, *Applied Physics Letters* **98**, 053112 (2011).

[89] K. Zhang, F. Liu, A. J. Williams, X. Qu, J. J. Feng, and C.-H. Chen, *Physical Review Letters* **115**, 074502 (2015).

[90] J. Zhang, Y. Yao, L. Sheng, and J. Liu, *Advanced Materials* **27**, 2648 (2015).

[91] H. J. Keh and J. S. Jan, *Journal of Colloid Interface Science* **183**, 458 (1996).

[92] J. Palacci, B. Abecassis, C. Cottin-Bizonne, C. Ybert, and L. Bocquet, *Physical Review Letters* **104**, 138302 (2010).

[93] M. Dupeyrat and E. Nakache, *Bioelectrochemistry and Bioenergetics* **5**, 134 (1978).

[94] S. Kai, S. C. Muller, T. Mori, and M. Miki, *Physica D* **50**, 412 (1991).

[95] S. Kai, E. Ooishi, and M. Imasaki, *Journal of the Physical Society of Japan* **54**, 1274 (1985).

[96] E. Nakache, M. Dupeyrat, and M. Vignes-Adler, *Journal of Colloid and Interface Science* **94**, 187 (1983).

[97] S. Nakata, T. Kaori, and H. Yuko, *Forma* **13**, 387 (1998).

[98] K. Yoshikawa and Y. Matsubara, *Journal of the American Chemical Society* **106**, 4423 (1984).

[99] A. Shioi, K. Katano, and Y. Onodera, *Journal of Colloid and Interface Science* **266**, 415 (2003).

[100] Y. Sumino, H. Kitahata, K. Yoshikawa, M. Nagayama, S. M. Nomura, N. Magome, and Y. Mori, *Physical Review E* **72**, 041603 (2005).

[101] M. M. Hanczyc, T. Toyota, T. Ikegami, N. Packard, and T. Sugawara, *Journal of the American Chemical Society* **129**, 9386 (2007).

[102] Q. Yuan, X. Huang, and Y.-P. Zhao, *Physics of Fluids* **26**, 092104 (2014).

[103] C. Bechinger, R. Di Leonardo, H. Löwen, C. Reichhardt, G. Volpe, and G. Volpe, *Reviews of Modern Physics* **88**, 045006/1 (2016).

[104] B. Esteban-Fernandez De Avila, W. Gao, E. Karshalev, L. Zhang, and J. Wang, *Accounts of Chemical Research* **51**, 1901 (2018).

[105] C. C. Maass, C. Krüger, S. Herminghaus, and C. Bahr, *Annual Review of Condensed Matter Physics* **7**, 171 (2016).

[106] N. J. Suematsu and S. Nakata, *Chemistry* **24**, 6308 (2018).

[107] T. Debnath, Y. Li, P. K. Ghosh, and F. Marchesoni, *Journal of Chemical Physics* **150**, 104102/1 (2019).

[108] S. Nakata, M. Nomura, H. Yamamoto, S. Izumi, N. J. Suematsu, Y. Ikura, and

T. Amemiya, *Angewandte Chemie International Edition* **56**, 861 (2017).

[109] T. Xu, F. Soto, W. Gao, R. Dong, V. Garcia-Gradilla, E. Magana, X. Zhang, and J. Wang, *Journal of the American Chemical Society* **137**, 2163 (2015).

[110] D. Yamamoto, T. Takada, M. Tachibana, Y. Iijima, A. Shioi, and K. Yoshikawa, *Nanoscale* **7**, 13186 (2015).

[111] C. Antoine and V. Pimienta, *Langmuir* **29**, 14935 (2013).

[112] T. Banno, A. Asami, N. Ueno, H. Kitahata, Y. Koyano, K. Asakura, and T. Toyota, *Scientific Reports* **6**, 31292/1 (2016).

[113] J. Čejková, M. Novák, F. Štěpánek, and M. M. Hanczyc, *Langmuir* **30**, 11937 (2014).

[114] Y. J. Chen, Y. Nagamine, and K. Yoshikawa, *Physical Review E* **80**, 016303/1 (2009).

[115] N. Horibe, M. M. Hanczyc, and T. Ikegami, *Entropy* **13**, 709 (2011).

[116] Z. Izri, M. N. Van Der Linden, S. Michelin, and O. Dauchot, *Physical Review Letters* **113**, 248302/1 (2014).

[117] J. Jiang, J. Gao, H. Zhang, W. He, J. Zhang, D. Daniel, and X. Yao, *Proceedings of the National Academy of Sciences of the United States of America* **116**, 2482 (2019).

[118] C. Jin, C. Krüger, and C. C. Maass, *Proceedings of the National Academy of Sciences of the United States of America* **114**, 5089 (2017).

[119] H. Kim, K. Muller, O. Shardt, S. Afkhami, and H. A. Stone, *Nature Physics* **13**, 1105 (2017).

[120] T. Liu, N. Nadermann, Z. He, S. H. Strogatz, C. Y. Hui, and A. Jagota, *Langmuir* **33**, 4942 (2017).

[121] V. Pimienta, M. Brost, N. Kovalchuk, S. Bresch, and O. Steinbock, *Angew Chem Int Ed Engl* **50**, 10728 (2011).

[122] Y. Satoh, Y. Sogabe, K. Kayahara, S. Tanaka, M. Nagayama, and S. Nakata, *Soft Matter* **13**, 3422 (2017).

[123] F. Takabatake, N. Magome, M. Ichikawa, and K. Yoshikawa, *The Journal of Chemical Physics* **134**, 114704/1 (2011).

[124] S. Tanaka, S. Nakata, and T. Kano, *Journal of the Physical Society of Japan* **86**, 101004/1 (2017).

[125] S. Tanaka, Y. Sogabe, and S. Nakata, *Physical Review E* **91**, 032406/1 (2015).

[126] N. Ueno, T. Banno, A. Asami, Y. Kazayama, Y. Morimoto, T. Osaki, S. Takeuchi, H. Kitahata, and T. Toyota, *Langmuir* **33**, 5393 (2017).

[127] D. Zwicker, R. Seyboldt, C. A. Weber, A. A. Hyman, and F. Jülicher, *Nature Physics* **13**, 408 (2017).

[128] E. F. Greco and R. O. Grigoriev, *Physics of Fluids* **21**, 042105/1 (2009).

[129] A. Karbalaei, R. Kumar, and H. J. Cho, *Micromachines* **7**, 13/1 (2016).

[130] M. Robert De Saint Vincent and J. P. Delville, *Physical Review E* **85**, 026310/1 (2012).

[131] Y. Zhao, F. Liu, and C.-H. Chen, *Applied Physics Letters* **99**, 104101/1 (2011).

[132] A. J. Bae, D. Hanstorp, and K. Chang, *Physical Review Letters* **122**, 043902/1 (2019).

[133] S. Rybalko, N. Magome, and K. Yoshikawa, *Physical Review E* **70**, 046301/1 (2004).

[134] C. Song, J. K. Moon, K. Lee, K. Kim, and H. K. Pak, *Soft Matter* **10**, 2679 (2014).

[135] F. Takabatake, K. Yoshikawa, and M. Ichikawa, *Journal of Chemical Physics* **141**, 051103/1 (2014).

[136] J. Arbelaiz, A. U. Oza, and J. W. M. Bush, *Physical Review Fluids* **3**, 013604/1 (2018).

[137] M. Hase, S. N. Watanabe, and K. Yoshikawa, *Physical Review E* **74**, 046301/1 (2006).

[138] Y. J. Chen, K. Sadakane, H. Sakuta, C. Yao, and K. Yoshikawa, *Langmuir* **33**, 12362 (2017).

[139] F. Jülicher, K. Kruse, J. Prost, and J. Joanny, *Physics Reports* **449**, 3 (2007).

[140] M. C. Marchetti, J. F. Joanny, S. Ramaswamy, T. B. Liverpool, J. Prost, M. Rao, and R. A. Simha, *Reviews of Modern Physics* **85**, 1143 (2013).

[141] S. Nakata, Y. Iguchi, S. Ose, M. Kuboyama, T. Ishii, and K. Yoshikawa, *Langmuir* **13**, 4454 (1997).

[142] K. Chen, C. Gu, Z. Yang, M. Nakajima, T. Chen, and T. Fukuda, *Micromachines* **8**, 183 (2017).

[143] J. Elgeti and G. Gompper, *The European Physical Journal Special Topics* **225**, 2333 (2016).

[144] F. Kümmel, B. Ten Hagen, R. Wittkowski, I. Buttinoni, R. Eichhorn, G. Volpe,

H. Löwen, and C. Bechinger, *Physical Review Letters* **110**, 198302 (2013).

[145] H. Ke, S. Ye, R. L. Carroll, and K. Showalter, *The Journal of Physical Chemistry A* **114**, 5462 (2010).

[146] G. Loget and A. Kuhn, *Nature Communication* **2**, 535 (2011).

[147] B. Dai, J. Wang, Z. Xiong, X. Zhan, W. Dai, C. C. Li, S. P. Feng, and J. Tang, *Nature Nanotechnology* **11**, 1087 (2016).

[148] D. Feldmann, S. R. Maduar, M. Santer, N. Lomadze, O. I. Vinogradova, and S. Santer, *Scientific Reports* **6**, 36443 (2016).

[149] Z. Shen, L. Su, X. C. Yuan, and Y. C. Shen, *Applied Physics Letters* **109**, 241901 (2016).

[150] L. Zhang, J. J. Abbott, L. Dong, K. E. Peyer, B. E. Kratochvil, H. Zhang, C. Bergeles, and B. J. Nelson, *Nano Letters* **9**, 3663 (2009).

[151] M. Ichikawa, F. Takabatake, K. Miura, T. Iwaki, N. Magome, and K. Yoshikawa, *Physical Review E* **88**, 012403 (2013).

[152] E. Lauga and A. M. J. Davis, *Journal of Fluid Mechanics* **705**, 120 (2011).

[153] F. Takabatake, K. Yoshikawa, and M. Ichikawa, *Journal of Chemical Physics* **141**, 051103 (2014).

[154] F. D. Dos Santos and T. Ondarcuhu, *Physical Review Letters* **75**, 2972 (1995).

[155] D. Jean-Pierre, V. Matthieu Robert De Saint, D. S. Robert, C. Hamza, I. Bruno, W. Régis, L. Didier, W. Z. Wendy, and B. Etienne, *Journal of Optics A* **11**, 034015 (2009).

[156] Y. Koyano, M. Gryciuk, P. Skrobanska, M. Malecki, Y. Sumino, H. Kitahata, and J. Gorecki, *Physical Review E* **96**, 012609 (2017).

[157] K. H. Nagai, K. Tachibana, Y. Tobe, M. Kazama, H. Kitahata, S. Omata, and M. Nagayama, *Journal of Chemical Physics* **144**, 114707 (2016).

[158] K. H. Nagai, F. Takabatake, Y. Sumino, H. Kitahata, M. Ichikawa, and N. Yoshinaga, *Physical Review E* **87**, 013009 (2013).

[159] D. Okawa, S. J. Pastine, A. Zettl, and J. M. Frechét, *Journal of the American Chemical Society* **131**, 5396 (2009).

[160] K. Suzuki and T. Sugawara, *ChemPhysChem* **17**, 1 (2016).

[161] A. Venancio-Marques, F. Barbaud, and D. Baigl, *Journal of the American Chemical Society* **135**, 3218 (2013).

[162] A. Onuki, *Phase Transition Dynamics*, Cambridge University Press, 2002.

[163] S. A. Safran, *Statistical Thermodynamics of Surfaces, Interfaces, and Membranes*, volume 90 of *Frontiers in Physics*, Addison-Wesley, Reading, Massachusetts, 1994.

[164] N. F. Bunkin and A. V. Lobeyev, *Colloids and Surfaces A* **129-130**, 33 (1997).

[165] I. Buttinoni, G. Volpe, F. Kümmel, G. Volpe, and C. Bechinger, *Journal of Physics: Condensed Matter* **24**, 284129 (2012).

[166] N. Kitamura, M. Yamada, S. Ishizaka, and K. Konno, *Analytical Chemistry* **77**, 6055 (2005).

[167] C. Lalaude, J. P. Delville, S. Buil, and A. Ducasse, *Physical Review Letters* **78**, 2156 (1997).

[168] S. Mukai, H. Kitahata, and K. Yoshikawa, *Chemical Physics Letters* **402**, 529 (2005).

[169] S. Mukai, N. Magome, H. Kitahata, and K. Yoshikawa, *Applied Physics Letters* **83**, 2557 (2003).

[170] H. Oana, A. Kishimura, K. Yonehara, Y. Yamasaki, M. Washizu, and K. Kataoka, *Angewandte Chemie International Edition* **48**, 4613 (2009).

[171] K. Sadakane, H. Kitahata, H. Seto, and K. Yoshikawa, *Physical Review E* **78**, 046214 (2008).

[172] F. Schmidt, A. Magazzu, A. Callegari, L. Biancofiore, F. Cichos, and G. Volpe, *Physical Review Letters* **120**, 068004 (2018).

[173] Y. Tsori, F. Tournilhac, and L. Leibler, *Nature* **430**, 544 (2004).

[174] K.-I. Yuyama, T. Rungsimanon, T. Sugiyama, and H. Masuhara, *The Journal of Physical Chemistry C* **116**, 6809 (2012).

[175] A. Ashkin, *Biophysical journal* **61**, 569 (1992).

[176] J. P. Delville, C. Lalaude, and A. Ducasse, *Physica A* **262**, 40 (1999).

[177] K. Svoboda and S. M. Block, *Annual Review of Biophysics and Biomolecular Structure* **23**, 247 (1994).

[178] I. K. Jun and H. Hess, *Advanced Materials* **22**, 4823 (2010).

[179] N. Magome, H. Kitahata, M. Ichikawa, S. M. Nomura, and K. Yoshikawa, *Physical Review E* **65**, 045202 (2002).

[180] S. Sengupta, D. Patra, I. Ortiz-Rivera, A. Agrawal, S. Shklyaev, K. K. Dey, U. Cordova-Figueroa, T. E. Mallouk, and A. Sen, *Natature Chemistry* **6**, 415 (2014).

[181] S. Sengupta, M. M. Spiering, K. K. Dey, W. Duan, D. Patra, P. J. Butler, R. D. Astumian, S. J. Benkovic, and A. Sen, *ACS Nano* **8**, 2410 (2014).

[182] M. Robert De Saint Vincent, H. Chraïbi, and J. P. Delville, *Physical Review Applied* **4**, 044005 (2015).

[183] H. M. J. M. Wedershoven, C. W. J. Berendsen, J. C. H. Zeegers, and A. A. Darhuber, *Physical Review Applied* **3**, 024005 (2015).

[184] A. Bergen, S. Rudiuk, M. Morel, T. Le Saux, H. Ihmels, and D. Baigl, *Nano Letters* **16**, 773 (2016).

[185] N. A. Ivanova, V. M. Starov, A. Trybala, and V. M. Flyagin, *Journal of Colloid and Interface Science* **473**, 120 (2016).

[186] D. E. Lucchetta, F. Simoni, L. Nucara, and R. Castagna, *AIP Advances* **5**, 077147 (2015).

[187] S. Yehoshua, R. Pollari, and J. N. Milstein, *Biophysical Journal* **108**, 2759 (2015).

[188] Y. Wang, Q. Zhang, Z. Zhu, F. Lin, J. Deng, G. Ku, S. Dong, S. Song, M. K. Alam, and D. Liu, *Science Advances* **3**, e1700555 (2017).

[189] R. Kubota, Y. Yamashita, T. Kenmotsu, Y. Yoshikawa, K. Yoshida, Y. Watanabe, T. Imanaka, and K. Yoshikawa, *ChemPhysChem* **18**, 959 (2017).

[190] M. M. Hanczyc, *Life* **4**, 1038 (2014).

[191] S. Ito, T. Sugiyama, N. Toitani, G. Katayama, and H. Miyasaka, *The Journal of Physical Chemistry B* **111**, 2365 (2007).

[192] V. Vitagliano, R. Sartorio, E. Chiaravalle, and O. Ortona, *Journal of Chemical and Engineering Data* **25**, 121 (1980).

[193] B. Banijamali and K.-J. Bathe, *International Journal for Numerical Methods in Engineering* **71**, 66 (2007).

[194] H. Chen, Q. Zhao, and X. Du, *Micromachines* **9**, 41 (2018).

[195] A. Mourran, H. Zhang, R. Vinokur, and M. Möller, *Advanced Materials* **29**, 1604825 (2017).

[196] B. Ten Hagen, F. Kümmel, R. Wittkowski, D. Takagi, H. Löwen, and C. Bechinger, *Nature Communication* **5**, 4829 (2014).

[197] L. Xu, F. Mou, H. Gong, M. Luo, and J. Guan, *Chemical Society Reviews* **46**, 6905 (2017).

[198] R. Koningsveld and A. Staverman, *Journal of Polymer Science* **6**, 325 (1968).

[199] J. A. Thomson, P. Schurtenberger, G. M. Thurston, and G. B. Benedek, *Proceedings of the National Academy of Sciences of the United States of America* **84**, 7079 (1987).

# Publications


[i] H. Sakuta, N. Magome, Y. Mori, K. Yoshikawa, ”Negative/Positive Chemotaxis of a Droplet: Dynamic Response to a Stimulant Gas”, *Applied Physics Letters* **108**, 203703 (2016).

[ii] 作田 浩輝、馬籠 信之、吉川 研一、「ナノの世界からマクロな世界を動かす: 見えない分子から巨視的な動きへ」『分子マシンの科学分子の動きとその機能を見る』、*CSJ* カレントレビュー **26 巻**、化学同人、日本、2017 年

[iii] Y. J. Chen, K. Sadakane, H. Sakuta, C. Yao, K. Yoshikawa, ”Spontaneous Oscillations and Synchronization of Active Droplets on a Water Surface via Marangoni Convection”, *Langmuir* **33**, 12362 (2017).

[iv] Y. Harada, K. Koyoshi, H. Sakuta, K. Sadakane, T. Kenmotsu, K. Yoshikaw, ”Emergence of Pendular and Rotary Motions of a Centimeter-Sized Metallic Sheet under Stationary Photoirradiation”, *The Journal of Physical Chemistry C* **122**, 2747 (2018).

[v] H. Sakuta, S. Seo, S. Kimura, M. Hoörning, K. Sadakane, T. Kenmotsu, M. Tanaka, K. Yoshikawa, ”Optical Fluid Pump: Generation of Directional Flow via Microphase Segregation/Homogenization”, *The Journal of Physical Chemistry Letters*, **9**, 5792 (2018).

[vi] H. Sakuta, T. Fujimoto, Y. Yamana, Y. Hoda, K. Tsumoto, K. Yoshikawa, ”Aqueous/Aqueous Micro Phase Separation: Construction of an Artificial Model of Cellular Assembly”, *Frontiers in Chemistry*, **7**, 44 (2019).

[vii] S. Sato, H. Sakuta, K. Sadakane, K. Yoshikawa, ”Self-Synchronous Swinging Motion of a Pair of Autonomous Droplets”, *ACS Omega* **4**, 12766 (2019).

# Acknowledgement

本論文の執筆にあたり、厚いご指導を賜りました、主査の 同志社大学大学院生命医科学研究科 廣安知之 教授、副査の 同志社大学大学院生命医科学研究科 貞包浩一朗 准教授、三重大学大学院工学研究科 湊元幹太 准教授 に謝意を申し上げます。

本論文における研究を行うにあたり、指導教員として御指導、御助言をくださいました、同志社大学生命医科学部生命物理科学研究室 吉川研一 教授、剣持貴弘 教授、ならびに、貞包浩一朗 准教授 に謝意を申し上げます。

本論文における研究の共同研究者として御指導、御助言をくださいました、お茶の水女子 森義仁 教授、獨協医科大学 馬籠信之 准教授、Shaoxing university Yong-Jun Chen 博士、名古屋大学 瀧口金吾 講師、法政大学 林真人 博士、名古屋大学 田中駿介 氏、三重大学 湊元幹太 准教授、北陸先端科学技術大学院大学 濵田勉 准教授、Heidelberg university 田中求 教授、Universität Stuttgart Marcel Hörning 博士、未来 ICT 研究所（NICT）大岩和弘 主幹研究員、国立遺伝学研究所 鳥澤嵩征 助教、東京理科大学 住野豊 准教授、千葉大学 北畑裕之 准教授、City university of New York Chwen-Yang Shew 教授 に謝意を申し上げます。

また、本論文における研究の共同研究者として活発な議論をしてくださいました、同志社大学大学院 2017 年修了 中谷真規 氏、2017 年修了 木村宗斗 氏、2018 年修了 妹尾駿佑 氏、2017 年修了 小吉圭佑 氏、2018 年修了 原田優吾 氏、2019 年修了 佐藤志帆 氏 に謝意を申し上げます。

研究を行うにあたって様々な形でご支援を頂きました、生命物理科学研究室秘書 古本真希子氏 に謝意を申し上げます。

同志社大学生命医科学研究科生命物理科学研究室の学友各位に謝意を申し上げます。

これまでの学生生活を見守り、支えていただいた、家族に心から深く感謝致します。

本論文に関する研究の一部は、日本学術振興会特別研究員 (DC2) として特別研究員奨励費 JP18J12947 の助成を受けたものです。ここに謝意を申し上げます。